Integrated phase-sensitive photonic sensors: a system design tutorial

Johannes Milvich,[1,2,*] Daria Kohler,[1] Wolfgang Freude,[1] and Christian Koos[1,3]

[1]Institute of Photonics and Quantum Electronics (IPQ), Karlsruhe Institute of Technology (KIT), Engesserstr. 5, 76131 Karlsruhe, Germany
[2]Robert Bosch GmbH, Robert-Bosch-Campus 1, 71272 Renningen, Germany
[3]e-mail: christian.koos@kit.edu
*Corresponding author: johannes.milvich@bosch.com

Photonic integration has seen tremendous progress over the previous decade, and several integration platforms have reached industrial maturity. This evolution has prepared the ground for miniaturized photonic sensors that lend themselves to efficient analysis of gaseous and liquid media, exploiting large interactions lengths of guided light with surrounding analytes, possibly mediated by chemically functionalized waveguide surfaces. Among the various sensor concepts, phase-sensitive approaches are particularly attractive: offering a flexible choice of the operation wavelength, these schemes are amenable to large-scale integration on mature technology platforms such as silicon photonics or silicon nitride (Si_3N_4) that have been developed in the context of tele- and data-communication applications. This paves the path toward miniaturized and robust sensor systems that offer outstanding scalability and that are perfectly suited for high-volume applications in life sciences, industrial process analytics, or consumer products. However, as the maturity of the underlying photonic integrated circuits (PICs) increases, system-level aspects of mass-deployable sensors gain importance. These aspects include, e.g., robust system concepts that can be operated outside controlled laboratory environments as well as readout schemes that can be implemented based on low-cost light sources, without the need for benchtop-type tunable lasers as typically used in scientific demonstrations. It is, thus, the goal of this tutorial to provide a holistic system model that allows us to better understand and to quantitatively benchmark the viability and performance of different phase-sensitive photonic sensor concepts under the stringent limitations of mass-deployable miniaturized systems. Specifically, we explain and formulate a generally applicable theoretical framework that allows for a quantitatively reliable end-to-end analysis of the overall signal chain. Building upon this framework, we identify and explain the most important technical parameters of the system, comprising the photonic sensor circuit, the light source, and the detector, as well as the readout and control scheme. We quantify and compare the achievable performance and the limitations that are associated with specific sensor structures based on Mach–Zehnder interferometers (MZIs) or high-Q optical ring resonators (RRs), and we condense our findings by formulating design guidelines both for sensor concepts. As a particularly attractive example, we discuss an MZI-based sensor implementation, relying on a vertical-cavity surface-emitting laser (VCSEL) as a power-efficient low-cost light source in combination with a simple and robust readout and control

scheme. In contrast to RR-based sensor implementations, MZIs can be resilient to laser frequency noise, at the cost of a slightly lower sensitivity and a moderately increased footprint. To facilitate the application of our model, we provide a MATLAB-based application that visualizes the underlying physical principles and that can be readily used to estimate the achievable performance of a specific sensor system. The system-level design considerations are complemented by an overview of additional aspects that are important for successful sensor system implementation such as the design of the underlying waveguides, photonic system assembly concepts, and schemes for analyte handling.

Integrated phase-sensitive photonic sensors: a system design tutorial

JOHANNES MILVICH, DARIA KOHLER, WOLFGANG FREUDE, AND CHRISTIAN KOOS

1. INTRODUCTION

Waveguide-based photonic sensors lend themselves to precise and highly sensitive analysis of a wide range of gaseous and liquid media [1–6], exploiting large interaction lengths of guided light with the surrounding analyte [7], possibly mediated by functionalized waveguide surfaces [8–10]. Utilizing established photonic integration platforms such as silicon photonics [11–14] or silicon nitride [15–18], photonic sensors are amenable to miniaturization and cost-efficient mass production and allow for massively parallel integration of multiplexed arrays on a single photonic chip [19]. Over the previous years, such devices have found their way into first commercial products [20–27], and this evolution will continue: driven by the need for ubiquitous data acquisition in an increasingly connected world, often described by Internet-of-things (IoT) scenarios, research efforts in the field of photonic sensors have intensified, and the application areas of such devices steadily expand. However, most of the associated proof-of-concept experiments are still performed in controlled laboratory environments, often relying on benchtop-type measurement equipment such as highly stable tunable lasers or high-resolution spectrometers for operation and readout. While these demonstrations have shown impressive results [1,2,5–10], the question arises to which extent the associated performance can be transferred to highly integrated mass-deployable sensor systems that rely on, e.g., non-ideal light sources with limited emission power that suffer from environmental influences such as thermal drift, and that are subject to noise as well as limited resolution of analog-to-digital converters (ADCs).

It is, thus, the goal of this tutorial to introduce and explain a comprehensive model for waveguide-based photonic sensor systems that allows us to estimate the impact of the various non-idealities on the overall system performance and that can be used for comparing and designing sensor systems for operation under real-world constraints. Building upon the existing literature, we focus our analysis on phase-sensitive schemes, which are particularly attractive for highly scalable low-cost systems: in contrast to absorption-based spectroscopic sensors, where the operation wavelength is dictated by the spectral characteristics of the respective analytes, phase-sensitive concepts are much more flexible with respect to the readout wavelength. This allows us to choose operating wavelengths for best compatibility with highly mature integration platforms such as silicon-on-insulator or silicon nitride that have been developed in the context of data- and telecommunication applications. In our analysis, we investigate different implementations of ring resonators (RRs) and Mach–Zehnder interferometers (MZIs), which represent the most widely used concepts for phase-sensitive integrated photonic sensors. As a particularly attractive scenario, we consider the use of vertical-cavity surface-emitting lasers (VCSELs) as compact and efficient light sources, along with simple photodiodes for detection. We experimentally verify our theoretical models, provide design guidelines, and quantify achievable performance parameters of the various sensor concepts. We find

that high-Q RRs, while showing excellent performance in laboratory experiments, are particularly prone to laser frequency noise, which turns out to dictate the limit of detection (LoD) when using mass-producible semiconductor lasers with linewidths in the MHz range. In contrast to that, properly designed MZI-based sensors are much less sensitive to laser frequency noise while offering simple operation along with detection limits that can well compete with those of high-Q micro-resonators. Along with the paper, we provide a MATLAB application that allows us to estimate and compare the sensitivity and LoD of different sensor system implementations based on noise parameters of the light source and the detection system.

This paper is structured as follows: Section 2 gives a brief overview of the state of the art of waveguide-based photonic sensors and the associated commercial products. Section 3 introduces a generic mathematical description of phase-sensitive sensor systems along with the model used for deriving the sensitivity and the associated LoD. Section 4 provides a quantitative analysis of the sensitivity and the LoD of typical RR- and MZI-based sensor implementations. In Section 5, we experimentally validate the model regarding the impact of laser frequency noise on the LoD, using a low-cost 1550 nm VCSEL as a test device and a benchtop tunable light source (TLS) as a reference. Section 6 condenses the key findings of the analysis into a set of guidelines for sensor design. Section 7 provides an overview of additional aspects that are important for a successful implementation of integrated photonic sensor systems and that are covered in the broader literature. An overall summary is found in Section 8. Details and mathematical descriptions of the signal and noise models are given in Appendices A–F.

2. WAVEGUIDE-BASED PHOTONIC SENSORS: STATE OF THE ART AND COMMERCIAL PRODUCTS

This tutorial builds on the existing scientific literature and introduces a model that allows us to estimate the performance of miniaturized phase-sensitive photonic sensor systems. As a starting point for this analysis, the following paragraphs provide an overview of the literature related to waveguide-based photonic sensors and of commercial products that rely on such devices.

On the scientific side, waveguide-based photonic sensors have been the subject of intensive research activities over the previous decade, and the number of publications is steadily increasing. A comprehensive overview of the current state of the art can be found in several scientific review articles, e.g., by Luan *et al.* for silicon photonic biosensors using label-free detection techniques [28], by Zou *et al.* for mid-infrared silicon photonic waveguides and devices [29], by Makarona *et al.* for point-of-need bioanalytics based on planar optical interferometry [30], or by Gavela *et al.* for silicon photonic biosensors [31]. These review papers provide an overview of concepts and experimental demonstrations of integrated sensors along with a comparison of experimentally demonstrated performances in terms of sensitivity and LoD. Application demonstrations range from classical refractive index (RI) sensors to biosensors that exploit chemically functionalized waveguide surfaces for label-free detection of cells, bacteria, viruses, or biomolecules such as proteins or nucleic acids.

Fostered by such research, waveguide-based sensors have found their way into their first commercial products. Prominent examples are handheld trace-gas sensors based on absorption spectroscopy [20,21] or disposable sensor chips for bio-diagnostics that exploit resonance shifts in photonic crystals [22–25] or in highly multiplexed RR arrays [19,26,27]. This evolution will continue, and highly scalable miniaturized sensor systems will gain importance, building the base for ubiquitous data acquisition in an increasingly connected world. In this context, rapid transition from

proof-of-concept laboratory demonstrations to commercially viable sensor systems is key. In the following sections, we focus on integrated phase-sensitive photonic sensors, and we introduce a quantitatively reliable model that accounts for the constraints of highly scalable miniaturized systems operated under realistic field conditions. This model provides a fundamental understanding of concepts, design options, and trade-offs for such systems and builds the base for important system design decisions regarding the selection of the photonic circuits and the specifications of the corresponding optoelectronic components.

3. SENSOR SYSTEM MODEL AND PERFORMANCE PARAMETERS

In the following, we introduce a high-level description of the sensor system model (Subsection 3.1), and subsequently evaluate the sensor performance to determine the sensor system sensitivity (Subsection 3.2) as well as the sensor system LoD (Subsection 3.3).

3.1. Sensor System Description

The generic concept of an integrated phase-sensitive photonic sensor system is illustrated in Fig. 1(a). The system combines a photonic sensor chip with electronic control and readout circuits. In view of technically and commercially viable sensor systems, we focus our analysis on phase-sensitive concepts that rely on simple optical power measurements rather than on more demanding spectrally resolved detection techniques [32]. Note, however, that the fundamental concepts, performance trade-offs, and design choices outlined in this analysis can be transferred to spectrally resolved detection techniques as well, which ultimately also rely on power measurements. As a consequence, sensor concepts that are based on, e.g., tracking of spectral features such as resonances of RRs [33], Bragg gratings [34], or photonic crystals [24] are ultimately subject to detection limits that are similar to the ones estimated from our analysis.

As an example for an integrated phase-sensitive photonic sensing element, the illustration in Fig. 1(a) shows an MZI with long waveguide spirals in each arm. The MZI is part of a photonic integrated circuit (PIC) that is connected to laser sources and detectors via grating couplers (GCs) [see top level "Photonics" of the stack in Fig. 1(a)]. Note that the MZI is just an example—the model developed in the following can be generally applied to MZI and RR-based sensors. Similarly, the illustration in Fig. 1(a) shows a VCSEL as a particularly simple light source that can be operated with small pump currents and that can be efficiently fabricated in large quantities [35]. On the bottom level "Electronics," the system comprises laser drivers, photodetector (PD) readout electronics, and ADCs, as well as digital signal processing (DSP) circuits for electrical signal generation and evaluation. Depending on the integration level, the ADC and the DSP circuits may be realized from discrete components on a printed circuit board (PCB), as a monolithic field-programmable gate array (FPGA), or as an application-specific integrated circuit [ASIC, shown in Fig. 1(a)].

3.2. Sensor System Sensitivity

A simplified schematic of the sensor PIC in the form of an MZI is illustrated in Fig. 1(b). A certain region of the PIC, indicated by a yellow area with a magenta waveguide section, is exposed to the environment to record a change Δ_{env} of an environmental parameter and to convert it into a change Δn_{e} of the effective modal index. We define this conversion as the waveguide sensitivity $S_{\mathrm{env}} = \Delta n_{\mathrm{e}}/\Delta_{\mathrm{env}}$. The effective-index change Δn_{e} is then translated into a phase shift in the corresponding MZI arm and, thus, leads to a change ΔT of the optical power transmission factor

$T = P_o/P_i$ between the sensor input power P_i and the sensor output power P_o on the PIC. The magnitude of the transmission change ΔT for a given effective-index change Δn_e is quantified by the effective-index sensitivity $S_e = \Delta T/\Delta n_e$. The transmission change ΔT results in a measurable power change $\Delta P_o = P_i \Delta T$ at the output,

$$\begin{aligned} \Delta P_o &= P_i S_e S_{env} \Delta_{env} = S_{sys} \Delta_{env}, \\ S_{sys} &= P_i S_e S_{env} = \Delta P_o / \Delta_{env}, \\ S_e &= \Delta T/\Delta n_e, \quad S_{env} = \Delta n_e / \Delta_{env}. \end{aligned} \tag{1}$$

The system sensitivity S_{sys} is defined as the output power change ΔP_o with respect to environmental changes Δ_{env} and is governed by three main factors: the effective optical input power P_i, the waveguide sensitivity S_{env}, and the effective-index sensitivity S_e. These quantities are described in more detail in the following paragraphs.

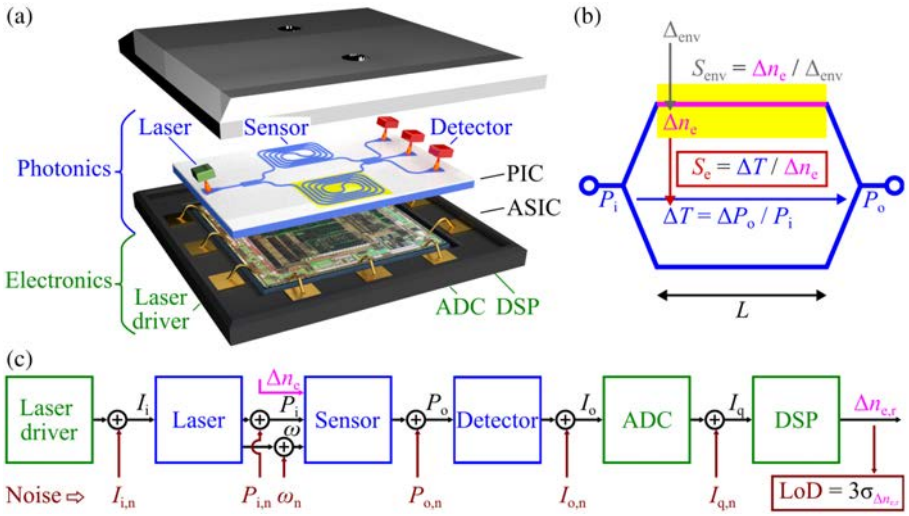

Concept and model of an integrated phase-sensitive photonic sensor system. (a) Artist's view, comprising a photonic sensor chip with laser light sources and detectors ("Photonics"), along with electronic control and readout circuits ("Electronics"). (b) Principle of a photonic effective-index sensor. Within a sensitive waveguide region (magenta), an environmental change Δ_{env} (yellow) is converted into a change Δn_e of the effective modal refractive index via the waveguide sensitivity $S_{env} = \Delta n_e/\Delta_{env}$, and this effective-index change leads to a phase shift $\Delta\varphi$ along the sensitive waveguide region. In a phase-sensitive photonic circuit such as a Mach–Zehnder interferometer (MZI), this phase shift leads to a change of the optical power transmission $T = P_o/P_i$, which is defined as the ratio of the optical output power P_o and the effective input power P_i. The effective-index sensitivity $S_e = \Delta T/\Delta n_e$ is defined as the ratio of the power-transmission change ΔT and the effective-index change Δn_e. (c) Propagation of signal and noise quantities through the sensor system. All electronic and photonic stages add noise to the respective electrical currents I, optical powers P, or optical frequencies ω. The limit of detection (LoD) of the sensor system can be quantified by the 3σ-deviation of the reconstructed effective refractive index $\Delta n_{e,r}$. All noise-related quantities are denoted by a subscript "n".

3.2a. Effective Optical Input Power P_i

The signal level is described by the effective optical input power P_i, which is obtained by multiplying the physical output power P_LD of the laser diode with the optical power transmission factors of the coupling interface between the laser and the sensor PIC and of the lossy on-chip circuits, as well as of the PIC-detector interface. In other words, the effective optical input power accounts for all optical excess losses that result from non-idealities of the various sensor components such as coupling losses in chip-chip interfaces or propagation losses in on-chip transport waveguides, but not the unavoidable loss that results, e.g., from destructive interference at the MZI output because this is accounted for by the power transmission factor $T = P_\mathrm{o}/P_\mathrm{i}$. We quantify all these excess losses by a single power transmission factor $\eta < 1$,

$$P_\mathrm{i} = \eta P_\mathrm{LD}. \tag{2}$$

The effective optical input power can, hence, be improved either by increasing the laser power or by decreasing the excess loss of the various components. This calls for advanced photonic assembly concepts and for efficient light-source integration (see Section 7 for further details).

3.2b. Waveguide Sensitivity S_{env}

The waveguide sensitivity S_env describes the dependence of the effective modal index change $\Delta \mathrm{n_e}$ on a change Δ_env of an environmental parameter, caused, e.g., by a change of the waveguide's surrounding medium, by adsorption of analyte molecules to the waveguide surface, or by a change of temperature or stress within the waveguide. For a given operating point, the waveguide sensitivity can be approximated by the associated derivative,

$$S_\mathrm{env} = \frac{\partial n_\mathrm{e}}{\partial \Delta_\mathrm{env}}. \tag{3}$$

Note that the optimization of integrated waveguides with respect to the waveguide sensitivity S_env is a major subject in its own right [1,6,36,37]. A brief discussion of the various design options and of the associated state of the art can be found in Section 7.

For a RI sensor, Δ_env is given by the RI n_M of the medium that surrounds the waveguide. In this case, the waveguide sensitivity S_env can directly be linked to the so-called bulk phase sensitivity $S_\varphi = \partial\varphi/\partial n_\mathrm{M}$, which is often given in radians per RI unit (RIU) [28]. This bulk sensitivity quantifies the phase shift $\Delta\varphi = -k_0 L \Delta n_\mathrm{e}$ accumulated in a sensor waveguide of length L upon a change Δn_M of the surrounding medium,

$$S_\varphi = \left|\frac{\partial\varphi}{\partial n_\mathrm{M}}\right| = k_0 L \frac{\partial n_\mathrm{e}}{\partial n_\mathrm{M}} = k_0 L S_\mathrm{env}. \tag{4}$$

In this relation, $k_0 = \omega/c$ is the vacuum propagation constant of the light, where ω denotes the angular frequency of the optical wave, and where the vacuum speed of light is denoted as c. For resonator-based RI sensors, the bulk sensitivity can also be expressed by the shift $\Delta\lambda_\mathrm{res}$ of a resonance wavelength per refractive-change Δn_M of the surrounding medium,

$$S_{\lambda,\mathrm{RR}} = \frac{\partial\lambda_\mathrm{res}}{\partial n_\mathrm{M}} = \frac{\lambda}{n_\mathrm{eg}} S_\mathrm{env}. \tag{5}$$

Here, $n_\mathrm{eg} = n_\mathrm{e} - \lambda\partial n_\mathrm{e}/\partial\lambda$ is the effective group RI. Note that using wavelength-related bulk sensitivities for MZIs is somewhat more intricate since it is strongly

dependent on the asymmetry of the interferometer arms (see Appendix A for a more detailed discussion).

In the following analysis, we consider the waveguide design and, hence, the waveguide sensitivity S_{env} to be fixed. For a better comparability of the different sensor concepts, independently of the underlying waveguide design, we consider Δn_{e} as the physical quantity to be measured in the following sections, without further discussing its origin and its quantitative relationship to the actual change Δ_{env} of an environmental parameter. We are further only interested in RI sensors in which Δ_{env} predominantly affects the real part of the RI at the wavelength of interest while leaving the imaginary part, i.e., the waveguide loss, virtually unchanged. This is in contrast to absorption-based detection techniques, which rely on the molecular absorption properties at specific wavelengths and, therefore, often require light sources at dedicated wavelengths.

3.2c. Effective-Index Sensitivity S_e

For a given set of laser, waveguide, PD, and assembly technologies, the effective optical input power P_{i} according to Eq. (3) and the waveguide sensitivity S_{env} in Eq. (3) are fixed. The remaining degree of freedom in Eq. (1), hence, lies in the photonic sensor circuit design, which defines the effective-index sensitivity S_{e}, i.e., the ratio of the change of the power transmission T and the underlying change of the effective-index,

$$S_{\mathrm{e}} = \frac{\partial T}{\partial n_{\mathrm{e}}} = \frac{\partial}{\partial n_{\mathrm{e}}} \left(\frac{P_{\mathrm{o}}}{P_{\mathrm{i}}} \right). \tag{6}$$

To quantify S_{e} we need to consider the phase shift $\Delta\varphi = -k_0 L \Delta n_{\mathrm{e}}$ that the optical signal accumulates during propagation through the sensitive waveguide of length L [see Fig. 1(b) for an exemplary illustration for an MZI-based sensor]. Note that our model is based on wave propagation of the form $\exp(\mathrm{j}(\omega t - \beta z))$, where $\beta = n_{\mathrm{e}} k_0$ is the propagation constant of the guided mode. The phase shift $\Delta\varphi$ is converted into a change of the sensor output power ΔP_{o} by either an interferometric or a resonant circuit—the corresponding relations depend on the underlying sensor concept and on the respective operating point (see Section 4 for a more detailed analysis). In general, the optical power transmission T of the integrated MZI or RR fundamentally depends on the modal power loss coefficient α and on the associated optical amplitude transmission factor $a = \exp(-\alpha L/2)$ of the sensitive waveguide section. Like S_{env}, the modal power loss coefficient α depends on the waveguide technology and geometry, and it is, hence, regarded as a constant parameter for the optimization of the sensor system. This is a valid approach for all cases in which the sensor waveguide design is dictated by other constraints arising, e.g., from the underlying fabrication processes. In case the sensor waveguide design and, hence, α and S_{env} can be varied, a joint optimization of the system sensitivity $S_{\mathrm{sys}} = P_{\mathrm{i}} S_{\mathrm{e}} S_{\mathrm{env}}$ can be performed. In this case, an adaptation of the waveguide design will simultaneously affect the environmental sensitivity S_{env} and the effective-index sensitivity S_{e} and may, hence, allow for an ideal trade-off that optimizes the overall system performance. This is, e.g., useful in applications where the evanescent field of the waveguide mode interacts with an absorbing analyte such that an increase of S_{env} is unavoidably accompanied by an increase of the absorption loss, which usually results in a decreased effective-index sensitivity S_{e} [6,36].

3.3. Sensor System Limit of Detection

The schematic signal propagation of the sensor system is depicted in Fig. 1(c) and comprises currents I_{i} and I_{o}, at the input of the drive laser and at the sensor output, as well as optical signals with angular frequency ω and powers P_{i} and P_{o} at the input and

the output of the photonic section (see Table 1 for a summary of the symbols). The digitized signal of the ADC at the sensor output is described by a quantized photocurrent I_q. All signal quantities are random variables $x \in \{I_i,\ P_i,\ \omega,\ P_o,\ I_o,\ I_q\}$ with mean $\bar{x}$, fluctuation $\delta x = x - \bar{x}$, and variance $\sigma_x^2 = \overline{x^2}$. The output signal of the system is a reconstructed value $\Delta n_{e,r}$ of the actual effective RI change Δn_e, which is distorted by the accumulated noise contributions.

The output signal of each stage contains noise that originates from previous stages, as well as uncorrelated random noise ζ_n with mean $\overline{\zeta_n} = 0$ and variance $\sigma_{\zeta_n}^2 = \overline{\zeta_n^2}$ generated in the stage itself. The noise propagation through a specific stage can be described by a linearized transfer function in the respective operating point. As an example, the overall stochastic variance $\sigma_{P_o}^2$ of the photonic sensor output power P_o can be approximated by

$$\sigma_{P_o}^2 = \overline{|P_o - \overline{P_o}|^2} = \sigma_{P_{o,n}}^2 + \left|\frac{\partial P_o}{\partial P_i}\right|^2 \sigma_{P_i}^2 + \left|\frac{\partial P_o}{\partial \omega}\right|^2 \sigma_\omega^2. \tag{7}$$

In these relations, the overbar $\bar{X}$ denotes the expectation value of the respective expression X, while $\partial P_o/\partial P_i$ and $\partial P_o/\partial \omega$ represent the linearized transfer functions between the sensor input power P_i and frequency ω to the sensor output power P_o in its operating point. The total variance $\sigma_{P_o}^2$ in Eq. (7) consists of a sum of three uncorrelated noise terms, where $\sigma_{P_{o,n}}^2 = \overline{P_{o,n}^2}$ represents the additive noise originating from the sensor stage as such, while the other two terms describe the propagation of the noisy optical power and frequency with variances $\sigma_{P_i}^2$ and σ_ω^2 from the previous stage. Applying the same noise propagation scheme to all other stages in the system, we obtain an accumulated reconstruction variance $\sigma_{\Delta n_{e,r}}^2$ of the reconstructed effective RI $\Delta n_{e,r}$. This variance finally dictates the useful sensor resolution, and it defines the LoD [1] as

$$\mathrm{LoD} = 3\sigma_{\Delta n_{e,r}}. \tag{8}$$

A quantitative analysis of each noise source in Table 1, of the associated error propagation, and of the respective impact on the total LoD is given in Subsection 4.3.

4. QUANTITATIVE ANALYSIS OF INTEGRATED PHASE-SENSITIVE PHOTONIC SENSOR SYSTEMS BASED ON RING RESONATORS AND MACH–ZEHNDER INTERFEROMETERS

With the overall sensor model described in Section 3 at hand, we can now perform a quantitative analysis of the performance of sensor systems based on different photonic circuits such as RRs and MZIs. We first introduce the photonic sensor concepts

Table 1. Description of Signal Variables and Noise Contributors in a Highly Integrated Photonic Sensor System[a]

Signals			Noise	
I_i	Laser input current	*(electrical)*	$I_{i,n}$	Laser driver current noise
P_i	Sensor input power	*(optical)*	$P_{i,n}$	Laser intensity noise
ω	Angular frequency	*(optical)*	ω_n	Laser frequency noise
P_o	Sensor output power	*(optical)*	$P_{o,n}$	Temperature-induced fluctuation of sensor output power
I_o	Photodetector output current	*(electrical)*	$I_{o,n}$	Photocurrent shot noise and additional detector noise
	ADC output current	*(digital)*	$I_{q,n}$	ADC quantization noise
$\Delta n_{e,r}$	Reconstructed effective refractive index	*(digital)*	LoD	Limit of detection ($3\sigma_{\Delta n_{e,r}}$)

[a]The cumulated noise in the reconstructed effective refractive index $\Delta n_{e,r}$ leads to a certain limit of detection.

and analytical models (Subsection 4.1), which allows us to determine the effective-index sensitivity S_e (Subsection 4.2). The corresponding mathematical relations are summarized in Tables 2 and 3. Finally, we estimate and compare the LoD (Section 5) for each RR- and MZI-based sensor implementation, which is summarized comprehensively in Table 4. Further mathematical details are provided in Tables 5 and 6 in the appendices.

4.1. Photonic Sensor Concepts and Analytical Models

In the following, we consider three different photonic sensor implementations of both RRs (Subsection 4.1a) as well as MZIs (Subsection 4.1b), as illustrated in Fig. 2. In each of these two sections, we introduce the sensor concepts, explain the sensing process, highlight key parameters, and derive the generic optical power transmission T, which is used as a basis for the subsequent sensitivity and LoD calculations.

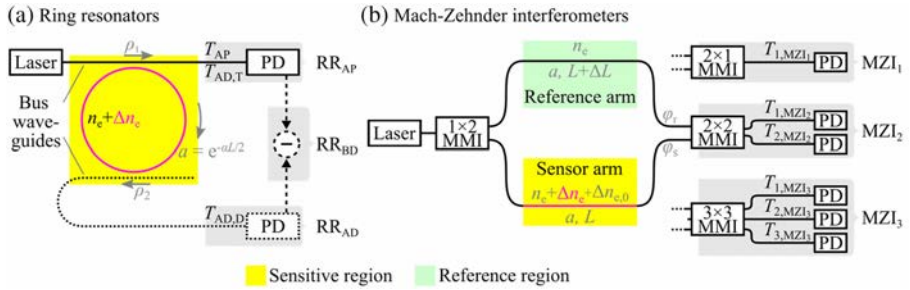

Schematic of common phase-sensitive integrated photonic sensors. A laser launches an optical signal into a single-mode on-chip waveguide. All waveguide sections within a sensitive region (yellow) are subject to an effective-refractive-index change Δn_e resulting from a change Δ_env of an environmental parameter. The index change is translated into a measurable change of one or more optical output powers, which are recorded by photodiodes (PD). The corresponding change of the optical power transmission functions $T(\Delta n_\mathrm{e})$ depends on the specific implementation of the respective sensor circuit. Different implementations of photonic sensors are shaded in gray. (a) Sensor implementations based on ring resonators, comprising an all-pass ring resonator ($\mathrm{RR_{AP}}$) with a single through port (solid lines), an add-drop ring resonator ($\mathrm{RR_{AD}}$) having an additional drop port bus waveguide (dotted lines), and a balanced-detection add-drop ring resonator ($\mathrm{RR_{BD}}$) that relies on the difference signal between the through port and the drop port (dashed lines). The associated optical power transmission factors T_AP, $T_\mathrm{AD,T}$, and $T_\mathrm{AD,D}$ depend on the coupling to and from the resonator as given by the amplitude transmission ρ_1 and ρ_2 of the coupling sections, on the round trip length L, and on the round trip amplitude transmission factor a. Analytic expressions for the various power transmission factors are given in Eqs. (10) and (12), and in Appendix B. (b) Sensor implementations based on Mach–Zehnder interferometers: a 1×2 multimode interference (MMI) coupler splits the input signal into a reference and a sensor arm. Propagation through these arms leads to different phase shifts φ_r and φ_s at the input of the 2×1, 2×2, or 3×3 MMI coupler that is used to recombine the signals in the MZI with one ($\mathrm{MZI_1}$), two ($\mathrm{MZI_2}$) or three output ports ($\mathrm{MZI_3}$), respectively. For the 3×3 MMI coupler, the signals are fed to the first and the last input port, whereas the second is left unconnected. In general, the optical power transmission factors depend on the arm lengths L and $L + \Delta L$ of the sensing and the reference arm, on the amplitude transmission factors a, which we assume to be identical for both arms, on the effective refractive index $n_\mathrm{e} + \Delta n_\mathrm{e} + \Delta n_{\mathrm{e},0}$ of the sensor arm, and on its counterpart n_e for the reference arm [see Eqs. (11) and (12)].

4.1a. Ring Resonators

For RR-based sensor implementations, three different readout approaches are illustrated in Fig. 2(a). The first approach relies on a RR in a so-called "all-pass configuration" [33], in which the ring is coupled to a single bus waveguide, which serves both as an input and an output port (RR_{AP}; associated elements indicated by solid lines). In the second implementation, another bus waveguide is coupled to the ring to tap a drop signal from the resonator that is detected by a single photodiode (add-drop RR, RR_{AD})—the additional elements to RR_{AP} are indicated by dotted lines. The third implementation also comprises a drop waveguide but uses a pair of balanced detectors (BDs) to extract the difference signal of optical powers at the through port and at the drop port (RR_{BD})—the additional elements to RR_{AD} are indicated by dashed lines. All these implementations have specific advantages: the RR_{AP} concept is attractive due to its simple design and high resonator Q-factor, which leads to a high sensitivity, RR_{AD} allows us to multiplex several rings on a single bus waveguide, and RR_{BD} simplifies the feedback control to maintain the operating point of highest effective-index sensitivity, as detailed in Subsection 4.2c.

Sensing in RRs relies on detecting a change Δn_e of the effective RI within the sensitive region, depicted in yellow in Fig. 2(a), which comprises the RR. The corresponding phase shift $-k_0 L \Delta n_e$ in a resonator with round trip length L causes a phase change with respect to the round trip phase shift $\varphi_{OP,RR}$ in the operating point. This additional phase shift modifies the overall round trip phase φ_{RR},

$$\begin{aligned} \varphi_{RR} &= -k_0 L \Delta n_e + \varphi_{OP,RR}, \\ \varphi_{OP,RR} &= -k_0 L n_e, \end{aligned} \tag{9}$$

which then leads to a change of the optical power transmission T (see Appendix B).

Key parameters are the operating point, characterized by the round trip phase shift and the round trip optical amplitude transmission $a = \exp(-\alpha L/2)$, as well as the amplitude transmission ρ_1 and ρ_2 and the corresponding cross coupling amplitude transmission κ_1 and κ_2 at the coupling sections of the through and the drop port. The round trip length L also dictates the free spectral range (FSR) $\Delta\omega_{FSR,RR}$ of the RR, which corresponds to the frequency increment that increases the magnitude of the round trip phase shift $k_0 L n_e$ by 2π and which is given by the reciprocal of the round trip group delay $\tau_{g,RR} = -\partial\varphi_{OP,RR}/\partial\omega = n_{eg} L/c = 1/\Delta\omega_{FSR,RR}$.

In the following, we assume lossless coupling sections, $\kappa_1^2 + \rho_1^2 = \kappa_2^2 + \rho_2^2 = 1$, which are not affected by the change Δn_e of the effective-index of the waveguide mode in the sensing region. Based on these parameters, we can calculate the optical power transmission as a function of the effective-index change Δn_e and, hence, the RR phase φ_{RR} (see also Subsection 4.2 and Appendix B for further details),

$$\begin{aligned} T_{AP} &= \frac{\rho_1^2 - 2\rho_1 a \cos(\varphi_{RR}) + a^2}{1 - 2\rho_1 a \cos(\varphi_{RR}) + (\rho_1 a)^2}, \\ T_{ADT} &= \frac{\rho_2^2 a^2 - 2\rho_1\rho_2 a \cos(\varphi_{RR}) + \rho_1^2}{1 - 2\rho_1\rho_2 a \cos(\varphi_{RR}) + (\rho_1\rho_2 a)^2}, \\ T_{ADD} &= \frac{(1-\rho_1^2)(1-\rho_2^2) a}{1 - 2\rho_1\rho_2 a \cos(\varphi_{RR}) + (\rho_1\rho_2 a)^2}. \end{aligned} \tag{10}$$

4.1b. Mach–Zehnder Interferometers

For MZI-based sensor implementations, we consider three typical two-arm implementations as illustrated in Fig. 2(b), featuring 1×2 multimode interference (MMI) coupler for splitting the input power in a sensor arm passing the sensitive region (depicted in yellow) and in a reference arm (depicted in green). For simplicity, we assume both arms to have the same power transmission, and we only consider the phase shift difference in the following calculations.

The effective RI change Δn_e causes a phase shift $-k_0 L \Delta n_\mathrm{e}$ in the sensor arm and modifies the phase difference $\varphi_\mathrm{MZI} = \varphi_\mathrm{s} - \varphi_\mathrm{r}$ of the optical sensor and reference signals entering the 2×1 (MZI_1), 2×2 (MZI_2), or 3×3 MMI couplers (MZI_3). All MMI couplers are assumed to be lossless with ideal splitting ratios for equal output powers. In absence of an effective RI change in the sensitive region, $\Delta n_\mathrm{e} = 0$, the optical signals in the reference and in the sensor arm experience a phase difference $\varphi_\mathrm{OP,MZI}$, which determines the MZI operating point. The phase difference $\varphi_\mathrm{OP,MZI}$ of the operating point may be caused either by a geometric length difference ΔL between the reference and the sensor arm or by a difference $\Delta n_{\mathrm{e},0}$ of the effective RI that occurs even in absence of an environmental change Δ_env. The overall phase difference at the output of the two arms may, hence, be written as

$$\varphi_\mathrm{MZI} = \varphi_\mathrm{s} - \varphi_\mathrm{r} = -k_0 L\, \Delta n_\mathrm{e} + \varphi_\mathrm{OP,MZI}, \quad \varphi_\mathrm{OP,MZI} = -k_0 (L \Delta n_{\mathrm{e},0} - \Delta L\, n_\mathrm{e}),$$
$$\varphi_\mathrm{s} = -k_0 L (n_\mathrm{e} + \Delta n_{\mathrm{e},0} + \Delta n_\mathrm{e}), \quad \varphi_\mathrm{r} = -k_0 n_\mathrm{e} (L + \Delta L). \tag{11}$$

For the MZI, the FSR $\Delta\omega_\mathrm{FSR,MZI}$ corresponds to the spectral period of the transmission fringes and is given by the reciprocal of the group delay difference $\tau_\mathrm{g,MZI} = -\partial\varphi_\mathrm{OP,MZI}/\partial\omega = (L \Delta n_\mathrm{eg,0} - \Delta L n_\mathrm{eg})/c = 1/\Delta\omega_\mathrm{FSR,RR}$. The phase difference $\varphi_\mathrm{OP,MZI}$ in the MZI operating point may be adjusted by design, e.g., via the geometric length difference ΔL of the two arm lengths, or by using different waveguide designs in the two arms that allow us to adjust the effective RI offset $\Delta n_{\mathrm{e},0}$. These methods may be combined with a dynamic operating-point adjustment, e.g., by implementing electronically or thermally controlled phase shifters in the MZI arms, or by tuning the laser frequency ω (see Subsection 4.2c). Note that the operating point $\Delta\varphi_\mathrm{OP,MZI}$ of the interferometer can be set to zero independently of the operating wavelength by matching the optical path lengths via $L \Delta n_{\mathrm{e},0} = \Delta L n_\mathrm{e}$. In this case, the group delay difference $\tau_\mathrm{g,MZI} \approx 0$ vanishes, thereby eliminating the frequency dependency of the optical power transmission.

The extra outputs of the MZI_2 and MZI_3 implementations help in data processing [38,39] at the cost of an increased readout complexity. Specifically, the three output currents of the MZI_3 can be processed by a Clarke transformation [40] to reduce the three output signals to a pair of signals that represent the in-phase and the quadrature-phase components of a complex signal with phase angle φ_MZI. This allows us to make the sensor sensitivity independent of the operating point and further allows us to eliminate directional signal ambiguity [41]. Note that, in principle, further output ports may added. This, however, only increases the complexity of the photonic circuit without improving the sensor performance any further. Three output ports may, hence, be considered an ideal trade-off between implementation complexity and functionality. A study on fundamental limits and design considerations for a coherent phase-readout of different kinds of MZI-based sensors can be found in [42].

Independent of the specific implementation, the change Δn_e of the effective RI leads to a change ΔT of the optical power transmission at the MZI outputs, which is finally evaluated. Key parameters are the phase difference $\Delta\varphi_\mathrm{OP,MZI}$ in the operating point, the length L of the sensitive waveguide section, and the amplitude transmission

factors a of the MZI arms. For a two-arm MZI having a 1×2 MMI coupler for splitting the power into the two arms and a lossless $\mu \times \mu$ MMI coupler ($\mu = 2,\ 3,\ \ldots$) with the first and the last input port connected to the MZI arms for recombining the signals, the general optical power transmission T for the νth output port ($\nu = 1 \ldots \mu$) can be written as

$$T_{\nu,\mathrm{MZI}_\mu} = \frac{a^2}{\mu}\left(1 + \sin\left(\varphi_{\mathrm{MZI}} + 2\pi\frac{\nu-1}{\mu} + \frac{\pi}{2}\mathrm{mod}(\mu, 2)\right)\right),$$
$$\mu = 2,\ 3, \ldots, \quad \nu = 1 \ldots \mu. \tag{12}$$

In this relation, φ_{MZI} denotes the phase difference of the optical signals entering the two ports of the output MMI [see Eq. (11)], a^2 is the power transmission factor of the MZI arms, and $\mathrm{mod}(\mu, 2)$ refers to the remainder of the Euclidean division of μ by 2. The power transmission factor a^2 is assumed to be the same for both interferometer arms. Note that the overall power transmission T_{ν,MZI_μ} of the different MZI output ports $\nu = 1 \ldots \mu$ reveals a sinusoidal dependence on the phase difference φ_{MZI}. These sinusoidals are offset in phase by constant increments $2\pi/\mu$, which is a direct consequence of the distinct phase relations in $\mu \times \mu$ MMI couplers [43]. Note also that, for MZI_μ with $\mu > 1$, the combination of the signals in the $\mu \times \mu$ MMI coupler does not introduce any additional power loss. This is different for an MZI terminated by a 2×1 MMI ($\mu = 1$), for which lossless combination of the signals is only possible for constructive interference at $\varphi_{\mathrm{MZI}} = 2\pi m (m \in \mathbb{N})$. In this case, the optical power transmission can be written as

$$T_{\nu,\mathrm{MZI}_1} = \frac{a^2}{2}(1 + \cos(\varphi_{\mathrm{MZI}})). \tag{13}$$

Note that in our further analysis, the power transmission factor a^2 is assumed to be the same for both interferometer arms.

4.2. Effective-Index Sensitivity

In this section, we analytically maximize the effective-index sensitivity of the RR- and MZI-based sensor implementations in Fig. 2 by optimizing the sensor operating point as well as the circuit design parameters, i.e., the round trip length and coupling coefficients for RR, and the arm length for MZI. As a baseline, we use the generic optical power transmission T from Eqs. (10) and (12) derived in the previous two sections, and we assume a set of technologically fixed parameters, namely the vacuum propagation constant k_0 of the light source as well as the effective-index n_e and the modal power loss coefficient α of the sensor waveguide.

In order to quantify and to compare the effective-index sensitivity of all sensor implementations, we start by extending the optical power transmission T by defining an effective optoelectronic transmission τ and sensitivity $S_{\mathrm{e},\tau}$ (Subsection 4.2a). This allows for a comparison with concepts that are relying on signals from multiple outputs ($\mathrm{RR}_{\mathrm{BD}}$, MZI_2, MZI_3) by including the combination of the digitized PD currents I_q. Based on τ, we quantify the optoelectronic effective-index sensitivity $S_{\mathrm{e},\tau}$ (Subsection 4.2b), where we find general analytical expressions for both the RR and MZI. With this sensitivity model at hand, we determine optimum operating points $\varphi_{\mathrm{OP,opt}}$ (Subsection 4.2c) of each sensor and derive the peak sensitivity $S_{\mathrm{e},\tau,\mathrm{peak}}$ as a function of the remaining design parameters. We further provide details on the operating-point control in fully integrated photonic sensor systems. We exploit $S_{\mathrm{e},\tau,\mathrm{peak}}$ to analytically find optimum design parameters (Subsection 4.2d), in particular for the MZI arm length and for the round trip length and the amplitude transmission ρ_1, ρ_2 of the coupling sections in case of the RR. We further formulate

requirements regarding the laser diode linewidth $\Delta\omega_{\mathrm{FWHM,LD}}$ that are associated with highly sensitive measurements in RR- and MZI-based sensor circuits. Finally, we perform a quantitative comparison of the optoelectronic effective-index sensitivity $S_{\mathrm{e},\tau,\mathrm{max}}$ for each RR- and MZI-based sensor implementation (Subsection 4.2e).

4.2a. Optoelectronic Transmission and Optoelectronic Effective-Index Sensitivity

In sensor systems relying on signals from multiple outputs ($\mathrm{RR_{BD}}$, $\mathrm{MZI_2}$, $\mathrm{MZI_3}$), further processing steps such as additions or subtractions are required in the electronic or digital domain to obtain the output signal. To include these steps in our model, we extend the optical power transmission T of all sensor types by defining an effective optoelectronic transmission,

$$\tau = f(T, \Re). \tag{14}$$

The effective optoelectronic transmission τ comprises the additional processing steps of the analog or digitized electric signals as well as the overall electric readout responsivity $\Re$, which accounts for the photodiode responsivity and for the gain of any electrical readout amplifiers. For simplicity, we assume the same frequency-independent electric readout responsivity $\Re$ for the various output ports of the photonic sensor circuits. In analogy to Eq. (6), we can then define an optoelectronic effective-index sensitivity,

$$S_{\mathrm{e},\tau} = \frac{\partial \tau}{\partial n_{\mathrm{e}}}, \tag{15}$$

that refers to the optoelectronic transmission τ rather than to the optical transmission T. For sensor circuits with only one output ($\mathrm{RR_{AP}}$, $\mathrm{RR_{AD}}$, $\mathrm{MZI_1}$), the optoelectronic transmission τ can be obtained from the optical transmission T by a simple multiplication with the electric readout responsivity $\Re$, $\tau = \Re T$, and Eq. (15) simplifies to $S_{\mathrm{e},\tau} = \Re S_{\mathrm{e}}$. For sensor circuits with multiple outputs ($\mathrm{RR_{AP}}$, $\mathrm{RR_{AD}}$, $\mathrm{MZI_1}$), further processing of the acquired and digitized photocurrents I_q is involved, leading to additions and subtractions of the respective optical power transmission factors. The effective optoelectronic transmission τ of the three RRs and the three MZI circuits is shown in Column 2 of Table 2. For the case of $\mathrm{MZI_3}$, the phase difference between the MZI arms can be extracted by merging the three readout signals into a complex-valued optoelectronic transmission function τ and by determining its argument (see the last row of Table 2).

4.2b. Sensitivity Analysis of RR- and MZI-Based Sensors

In the following, we develop quantitative models for the effective optoelectronic transmission and the optoelectronic effective-index sensitivity of RR- and MZI-based sensors. For the three RR-based implementations, we assume that the rings have identical round trip lengths L, modal power loss coefficients α, and effective group refractive indices $n_{\mathrm{eg}} = n_{\mathrm{e}} + \omega \partial n_{\mathrm{e}}/\partial\omega$ and, thus, identical intrinsic Q-factors Q_i, which are defined as the product of the cavity resonance frequency ω_{res} and the photon lifetime τ_{c},

$$Q_{\mathrm{i}} = \omega_{\mathrm{res}} \tau_{\mathrm{c}} = n_{\mathrm{eg}} \frac{k_0}{\alpha}. \tag{16}$$

In the subsequent analysis, we consider different coupling strengths of the RR to the single ($\mathrm{RR_{AP}}$) or the pair ($\mathrm{RR_{AD}}$, $\mathrm{RR_{BD}}$) of bus waveguides, which we quantify by the quality ratio $c_Q = Q/Q_{\mathrm{i}}$ of the loaded Q-factor Q and the intrinsic, unloaded Q-factor Q_i,

$$Q = c_Q Q_i, \quad c_Q \leq 1. \tag{17}$$

For loaded high-Q RRs, the power transmission characteristics can be approximated by a Lorentzian for the drop ports, and by its complement to unity transmission for the through ports. This is done by a Taylor approximation of the cosine term $\cos(\varphi_{RR}) \approx 1 - (\varphi_{RR} - \varphi_{res})^2/2$ in Eq. (10) for small offsets $\Delta\varphi_{RR} = \varphi_{RR} - \varphi_{res}$ of the round trip phase from that the nearest resonance $\varphi_{res} = 2\pi\, m (m \in \mathbb{N})$, i.e., for $|\Delta\varphi_{RR}| \ll 1$ (see Appendix C for details). For the remainder of this subsection, we assume for simplicity that the RR is operated at its optical resonance frequency ω_{res} in the absence of an effective-index change, i.e., for $\Delta n_e = 0$, and we consider the change of the effective optoelectronic transmission τ as a function of Δn_e. The dependence of the effective optoelectronic transmission τ on the effective-index change Δn_e is then given by the simplified Lorentz-based optoelectronic transmission functions in the third column of Table 2 for the RR_{AP}, the RR_{AD}, and the RR_{BD} implementation. In Subsection 4.2c, we will consider the choice of the optimum operating point given by a phase offset $\Delta\varphi_{OP,RR}$, which is adjusted by tuning the laser away from the resonance frequency of the ring. This simply corresponds to a horizontal shift of the effective optoelectronic transmission characteristics—the transmission characteristics for any other operating point $\varphi_{OP,RR}$ can be obtained by replacing Δn_e in Rows 2, 3, and 4 of Table 2 through $\Delta n_e - \varphi_{OP,RR}/(k_0 L)$. Note that, when using the Lorentzian approximation, the effective optoelectronic transmission characteristics of a ring-based sensor are fully defined by two simple parameters: the resonance depth or output contrast $\hat{\tau}$ and the resonance width $\Delta n_{eg,FWHM,RR} = n_{eg}/Q$ with respect to effective-index change Δn_e (see also Table 6 in Appendix C).

Based on these models, Fig. 3(a) shows the effective optoelectronic transmission τ as a function of an effective-index change Δn_e for the various RR-based sensor implementations. For the RR_{AP} and the RR_{AD}, we investigate the case of critical coupling (superscript "CC") as well as an under-coupled (superscript "UC") implementation, for which the coupling to the through and drop port is chosen to maximize the sensitivity in the optimum operating point (see Subsection 4.2d). The two black lines in Fig. 3(a) correspond to the critically coupled (CC) RR_{AP} (RR_{AP}^{CC}, solid black line, $c_Q = 1/2$) and to its under-coupled (UC) counterpart (RR_{AP}^{UC}, dashed black line, $c_Q = 2/3$). Similarly, the two red lines in Fig. 3(a) correspond to RR_{AD}, again CC (RR_{AD}^{CC}, solid red line, $c_Q = 1/4$) and UC (RR_{AD}^{UC}, dashed red line, $c_Q = 1/3$) For the

Table 2. Effective Optoelectronic Transmission τ of the Different RR-Based and MZI-Based Sensor Implementations as Defined in Fig. 2[a,b,c]

Sensor Impl.	Effective Optoelectronic Transmission τ		Output Contrast $\hat{\tau}/\Re$
	General	Simplified	
RR_{AP}	$\tau_{RR_{AP}} = \Re T_{AP}$	$\left\{\begin{matrix}1-\\0+\\1-\end{matrix}\right\} \hat{\tau}\, \frac{1}{1+\left(\frac{2\Delta n_e}{n_{eg}/Q}\right)^2}$	$1 - \frac{(a-\rho_1)^2}{(1-\rho_1 a)^2}$
RR_{AD}	$\tau_{RR_{AD}} = \Re T_{ADD}$		$\frac{(1-\rho_1^2)(1-\rho_2^2)a}{(1-\rho_1\rho_2 a)^2}$
RR_{BD}	$\tau_{RR_{BD}} = \Re(T_{AD} - T_{ADD})$		$\frac{(a+1)(\rho_1{}^2-1)(a\rho_2^2-1)}{(1-\rho_1\rho_2 a)^2}$
MZI_1	$\tau_{MZI_1} = \Re T_{1,MZI_1}$	$\hat{\tau}/2 \times (1 + \cos(\Delta n_e k_0 L + \varphi_{OP,MZI}))$	a^2
MZI_2	$\tau_{MZI_2} = \Re(T_{2,MZI_2} - T_{1,MZI_2})$	$\hat{\tau}/2 \times \sin(\Delta n_e k_0 L + \varphi_{OP,MZI})$	$2a^2$
MZI_3	$\tau_{MZI_3} = \Re(2T_{2,MZI_3} - T_{3,MZI_3} - T_{1,MZI_3}) + j\Re\sqrt{3}(T_{3,MZI_3} - T_{1,MZI_3})$	$\hat{\tau}/2 \times \exp(-j(\Delta n_e k_0 L + \varphi_{OP,MZI}))$	$2a^2$

[a]For each sensor implementation indicated in Column 1, Column 2 gives a general expression for the optoelectronic transmission τ, assuming the same electric readout responsivity $\Re$ for each output.

[b]The relations in Column 3 refer to the simplified τ for an effective-refractive-index change Δn_e that are derived in Appendices B and C. These relations depend on the normalized output contrast $\hat{\tau}$ in Column 4 as a parameter.

[c]For the ring resonators, we assume that the device is operated at its optical resonance frequency, i.e., $\varphi_{OP,RR} = 2\pi\, m (m \in \mathbb{N})$, in the absence of an effective-index change ($\Delta n_e = 0$). Choosing an optimum operating point according to Subsection 4.2c corresponds to a simple shift of the effective optoelectronic transmission characteristics τ along Δn_e.

RR_{BD}, we only consider an UC implementation (RR_{BD}^{UC}, solid blue line, $c_Q = 1/3$), which simultaneously maximizes sensitivity and leads to perfect power transmission balancing of the two output ports in the optimum operating point.

The sensitivity $S_{e,\tau}$, Fig. 3(c), is obtained by taking the derivative of the effective optoelectronic transmission τ with respect to the effective-index change Δn_e [see Eq. (15)]. Qualitatively, the effective optoelectronic transmissions of RR_{AP} show steeper slopes with respect to Δn_e and, thus, a higher peak sensitivity $S_{e,\tau,peak}$ compared to those of RR_{AD} and RR_{BD}. This can be understood from the fact that both RR_{AD} and RR_{BD} require a second waveguide to be coupled to the ring, which decreases the loaded Q-factor and, hence, reduces the slope of the Lorentzian that approximates the resonance. Furthermore, slightly UC resonators outperform CC RRs.

We also formulate simplified expressions for the optoelectronic transmission τ of the various MZI-based sensor implementations (see the third column of Table 2), which have been derived from Eqs. (11)–(13). It can be seen that the output contrast of the MZI_1 is only half of all other MZI_μ versions (see Column 4 of Table 2). Figure 3(b) shows the corresponding effective optoelectronic transmission τ as a function of the effective-index change Δn_e. We limit our consideration to the range $\Delta n_e \in [-\pi; +\pi]/(k_0 L)$, exploiting the fact that the transmission characteristics are periodic with respect to Δn_e, where the period is given by the effective-index increment that increases the MZI phase difference φ_{MZI} by 2π. For the case of MZI_2 (MZI_3), we additionally indicate the individual contributions MZI_{2i} (MZI_{3i}) of the various MMI coupler outputs $\nu = 1, 2$ ($\nu = 1, 2, 3$) in dashed lines. This leads to a pair of sinusoidals that are phase-shifted by π in case of MZI_2 and to three sinusoidals that are phase-shifted by $2\pi/3$ for MZI_3. Note that for MZI_3, the optoelectronic transmission is a complex number (see Column 3, last row in Table 2), for which we plot the magnitude only. The MZI sensitivity shown Fig. 3(d) is again obtained by taking the derivative of the effective optoelectronic transmission τ with respect to the effective-index change Δn_e. Note that for the plots in Figs. 3(b) and 3(d), we assume operating points for which the phase difference of the two arms corresponds to an integer multiple of 2π, $\varphi_{OP,MZI} = 2\pi\ m (m \in \mathbb{Z})$. The transmission characteristics of any other operating points defined by a non-zero phase offset $\Delta\varphi_{OP,MZI}$ can be deduced from the plots by shifting the abscissa by $\Delta\varphi_{OP,MZI}/(k_0 L)$.

4.2c. Optimum Operating Points and Peak Sensitivity

For RRs, the optimum operating points offering the peak sensitivity $S_{e,\tau,peak}$ can be found at the inflection points of the Lorentzian that approximates the optical power transmission in the vicinity of the resonance frequency ω_{res}. Using the relations summarized in Appendix C, Table 6, we can calculate the phase offset in the optimum operating point of a RR as

$$\Delta\varphi_{OP,RR,opt} = \pm\frac{1}{2\sqrt{3}}\frac{\alpha L}{c_Q}. \tag{18}$$

In a typical experiment, a resonance is found by either tuning the input laser frequency or the effective RI of the waveguide in the resonator until minimum (RR_{AP}) or maximum (RR_{AD}) power transmission is achieved. From this resonance condition, the optimum operating point can be reached either through a frequency offset $\Delta\omega_{OP,RR,opt} = \omega_{res}/(2\sqrt{3}Q)$ or through a RI offset $\Delta n_{e,OP,RR,opt} = n_{eg}/(2\sqrt{3}Q)$ (see Table 6 in Appendix C).

For MZI_1 and MZI_2, the operating points for peak sensitivity $S_{e,\tau,peak}$ can be found accordingly, leading to phase offsets,

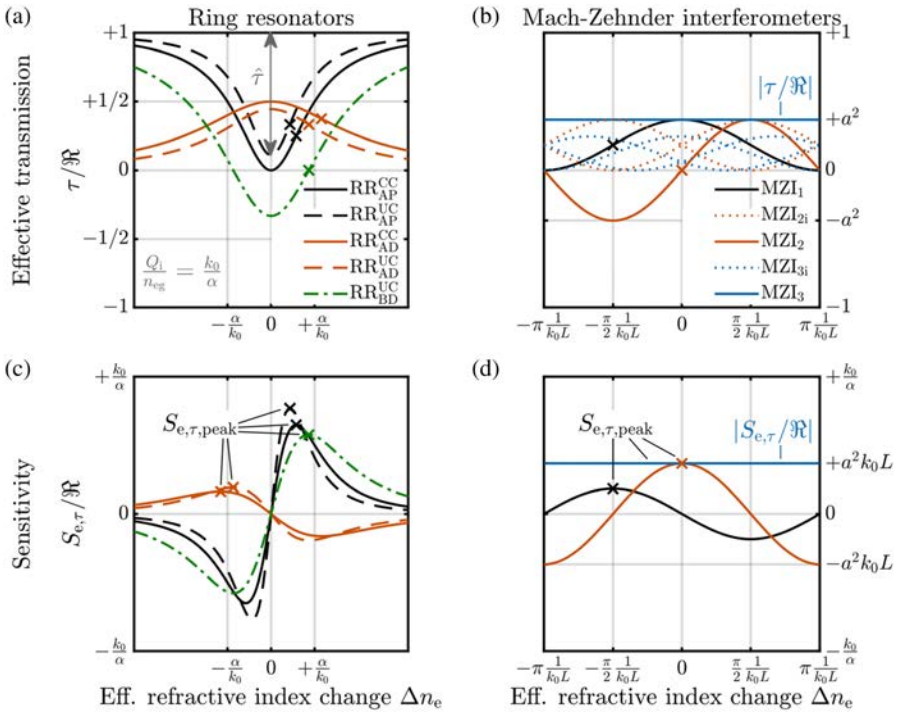

Optoelectronic transmission τ and optoelectronic effective-index sensitivity $S_{e,\tau}$ of the different sensor implementations based on ring resonators and MZI. (a) Effective optoelectronic transmission τ of RR-based implementations. For better comparability, all rings are assumed to have the same round trip length L, the same modal power loss coefficient α, the same effective group refractive index n_{eg}, and, thus, the same intrinsic Q-factor Q_i. We plot the diagrams for a critically coupled all-pass ring resonator ($\mathrm{RR}_{\mathrm{AP}}^{\mathrm{CC}}$, solid black line) and for its under-coupled counterpart ($\mathrm{RR}_{\mathrm{AP}}^{\mathrm{UC}}$, dashed black line), for a critically coupled and for an under-coupled add-drop ring resonator each with a single photodetector ($\mathrm{RR}_{\mathrm{AD}}^{\mathrm{CC}}$, solid red line, and $\mathrm{RR}_{\mathrm{AD}}^{\mathrm{UC}}$, dashed red line), and for an under-coupled add-drop ring resonator with balanced detection at the output ($\mathrm{RR}_{\mathrm{BD}}^{\mathrm{UC}}$, solid blue line), for which the photonic circuit is identical to that of $\mathrm{RR}_{\mathrm{AD}}^{\mathrm{UC}}$. The results are normalized by the electric readout responsivity $\Re$, which is assumed to be the same for the various outputs. For single-output sensors, the quantity $\tau/\Re = T$ gives the optical transmission. Relevant transmission changes happen around the resonance for $\Delta n_{\mathrm{e}} = \pm\alpha/k_0 = \pm n_{\mathrm{eg}}/Q_{\mathrm{i}}$. For simplicity, we assume that, in the absence of an effective-index change ($\Delta n_{\mathrm{e}} = 0$), the devices are operated at an optical resonance frequency, i.e., $\varphi_{\mathrm{OP,RR}} = 2\pi m (m \in \mathbb{N})$. The transmission characteristics for any other operating point defined by a non-zero phase offset $\Delta\varphi_{\mathrm{OP,RR}}$ can be deduced from the plots by shifting the abscissa by $\Delta\varphi_{\mathrm{OP,RR}}/(k_0 L)$. (b) Effective optoelectronic transmission of single-, double-, and triple-output Mach–Zehnder interferometers (MZI_1, MZI_2, MZI_3; black, red, and blue lines). Solid lines correspond to the individual outputs; dashed–dotted lines show combined effective optoelectronic transmissions. The trace plotted for MZI_3 refers to the magnitude of the complex effective optoelectronic transmission obtained from the last row of Table 2. For simplicity, we assume identical arm lengths and that, in the absence of an effective-index change ($\Delta n_{\mathrm{e}} = 0$), the phase shifts in the MZI two arms are identical or differ by an integer multiple of 2π $\varphi_{\mathrm{OP,MZI}} = 2\pi m (m \in \mathbb{N})$, The transmission characteristics of any other operating point defined by a non-zero phase offset $\Delta\varphi_{\mathrm{OP,MZI}}$ can be deduced from the plots by shifting the abscissa by $\Delta\varphi_{\mathrm{OP,MZI}}/(k_0 L)$. (c), (d) Optoelectronic effective-index sensitivity $S_{\mathrm{e},\tau} = (1/\Re)(\partial\tau/\partial n_{\mathrm{e}})$ of the RR and MZI, normalized by the electric readout responsivity $\Re$. For single-output sensors,

$S_{\mathrm{e},\tau}/\Re = S_{\mathrm{e}}$. Peak sensitivities $S_{\mathrm{e},\tau,\mathrm{peak}}$ in the optimum operating point are marked with crosses in all subfigures. Quantitative values can be found in Table 3. The trace for MZI_3 again refers to the magnitude of the complex optoelectronic effective-index sensitivity obtained from the last row of Table 2. In this case, $S_{\mathrm{e},\tau}$ is independent of the operating point.

$$\Delta\varphi_{\mathrm{OP,MZI,opt}} = \pm\frac{\pi}{2} + \begin{cases} 0 & \text{for } \mathrm{MZI}_1, \\ \frac{\pi}{2} & \text{for } \mathrm{MZI}_2. \end{cases} \tag{19}$$

The effective optoelectronic transmissions of MZI_1, MZI_2, and MZI_3 are drawn in solid lines. For MZI_3, the sensitivity is again a complex number for which we only plot the magnitude. Due to the advantageous signal combination, the magnitude of the sensitivity does not depend on the operating point for MZI_3.

With the optimum operating points at hand, we can now formulate relations for the associated peak sensitivity. To this end, we first express the peak sensitivities of RR- and MZI-based sensor implementations in terms of the output contrast $\hat{\tau}$ between minimum and maximum transmission of the respective device, as specified in the last column of Table 2,

$$S_{\mathrm{e},\tau,\mathrm{peak}} = \begin{cases} \frac{3}{8}2\sqrt{3}\frac{Q}{n_{\mathrm{eg}}}\hat{\tau} = \frac{3}{8}2\sqrt{3}\frac{k_0}{\alpha}c_{\mathrm{Q}}\hat{\tau} & \text{for RR}, \\ \frac{\hat{\tau}}{2}k_0 L & \text{for MZI}. \end{cases} \tag{20}$$

To derive these relationships, we assumed again that the power transmission of the RRs can be approximated by a Lorentzian for the drop ports, and by its complement to unity transmission for the through ports [see Eqs. (C1) and (C2) as well as Table 6 of Appendix C]. For the RR, the output contrast $\hat{\tau}$ represents the amplitude of this Lorentzian, which is equivalent to the resonance depth, and $c_Q = Q/Q_{\mathrm{i}}$ refers to the ratio of the loaded Q-factor Q and the intrinsic, unloaded Q-factor Q_{i}, [see Eq. (17)]. For MZI_1 and MZI_2, $\hat{\tau}$ is given by the peak-to-peak swing of the effective transmission τ when tuning the MZI phase difference φ_{MZI} over 2π. For MZI_3, $\hat{\tau}$ is calculated by summing over the output contrasts of the individual output ports.

Note that maintaining the optimum operating point of sensors based on RR, MZI_1, or MZI_2 is not a trivial task. In many cases of practical interest, the fabrication process of the sensor PIC is imperfect, such that it is impossible to reliably set the optimum operation point by design. In this case, a method to actively tune the system to $\Delta\varphi_{\mathrm{OP,RR,opt}}$ or $\Delta\varphi_{\mathrm{OP,MZI,opt}}$ is required. Furthermore, the operating points are affected by long-term drifts, caused, for example, by temperature or degradation effects. As a consequence of these drifts, measurement of absolute quantities over extended periods of time is usually much harder than detecting abrupt changes. As an example, relative measurements are usually sufficient for biosensors that detect binding events of target analytes to functionalized waveguide surfaces, which typically occur over time scales of a few minutes [27]. In contrast to that, long-term monitoring of absolute gas concentrations crucially relies not only on robust sensor calibration, but also on effective elimination of drift phenomena. To this end, it is necessary to equip the sensor system with appropriate stabilization mechanisms and/or feedback loops that can dynamically adjust tuning parameters to maintain the optimum operating point. This tuning can rely on, e.g., waveguide sections with thermal or free-carrier-injection phase shifters, a technique that is applicable to both MZIs and RRs. For RRs and asymmetric MZIs with non-zero group delay difference $\tau_{\mathrm{g,MZI}} = (L\Delta n_{\mathrm{eg},0} - \Delta L n_{\mathrm{eg}})/c$, the operating point may also be set by tuning the laser frequency. This is not an option in the case of symmetric MZIs with zero or very small group delay differences, which lead to an FSR $\Delta\omega_{\mathrm{FSR,MZI}} = 1/\tau_{\mathrm{g,MZI}}$ that exceeds the

tuning range of the underlying light source. On the other hand, sensor systems based on symmetric MZIs are less sensitive to laser frequency noise (see Subsection 4.3 for details).

For the balanced-detection schemes such as in the RR_{BD} and MZI_2 sensor implementations, the associated feedback loop to control these tuning elements is simple, as the effective optoelectronic transmission τ in the optimum operating point is always exactly zero. The feedback control loop just has to minimize τ and, hence, does not require any reference bias. It can be designed without knowledge of the expected signal levels, which may even vary over time.

For MZI_1, RR_{AP}, and RR_{AD}, a more sophisticated feedback loop is required to tune to the optimum operating point. As an example, a small phase modulation can be employed that can easily be extracted at the sensor output. In the optimum operating point, the modulation amplitude at the senor output reaches a maximum, since the phase sensitivity is maximized along with the optoelectronic effective-index sensitivity. The feedback control loop has then to maintain the maximum modulation amplitude at the output.

For the MZI_3-based implementation, the sensitivity is independent of the operating point, which renders active feedback control unnecessary and, thus, vastly reduces system complexity. Moreover, a large dynamic range at constant sensitivity can be obtained by unwrapping the measured phases, provided that the acquisition bandwidth at the sensor output is fast enough to continuously track the phase change. Combining an unbalanced MZI_3 with a sufficiently large modulation of the operation wavelength allows for endless phase unwrapping even if the signal is not tracked continuously [41].

4.2d. Optimum Design Parameters for Overall Maximum Sensitivity

In the preceding sections, we have calculated the transmission functions and the extended effective optoelectronic transmission functions that define the effective-index sensitivities for a set of selected sensor implementation examples. We found that each sensor can be tuned to an optimum operating point that offers the highest sensitivity toward changes of the effective RI in the sensitive regions [see Eq. (20)]. We will now expand our consideration and globally optimize the sensor design to identify the fundamental sensitivity limit that can be achieved for a given technology-specific modal power loss coefficient α and a given operating wavelength $\lambda = 2\pi / k_0$. In this consideration, the only remaining design parameters are the arm length L for the MZI and the round trip length L along with the amplitude transmission ρ_1, ρ_2 of the coupling sections for the RR. In the following, we analytically optimize these parameters based on Eq. (20) to obtain a maximum sensitivity, where, for the case of RRs, ρ and L are also encoded in c_Q and $\hat{\tau}$. We only discuss the results in the subsequent paragraphs—the mathematical details of this optimization are given in Appendix D.

Ring resonator coupling coefficients. The top panel of Fig. 4(a) shows the peak optoelectronic effective-index sensitivity $S_{e,\tau,peak}$ of an all-pass RR (RR_{AP}) tuned to the optimum operating point relative to the maximum achievable peak optoelectronic effective-index sensitivity $S_{e,\tau,max}$ as a function of the amplitude transmission ρ_1 of the coupling section between the ring and the bus waveguide. Notably, $S_{e,\tau,max}$ is achieved for an UC RR ($\rho_1 = \sqrt{a}$) and not for critical coupling ($\rho_1 = a$). For the add-drop configuration (RR_{AD}), $S_{e,\tau,peak}$ depends on the amplitude transmission ρ_1 and ρ_2 of the through port and drop port coupling sections and is plotted as a colored contour map in the bottom panel of Fig. 4(a). Also here, $S_{e,\tau,max}$ is found in a slightly UC regime ($\rho_1 = \rho_2 = a$), yielding a roughly 20% higher peak sensitivity compared

to the CC case ($\rho_1 = \rho_2 a$). The characteristics for the add-drop configuration with balanced detection (RR_{BD}) are the same as for RR_{AD}.

Device length. Figure 4(b) shows the peak sensitivities of different RR- and MZI-based sensor implementations as a function of the attenuation αL. For MZI, an optimum arm length of $L_{opt} = 1/\alpha$ can be found. This optimum results from the fact that large arm lengths increase the accumulated phase shift but decrease the optical power transmission and, hence, the output contrast. Exploiting the full potential of low-loss waveguide technologies through MZI-based sensors, hence, requires large device footprints.

For RR, we consider different implementations based on all-pass (RR_{AP}), add-drop (RR_{AD}), and balanced-detection (RR_{BD}) schemes. We consider both CC and UC implementations, see Table 3 for the exact choice of the amplitude transmission ρ_1 and ρ_2 of the coupling sections. Irrespective of the exact RR-based sensor implementation, the sensitivity is essentially length-independent for $\alpha L \ll 1$, provided that the coupling coefficients are adapted to the respective value of $a = \exp(-\alpha L/2)$ as indicated in Fig. 4(a). Note that $\alpha L \ll 1$ is typically the case for RRs with radii on the order of tens of micrometers realized on state-of-the-art integration platforms.

Note that our considerations did so far not take into account any non-idealities of the drive laser such as frequency noise, quantified by a non-zero linewidth, which can lead to a fading of the sensitivity. In the following, we consider laser sources with non-zero linewidths. To cover the range of practically relevant line shapes, we perform the analysis for both Lorentzian and Gaussian line shapes (see Appendix D) for details. The results are shown in Fig. 4(c). We can observe a fading of the optoelectronic effective-index sensitivity if the laser linewidth $\Delta\omega_{FWHM,LD}$ approaches the full width at half-maximum $\Delta\omega_{FWHM,RR}$ of the ring resonance or the MZI FSR $\Delta\omega_{FSR,MZI}$. As a rule of thumb, the laser linewidth should be kept 2 orders of magnitude smaller than the spectral features of the sensor transmission characteristics. Specifically, for high-Q RRs, the laser linewidth becomes a particularly crucial parameter and may set an upper limit for usable RR Q-factors for a laser with a given linewidth. Note

Table 3. Peak Optoelectronic Effective-Index Sensitivity $S_{e,\tau,peak}$ and Maximum Peak Optoelectronic Effective-Index Sensitivity $S_{e,\tau,max}$ Along with Corresponding Optimized Design Parameters for the Various RR- and MZI-Based Sensor Implementations[a,b,c,d]

	L_{opt}	$\rho_{1,opt}$	$\rho_{2,opt}$	c_Q	$\frac{\hat{\tau}}{\Re}$	$\frac{\tau_{OP}}{\Re}$	$\frac{S_{e,\tau,peak}}{\Re}$ $\left(\frac{S_{e,\tau,max}}{\Re}\ \text{if}\ (^*)\right)$
RR_{AP}^{CC}	$< \frac{1}{\alpha}$	a	–	$\frac{1}{2}$	1	$\frac{1}{4}$	$\frac{3\sqrt{3}}{8} \times \frac{k_0}{\alpha}$
RR_{AP}^{UC}	$< \frac{1}{\alpha}$	$\sqrt{a}$	–	$\frac{2}{3}$	$\frac{8}{9}$	$\frac{1}{3}$	$\frac{4\sqrt{3}}{9} \times \frac{k_0}{\alpha}$ $(^*)$
RR_{AD}^{CC}	$< \frac{1}{\alpha}$	a^2	a	$\frac{1}{4}$	$\frac{1}{2}$	$\frac{3}{8}$	$\frac{3\sqrt{3}}{32} \times \frac{k_0}{\alpha}$
RR_{AD}^{UC}	$< \frac{1}{\alpha}$	a	a	$\frac{1}{3}$	$\frac{4}{9}$	$\frac{1}{3}$	$\frac{\sqrt{3}}{9} \times \frac{k_0}{\alpha}$ $(^*)$
RR_{BD}^{UC}	$< \frac{1}{\alpha}$	a	a	$\frac{1}{3}$	$\frac{4}{3}$	0	$\frac{\sqrt{3}}{3} \times \frac{k_0}{\alpha}$ $(^*)$
MZI_1	$\frac{1}{\alpha}$	–	–	–	$\frac{1}{e}$	$\frac{1}{2e}$	$\frac{1}{2e} \times \frac{k_0}{\alpha}$ $(^*)$
MZI_2	$\frac{1}{\alpha}$	–	–	–	$\frac{2}{e}$	0	$\frac{1}{e} \times \frac{k_0}{\alpha}$ $(^*)$
MZI_3	$\frac{1}{\alpha}$	–	–	–	$\frac{2}{e}$	$\frac{1}{e}$ [a]	$\frac{1}{e} \times \frac{k_0}{\alpha}$ $(^*)$

[a]Note that, due to the complex-valued transmission τ of MZI_3, we specify $|\tau_{OP}|/\Re$.

[b]For the ring resonators (RR), we assume a given vacuum wavenumber k_0 and modal power loss coefficient α and calculate the peak optoelectronic effective-index sensitivity $S_{e,\tau,peak}$ in the optimum operating point for different implementations based on all-pass (RR_{AP}), add-drop (RR_{AD}), and balanced-detection (RR_{BP}) schemes as defined in Fig. 2.

[c]The quantity $a = \exp(-\alpha L/2)$ denotes the round trip amplitude transmission factor. The maximum peak optoelectronic effective-index sensitivity $S_{e,\tau,max}$ is obtained for the under-coupled (UC) implementations, indicated by an asterisk (*) in the last column. For the critically coupled (CC) implementations of RR_{AP} and RR_{AD}, the peak sensitivity $S_{e,\tau,peak}$ is smaller than for the UC implementation.

[d]The parameters a, ρ_1, and ρ_2 fully define the quality ratio $c_Q = Q/Q_i$ of the RR [see Eq. (17)], as well as the effective output contrast $\hat{\tau}$ and the effective optoelectronic transmission τ_{OP} for RR and MZI in the respective optimum operating point. For the MZI, we choose the optimum arm length $L = 1/\alpha$.

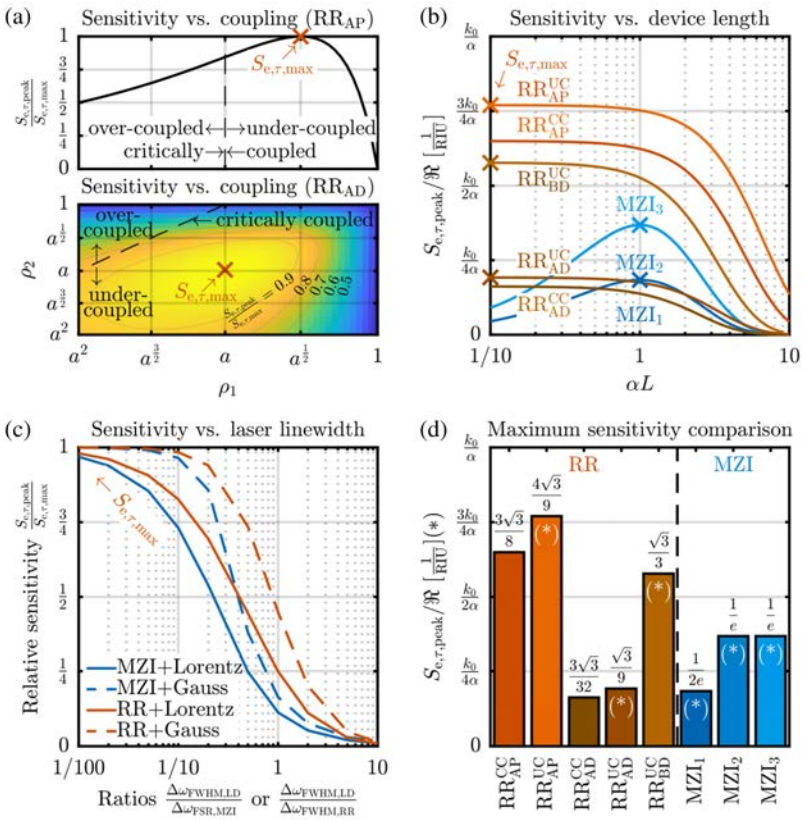

Design optimization for maximum peak optoelectronic effective-index sensitivity and comparison of sensor implementations. (a) Influence of the amplitude transmission ρ_1 and ρ_2 of the through port and drop port coupling sections on the peak optoelectronic effective-index sensitivity $S_{e,\tau,peak}$ of all-pass (RR$_{AP}$, top panel) and add-drop (RR$_{AD}$, bottom panel) RR with indications of over-coupled (OC), under-coupled (UC), and critically coupled (CC) regimes. $S_{e,\tau,peak}$ is normalized to its maximum peak value $S_{e,\tau,max}$ for the respective configuration. The characteristics for the add-drop configuration with balanced detection (RR$_{BD}$) are the same as for RR$_{AD}$. For the RR$_{AP}$ configuration, critical coupling is achieved for $\rho_1 = a$. For the RR$_{AD}$ and RR$_{BD}$ configurations, critical coupling requires $\rho_1 = a\rho_2$, indicated by a dashed line in the lower panel. (b) Influence of RR round trip length (red) and MZI arm length (blue) on the peak effective-index sensitivity $S_{e,\tau,peak}$, normalized by the electric readout responsivity $\Re$. Optimum device lengths are marked with crosses. Note that, for the case of RR in a certain coupling state, the effective-index sensitivity is essentially independent of the round trip length L as long as the round trip attenuation is small, $\alpha L \ll 1$. For the MZI, an optimum arm length of $L_{opt} = 1/\alpha$ can be found. (c) Sensitivity fading caused by frequency noise of the drive laser, quantified by a finite linewidth. We consider Lorentzian as well as Gaussian emission spectra, which are characterized by their full widths at half-maximum $\Delta\omega_{FWHM,LD}$. For RR, $\Delta\omega_{FWHM,LD}$ imposes a lower practical limit on the spectral width $\Delta\omega_{FWHM,RR}$ of the resonance and, hence, leads to an upper limit of the usable Q-factor for a given laser source. Note that these limitations do not apply to the MZI, since $\Delta\omega_{FSR,MZI}$ can always be made arbitrarily large by matching the group delay in the two arms. (d) Comparison of the peak effective-index sensitivity $S_{e,\tau,peak}$ and the fundamentally achievable maximum peak effective-index sensitivity $S_{e,\tau,max}$ for the various sensor concepts. All sensitivities are given as fractions of k_0/α and are ultimately limited the modal power loss coefficient α. Note that higher wavenumbers k_0 do generally not increase the optoelectronic

effective-index sensitivity $S_{e,\tau}$: for a given quantum efficiency of the photodetector, the electric readout responsivity $\Re$ is inversely proportional to the photon energy and, hence, to the vacuum wavenumber $k_0 = \omega/c$, which exactly cancels the influence of k_0 on $S_{e,\tau}$. For a given waveguide technology, the MZI can ultimately perform almost as well as the RR while being insensitive to the laser linewidth. For MZIs as well as under-coupled (UC) ring resonators, the graph indicates the maximum peak effective-index sensitivities $S_{e,\tau,max}$ that can be achieved. These implementations are marked with a white asterisk (*).

that, besides the decreased optoelectronic effective-index sensitivity, laser frequency noise can also add to the overall noise of the readout signal, thereby impairing the LoD—see Subsection 4.3d for a more detailed discussion. Note also that MZIs are not subject to any fundamental limitations related to the laser linewidth: by matching the group delays in the two arms, the MZI FSR $\Delta\omega_{FSR,MZI}$ can always be made much larger than any practically relevant laser linewidth.

4.2e. Sensitivity Comparison of Optimized Sensor Implementations

Assuming optimum device lengths L_{opt} and amplitude transmission factors $\rho_{1,opt}$ and $\rho_{2,opt}$ of the RR coupling sections, and neglecting detrimental effects that result from non-zero laser linewidths, we can calculate the peak optoelectronic effective-index sensitivity $S_{e,\tau,peak}$ and the fundamentally achievable maximum peak optoelectronic effective-index sensitivity $S_{e,\tau,max}$ of the various sensor concepts (see Appendix D for details). The results are indicated in Fig. 4(d), and the corresponding sensor parameters are summarized in Table 3. The right-hand part of Fig. 4(d) shows the maximum peak effective-index sensitivity $S_{e,\tau,max}$ of MZI with optimized arm lengths in different output configurations. The more complex implementations MZI_2 and MZI_3 allow us to enhance $S_{e,\tau,max}$ by using appropriate combinations of the output signals. Specifically, MZI_2 uses a balanced detection of two complementary photodiode currents, which allows us to double $S_{e,\tau,max}$ compared to MZI_1. Moreover, balanced detection leads to zero effective transmission τ_{OP} in the optimum operating point and, thereby, simplifies feedback control for operating point stabilization. MZI_3 provides the same sensitivity as MZI_2 and is additionally insensitive with respect to the operating point [39,41], eliminating the need of a feedback control for operating-point stabilization. The left-hand part of Fig. 4(d) shows $S_{e,\tau,peak}$ of typical RR-based sensor implementations.

For the same ring cavity, the RR_{AP} implementation generally outperforms the corresponding RR_{AD} concept by a factor of 4 due to the increased power loss introduced by the additional waveguide that is coupled to the RR_{AD} resonator. For both implementations, optimized UC operation leads to the maximum peak effective-index sensitivity $S_{e,\tau,max}$, which outperforms the best $S_{e,\tau,max}$ of CC operation by roughly 20%. For RR_{AD}, the optimized UC sensors are furthermore easier to reliably fabricate due to symmetric coupling gaps of the two tapping bus waveguides. The RR_{BD} exploits both the drop and through ports and increases $S_{e,\tau,max}$ by a factor of 3 compared to only using the drop port.

Moreover, RR_{BD}^{UC} implementations allow us to push the effective transmission τ_{OP} in the optimum operating point to zero, which simplifies feedback control for operating-point stabilization. Note that the optoelectronic effective-index sensitivity $S_{e,\tau}$ of an integrated phase-sensitive sensor can generally not be increased by using shorter operation wavelengths and, hence, larger wavenumbers $k_0 = \omega/c$, even though the normalization of the vertical axis by k_0/α might suggest this: for a given quantum efficiency of the PD, the electric readout responsivity $\Re$ is inversely proportional to

the photon energy and, hence, to the vacuum wavenumber, which exactly cancels the effect that the phase change is proportional to k_0.

Comparing broadly the various RR- or MZI-based sensor implementations, we find that the maximum peak effective-index sensitivity $S_{\mathrm{e},\tau,\max} \propto \alpha^{-1}$ is ultimately dictated by the modal power loss coefficient α. This can be intuitively understood: in RR, the ratio k_0/α is directly linked to the Q-factor since $k_0/\alpha = Q_\mathrm{i}/n_\mathrm{eg}$, as shown in Eq. (16), and, hence, the slope of the Lorentzian resonance, as shown in Eq. (20). In MZIs, k_0/α is related to the fundamental design trade-off between phase sensitivity and output contrast. The fundamental dependency of $S_{\mathrm{e},\tau,\max}$ on k_0 is eliminated due to the electric readout responsivity $\Re$, which accounts for the photodiode responsivity for the gain of any electrical readout amplifier, as well as for processing steps of the analog or digitized electric signals.

4.3. Limit of Detection

In Subsection 4.2, we have compared the different RR- and MZI-based sensor implementations in terms of their sensitivity toward a change Δn_e of the effective RI in the sensitive waveguide region. We will now quantify and compare the LoD, i.e., the smallest RI change Δn_e that can be detected by the various sensors. To this end, we assume that all deterministic influences can be eliminated by proper technology control, device design, and calibration, and we, thus, disregard fabrication errors and the corresponding waveguide/component errors or splitter/coupler/detector imbalances as well as absolute sensor temperature or stress. Note that controlling the impact of these deterministic errors is a complex task in its own right, and a wide range of approaches has been explored in the literature. Apart from improved fabrication processes [44,45] and error prediction [46], photonic components can be designed specifically for increased tolerance with respect to fabrication errors [47]. Moreover, waveguides or waveguide pairs in interferometer arms can be designed to minimize temperature effects [47–50], and on-chip as well as off-chip reference structures can be employed to compensate for environmental drift [27,51]. Factory calibration mechanisms can account for variations in the fabrication process [52], and advanced readout concepts and signal processing can dynamically recalibrate the sensor system at runtime [41]. Consequently, the remaining unavoidable measurement uncertainty and the associated LoD of the photonic sensor system are associated only with stochastic noise sources, which we analyze in the following paragraphs.

The noise propagation model is illustrated in Fig. 5. As noise sources ζ_n, we consider laser frequency and intensity (power) noise ω_n and $P_\mathrm{i,n}$ with variances $\sigma^2_{\omega_\mathrm{n}} = \overline{\omega^2_\mathrm{n}}$ and $\sigma^2_{P_\mathrm{i,n}} = \overline{P^2_\mathrm{i,n}}$, which partially result from noise $I_\mathrm{i,n}$ of the laser drive current [see Fig. 1(c)]. Note that our model treats the laser frequency and intensity (power) noise ω_n and $P_\mathrm{i,n}$ as statistically independent random variables and does not account for the exact dependence of these quantities on the drive current noise $I_\mathrm{i,n}$. This is illustrated by dashed lines in Fig. 5. We further include temperature fluctuations ϑ_n between the sensor and the co-integrated reference structure on the photonic chip, which are characterized by a variance $\sigma^2_{\vartheta_\mathrm{n}}$. In the model shown in Fig. 1(c), these temperature fluctuations are accounted for via a temperature-induced fluctuation $P_\mathrm{o,n}$ with variance $\sigma^2_{P_\mathrm{o,n}} = \overline{P^2_\mathrm{o,n}}$ of the optical sensor output power P_o. At the detector side, we consider the photocurrent shot noise $I_\mathrm{s,n}$ with variance $\sigma^2_{I_\mathrm{s,n}} = \overline{I^2_\mathrm{s,n}}$ as well as additional PD noise $I_\mathrm{NEP,n}$ with variance $\sigma^2_{I_\mathrm{NEP,n}} = \overline{I^2_\mathrm{NEP,n}}$, quantified by the so-called noise-equivalent power (NEP). Both of these noise currents contribute toward the total output-photocurrent noise $I_\mathrm{o,n}$ with variance $\sigma^2_{I_\mathrm{o,n}} = \overline{I^2_\mathrm{o,n}}$ [see Figs. 1(c) and 5]. We further account for quantization noise introduced by analog-to-digital conversion of the photocurrent, described by a quantization noise current $I_\mathrm{q,n}$ with variance

$\sigma^2_{I_{\mathrm{q,n}}} = \overline{I^2_{\mathrm{q,n}}}$. All these noise sources $\zeta_\mathrm{n} \in \{\vartheta_\mathrm{n};\, \omega_\mathrm{n};\, P_{\mathrm{i,n}};\, I_{\mathrm{s,n}};\, I_{\mathrm{NEP,n}};\, I_{\mathrm{q,n}}\}$ are treated as random variables with zero mean $\overline{\zeta_\mathrm{n}} = 0$ that have associated variances $\sigma^2_{\zeta_\mathrm{n}} = \overline{\zeta^2_\mathrm{n}}$. Note that the subscript "n" in these quantities refers to newly added noise in a certain stage of the sensor signal chain, in contrast to the noise that was accumulated from previous stages and that is denoted by symbols without subscript "n" [see Eq. (7)]. In the following, we assume for simplicity a unity propagation factor through the ADC, $|\partial I_\mathrm{q}/\partial I_\mathrm{o}|^2 = 1$, and add all three detection-related current noise variances to obtain the variance $\sigma^2_{I_\mathrm{q}} = \sigma^2_{I_{\mathrm{s,n}}} + \sigma^2_{I_{\mathrm{NEP,n}}} + \sigma^2_{I_{\mathrm{q,n}}}$ of the quantized output current I_q.

The propagation of these noise quantities and of the associated noise variances $\sigma^2_{\zeta_\mathrm{n}}$ through the system is illustrated in Fig. 5. Each noise variance $\sigma^2_{\zeta_\mathrm{n}}$ is associated with a noise propagation factor W_ζ that describes the propagation of $\sigma^2_{\zeta_\mathrm{n}}$ through the sensor system to the overall variance $\sigma^2_{\Delta n_{\mathrm{e,r}}}$ of the reconstructed effective RI change $\Delta n_{\mathrm{e,r}}$. In the illustration of Fig. 5, each noise propagation W_ζ is associated with a solid trace of the respective color that connects the variance of the respective noise source (colored ellipse) to the overall variance $\sigma^2_{\Delta n_{\mathrm{e,r}}}$ (green ellipse).

Assuming that the various noise sources are statistically independent, the overall variance $\sigma^2_{\Delta n_{\mathrm{e,r}}}$ can, thus, be expressed as a sum of the variances $\sigma^2_{\zeta_\mathrm{n}}$ weighted with the corresponding noise propagation factors W_ζ,

$$\sigma^2_{\Delta n_{\mathrm{e,r}}} = \sum_\zeta W_\zeta \sigma^2_{\zeta_\mathrm{n}}, \qquad W_\zeta = \left|\frac{\partial \Delta n_{\mathrm{e,r}}}{\partial \zeta_\mathrm{n}}\right|^2, \qquad \zeta_\mathrm{n} \in \left\{\vartheta_\mathrm{n};\, \omega_\mathrm{n};\, P_{\mathrm{i,n}};\, I_{\mathrm{s,n}};\, I_{\mathrm{NEP,n}};\, I_{\mathrm{q,n}}\right\},$$

$$\sigma^2_{\Delta n_{\mathrm{e,r}}} = \underbrace{W_\vartheta \sigma^2_{\vartheta_\mathrm{n}}}_{\sigma^2_{\Delta n_{\mathrm{e,r}},\vartheta}} + \underbrace{W_\omega \sigma^2_{\omega_\mathrm{n}}}_{\sigma^2_{\Delta n_{\mathrm{e,r}},\omega}} + \underbrace{W_{P_\mathrm{i}} \sigma^2_{P_{\mathrm{i,n}}}}_{\sigma^2_{\Delta n_{\mathrm{e,r}},P_\mathrm{i}}} + \underbrace{W_{I_\mathrm{s}} \sigma^2_{I_{\mathrm{s,n}}}}_{\sigma^2_{\Delta n_{\mathrm{e,r}},I_\mathrm{s}}} + \underbrace{W_{I_\mathrm{NEP}} \sigma^2_{I_{\mathrm{NEP,n}}}}_{\sigma^2_{\Delta n_{\mathrm{e,r}},I_\mathrm{NEP}}} + \underbrace{W_{I_\mathrm{q}} \sigma^2_{I_{\mathrm{q,n}}}}_{\sigma^2_{\Delta n_{\mathrm{e,r}},I_\mathrm{q}}}. \tag{21}$$

In this relation, the contribution of an individual noise source ζ_n to the uncertainty of the reconstructed effective RI $\Delta n_{\mathrm{e,r}}$ is quantified by the associated reconstruction variances $\sigma^2_{\Delta n_{\mathrm{e,r}},\zeta} = W_\zeta \sigma^2_{\zeta_\mathrm{n}}$. In order to quantify the total LoD according to Eq. (8), we calculate the 3σ − deviation of the reconstructed effective RI $\Delta n_{\mathrm{e,r}}$ that results from the various noise contributions according to Eq. (21).The following sections are dedicated to the detailed quantification of all discussed noise-related terms, i.e., the noise variances $\sigma^2_{\zeta_\mathrm{n}}$ (Subsection 4.3a), the corresponding noise propagation factors W_ζ (Subsection 4.3b), and the associated reconstruction variances $\sigma^2_{\Delta n_{\mathrm{e,r}},\zeta}$ (Subsection 4.3c). This allows us to perform a quantification and comparison of the LoD (Subsection 4.3d) for each RR- and MZI-based sensor implementation. The mathematical details on the noise variances, noise propagation factors, and reconstruction variances are summarized in Table 4.

4.3a. Noise Variances

Regarding temperature variations, we assume that the absolute temperature of the sensor can be accounted for by proper stabilization, calibration, and referencing [49], and that the sensor and the reference structures are based on waveguides with negligible differences in thermo-optic coefficients (TOCs) [50]. Note that, in general, on-chip temperature variations do not affect MZIs and RRs alike. For MZIs, the temperature-dependent behavior of the power splitter at the input and the power combiner at the output, typically realized as MMIs or directional couplers, as well as of the waveguides in the sensor and reference arms have to be taken into account. For the couplers, careful design can at least reduce the impact of temperature fluctuations, whereas temperature-induced shifts of the phase difference between sensor and reference arms can be largely suppressed by balancing arm lengths and waveguide TOCs.

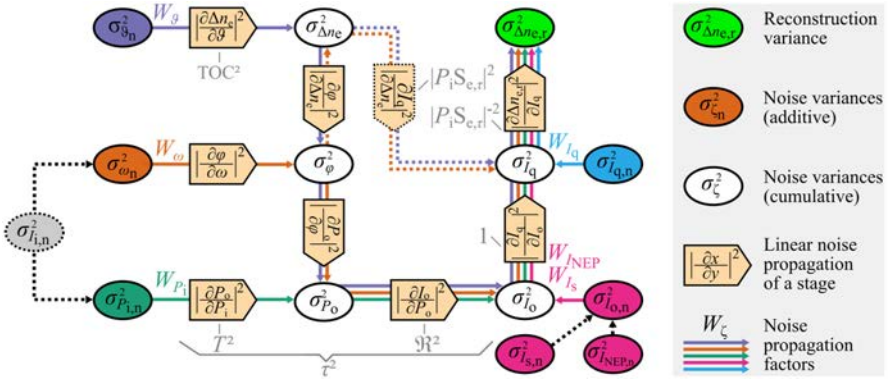

Illustration of the noise propagation. The individual noise quantities $\zeta_\mathrm{n} \in \{\vartheta_\mathrm{n};\, \omega_\mathrm{n};\, P_\mathrm{i,n};\, I_\mathrm{s,n};\, I_\mathrm{NEP,n};\, I_\mathrm{q,n}\}$ with associated additive noise variances $\sigma^2_{\zeta_\mathrm{n}}$, indicated by filled colored ellipses, propagate through different stages of the sensor system and contribute to cumulative noise variances of the intermediate quantities $\sigma^2_{\Delta n_\mathrm{e}}$, σ^2_{φ}, $\sigma^2_{P_\mathrm{o}}$, $\sigma^2_{I_\mathrm{o}}$, and $\sigma^2_{I_\mathrm{q}}$, all indicated by white ellipses. For simplicity, we assume all noise quantities to be uncorrelated, such that the variances of the respective contributions toward the overall reconstruction variance $\sigma^2_{\Delta n_\mathrm{e,r}}$ may simply be added [see Eq. (21)]. We consider laser frequency noise ω_n (brown) and intensity (power) noise $P_\mathrm{i,n}$ (dark green) with variances $\sigma^2_{\omega_\mathrm{n}} = \overline{\omega^2_\mathrm{n}}$ and $\sigma^2_{P_\mathrm{i,n}} = \overline{P^2_\mathrm{i,n}}$, neglecting a potential correlation of these quantities, which might result from their joint dependence on laser drive current noise $I_{i,n}$ with variance $\sigma^2_{I_\mathrm{i,n}} = \overline{I^2_\mathrm{i,n}}$. We further consider temperature fluctuations ϑ_n (purple) between the sensor and the co-integrated reference structure on the photonic chip, which feature a variance $\sigma^2_{\vartheta_\mathrm{n}}$. At the detector side, our model includes the photocurrent shot noise $I_\mathrm{s,n}$ with variance $\sigma^2_{I_\mathrm{s,n}} = \overline{I^2_\mathrm{s,n}}$ as well as additional photodetector noise $I_\mathrm{NEP,n}$ with variance $\sigma^2_{I_\mathrm{NEP,n}} = \overline{I^2_\mathrm{NEP,n}}$, quantified by the so-called noise-equivalent power (NEP), both contributing toward the total photocurrent noise $I_{o,n}$ at the sensor output with variance $\sigma^2_{I_\mathrm{o,n}} = \overline{I^2_\mathrm{o,n}}$ (magenta). We further account for quantization noise introduced by the digital-to-analog conversion of the photocurrent I_o, described by the quantization noise current $I_\mathrm{q,n}$ with variance $\sigma^2_{I_\mathrm{q,n}} = \overline{I^2_\mathrm{q,n}}$ (blue). The noise propagation factors W_ζ from each noise variance σ^2_ζ to the reconstruction variance $\sigma^2_{\Delta n_\mathrm{e,r}}$ (light green) of the effective refractive index $\Delta n_{e,r}$ are depicted by solid traces of the color associated with the respective noise source. The various noise propagation factors W_ζ are obtained by multiplying the linearized small-signal power transmission factors of the stages along the respective noise path. These small-signal power transmission factors of the various stages are indicated in arrow-shaped ochre fields, with simplified expressions in gray next to the respective field. The calculation of the noise propagation factors W_ω and W_ϑ can be simplified by skipping the explicit calculation of the error propagation via the intermediate quantities σ^2_φ, $\sigma^2_{P_\mathrm{o}}$, $\sigma^2_{I_\mathrm{o}}$, and $\sigma^2_{I_\mathrm{q}}$, but instead taking the detour indicated by the dotted lines. To this end, we first translate the temperature fluctuations ϑ_n or the frequency noise fluctuations ω_n into equivalent fluctuations of the effective refractive index n_e, which are then propagated to the cumulative variance $\sigma^2_{I_\mathrm{q}}$ of the quantized output current by reusing the results from the sensitivity calculations of Subsection 4.2, $|\partial I_\mathrm{q}/\partial \Delta n_\mathrm{e}|^2 = |P_\mathrm{i} S_{\mathrm{e},\tau}|^2$. As this term cancels with the term $|P_\mathrm{i} S_{\mathrm{e},\tau}|^{-2}$ associated with the reconstruction of the effective-index change $\Delta n_{e,r}$ from the quantized output current I_q, we obtain simple expressions for the impact of these two noise sources on the associated reconstruction variance, $\sigma^2_{\Delta n_\mathrm{e},\vartheta} = \mathrm{TOC}^2 \sigma^2_{\vartheta_\mathrm{n}}$ and $\sigma^2_{\Delta n_\mathrm{e},\omega} = (n_\mathrm{eg}/\omega)^2 \sigma^2_{\omega_\mathrm{n}}$ (RR), and $\sigma^2_{\Delta n_\mathrm{e},\omega} = 0$ (MZI with group-delay-matched arms).

In case of a balanced MZI with athermal couplers, the output signal is not distorted by absolute temperature drifts that affect both arms alike, as the MZI reference arm inherently acts as a temperature reference. For RRs, the temperature-dependent properties of the coupling section as well as of the sensor waveguide within the resonator have to be taken into account, which can again both be reduced via athermal designs. However, in contrast to MZIs, there is no configuration that inherently compensates the temperature dependence of the phase shift in the RR waveguide, and a dedicated reference RR has to be added for independent measurement of the temperature-dependent behavior. The data measurement from the reference structure can then be used for compensating the temperature dependence, e.g., by suitable feedback control or signal processing techniques. In general, sensor and reference waveguides should be routed in close proximity and with good thermal coupling to one another, ideally using interleaved circuit layouts that eliminate the impact of on-chip temperature gradients [53]. In addition, further temperature reference structures can be included on a chip or package level to eliminate the impact of global temperature offsets by appropriate signal processing techniques.

As a consequence, stochastic on-chip temperature fluctuations remain as the only noise contribution. These fluctuations are quantified by the variance $\sigma_{\vartheta_\mathrm{n}}^2$ of the temperature difference between the photonic sensor and the corresponding reference structure, which contribute to output power fluctuations $P_{\mathrm{o,n}}$ of the sensor. For MZIs, $\sigma_{\vartheta_\mathrm{n}}^2$ relates to the variance of the temperature difference between the two interferometer arms, whereas for RRs, $\sigma_{\vartheta_\mathrm{n}}^2$ represents the variance of the temperature difference between the sensor ring and the corresponding reference ring.

Table 4. Quantification of Various Noise Sources Along with the Corresponding Noise Propagation Factors as Defined in Eq. (21) and Fig. 5[a,b,c,d,e]

		Temperature $\zeta_\mathrm{n} = T_\mathrm{n}$	Laser Frequency $\zeta_\mathrm{n} = \omega_\mathrm{n}$	Laser Intensity $\zeta_\mathrm{n} = P_{\mathrm{i,n}}$	PD Shot Noise $\zeta_\mathrm{n} = I_{\mathrm{s,n}}$	PD NEP $\zeta_\mathrm{n} = I_{\mathrm{NEP,n}}$	Quantization $\zeta_\mathrm{n} = I_{\mathrm{q,n}}$
Noise variances	$\sigma_{\zeta_\mathrm{n}}^2$	$\sigma_{T_\mathrm{n}}^2$	$4\pi^2 \int_0^{\Delta f} S_\mathrm{F}(f)\,\mathrm{d}f$	$P_\mathrm{i}^2 \int_0^{\Delta f} S_\mathrm{RIN}(f)\,\mathrm{d}f \cong P_\mathrm{i}^2 \mathrm{RIN}\Delta f$	$2q_\mathrm{e} I_\mathrm{o} \Delta f$	$\Re^2 \mathrm{NEP}^2 \Delta f$	$\frac{\mathrm{LSB}^2}{12} = \frac{I_{\mathrm{o,max}}^2 2^{-2N}}{12}$
Noise propagation factors	W_ζ	TOC^2	$\left(\frac{\partial \varphi_\mathrm{OP}}{\partial \omega}\right)^2 \left(\frac{1}{k_0 L}\right)^2$	$\left(\frac{1}{P_i}\right)^2 \left(\frac{\lvert\tau\rvert}{S_{\mathrm{e},\tau}}\right)^2$	$\left(\frac{1}{P_i}\right)^2 \left(\frac{1}{S_{\mathrm{e},\tau}}\right)^2$	$\left(\frac{1}{P_i}\right)^2 \left(\frac{1}{S_{\mathrm{e},\tau}}\right)^2$	$\left(\frac{1}{P_i}\right)^2 \left(\frac{1}{S_{\mathrm{e},\tau}}\right)^2$
Reconstruction variances	$\sigma_{\Delta n_{\mathrm{e,r}},\zeta}^2$	$\mathrm{TOC}^2 \sigma_{T_\mathrm{n}}^2$	$\left(\frac{\sigma_{\omega_\mathrm{n}}}{\omega}\right)^2$	$\left(\frac{\alpha}{k_0}\right)^2 \mathrm{RIN}\Delta f$	$\left(\frac{\alpha}{k_0}\right)^2 \frac{q_\mathrm{e}\Delta f}{\Re P_\mathrm{i}}$	$\left(\frac{\alpha}{k_0}\right)^2 \frac{\mathrm{NEP}^2 \Delta f}{P_\mathrm{i}^2}$	$\left(\frac{\alpha}{k_0}\right)^2 \frac{2^{-2N}}{12}$
Relative implementation impairments	$\mathrm{RR}_{\mathrm{AP}}^{\mathrm{CC}}$	$\times 1$	$\times n_\mathrm{eg}^2$	$\times 4/27$	$\times 32/27$	$\times 64/27$	$\times 64/27$
	$\mathrm{RR}_{\mathrm{AP}}^{\mathrm{UC}}$			$\times 9/48$	$\times 54/48$	$\times 27/16$	$\times 4/3$
	$\mathrm{RR}_{\mathrm{AD}}^{\mathrm{CC}}$			$\times 16/3$	$\times 256/9$	$\times 1024/27$	$\times 256/27$
	$\mathrm{RR}_{\mathrm{AD}}^{\mathrm{UC}}$			$\times 3$	$\times 18$	$\times 27$	$\times 16/3$
	$\mathrm{RR}_{\mathrm{BD}}^{\mathrm{UC}}$			$\times 0$	$\times 2$	$\times 6$	$\times 16/3$
	MZI_1	$\times 1$	$\times \underbrace{\left(\Delta n_{\mathrm{eg},0} - n_\mathrm{eg}\frac{\Delta L}{L}\right)}_{=0(*)}$	$\times 1$	$\times 4\mathrm{e}$	$\times 4\mathrm{e}$	$\times 4$
	MZI_2			$\times 0$	$\times 2\mathrm{e}$	$\times 2\mathrm{e}$	$\times 4$
	MZI_3			$\times 0$	$\times 2\mathrm{e}$	$\times 6\mathrm{e}$	$\times 8/3$

[a]The columns refer to different noise sources ζ_n within the sensor system, which contribute to the total limit of detection (LoD).

[b]The second and the third row relate to analytic descriptions of the individual noise variances $\sigma_{\zeta_\mathrm{n}}^2$ at their origin and to the corresponding noise propagation factors W_ζ through the sensor system to the reconstructed value of the effective-index change $\Delta n_{\mathrm{e,r}}$.

[c]The subsequent rows describe the associated reconstruction variances $\sigma_{\Delta n_{\mathrm{e,r}},\zeta}^2$ that contribute to the uncertainty of $\Delta n_{\mathrm{e,r}}$ and that, thus, quantify the minimum detectable refractive-index change.

[d]Note that these reconstruction variances are split up into base expressions for each noise source, which are identical for all sensor implementations, fourth line, as well as into implementation-dependent multiplication factors, which show the implementation-specific impairments for the operating points according to Table 3.

[e]For RR, impairments by laser frequency noise are unavoidable. In case of MZI, the impact of laser frequency noise can be diminished by using symmetric devices with matched group delays in the two interferometer arms, leading to a zero multiplication factor, indicated by an asterisk (*).

Regarding laser frequency fluctuations, it is not possible to state a universal analytical expression for $\sigma^2_{\omega_\mathrm{n}}$ since frequency noise spectra of integrated lasers differ strongly. In theory, the variance $\sigma^2_{\omega_\mathrm{n}}$ of the laser frequency fluctuation can be obtained by integrating the one-sided laser frequency noise spectrum $S_\mathrm{F}(f)$ over the relevant frequency interval $[1/T_\mathrm{obs}, \Delta f]$, where T_obs denotes the overall observation during a complete set of measurements while Δf denotes the electronic acquisition bandwidth of the sensor system [see also Eq. (39) in Appendix E]. In practice, however, this approach is hard to apply, since the laser frequency noise spectrum $S_\mathrm{F}(f)$ usually increases strongly toward small Fourier frequencies $f \to 0$ such that the integral diverges for $T_\mathrm{obs} \to \infty$. Specifically, real lasers without frequency stabilization are typically subject to slow frequency drift, which leads to an additional $1/f^\gamma$-part in the frequency noise spectrum, where γ typically lies between 0 and 2 [54]. For most sensor systems with typical acquisition bandwidths Δf in the kHz or the lower MHz range, the contribution of this $1/f^\gamma$-part dominates the variance $\sigma^2_{\omega_\mathrm{n}}$ of the frequency fluctuations, while the spectrally white frequency noise background can be neglected. As a consequence, the intrinsic linewidth of the laser source, which is given by the spectrally white component of the frequency noise, is often not a relevant metric for laser sources in integrated phase-sensitive photonic sensors. For a given laser source, the frequency fluctuations usually have to be measured individually using, e.g., a heterodyne technique (see Appendix E for details).

The variance of the laser output power fluctuation is denoted as $\sigma^2_{P_\mathrm{i,n}}$ and can be calculated from the relative intensity noise (RIN) spectrum $S_\mathrm{RIN}(f)$, which is often expressed in dB Hz^{-1} [55]. Note that for the typically small electronic acquisition bandwidths Δf employed in sensing applications, the RIN spectrum is mostly flat. The input power variance can, hence, be approximated as $\sigma^2_{P_\mathrm{i,n}} = P_\mathrm{i}^2\,\mathrm{RIN}\,\Delta f$, where the quantity RIN refers to the constant, one-sided spectral density $S_\mathrm{RIN}(f)$ in the limit of low frequencies and is a commonly used performance metric for lasers. Note that both $\sigma^2_{P_\mathrm{i,n}}$ and $\sigma^2_{\omega_\mathrm{n}}$ may sensitively depend on the fluctuations of the laser drive current as well as on temperature fluctuations of the laser, in which case the respective variances may be correlated. For simplicity, we neglect this effect in our analysis.

The variance $\sigma^2_{I_\mathrm{o,n}}$ of the PD output current fluctuations comprises both the photocurrent shot noise as well as additional noise contributions of the detector circuit such as thermal noise and dark-current shot noise, which, for a given device, are often quantified by the NEP. For a given internal noise level, the NEP specifies the optical input power of the PD that leads to a signal-to-noise ratio of one at the output. Photocurrent shot noise is characterized by the variance $\sigma^2_{I_\mathrm{s,n}} = 2q_\mathrm{e}I_\mathrm{o}\Delta f$, here expressed as a function of the average output current I_o in the operating point, the acquisition bandwidth Δf, and the elementary charge q_e [56]. In contrast to that, the NEP-related current noise is independent of the actual signal level and features a variance $\sigma^2_{I_\mathrm{NEP,n}} = \Re^2\mathrm{NEP}^2\Delta f$[57]. In this relation, $\Re$ denotes the electric readout responsivity that accounts for the responsivity of the PD and for any optional subsequent amplifiers (see Subsection 4.2a). Furthermore, Δf is the electronic acquisition bandwidth, and the NEP level, specified in W/$\sqrt{\mathrm{Hz}}$, is assumed to be constant within $0 < f < \Delta f$.

Finally, we consider quantization noise originating from a finite ADC resolution of N bits, which does not depend on the acquisition bandwidth Δf. The quantization process introduces an erroneous current $I_\mathrm{q,n}$ characterized by the associated variance $\sigma^2_{I_\mathrm{q,n}} = \mathrm{LSB}^2/12$ [58], where LSB is the quantization step corresponding to the least significant bit as defined by the ADC range as well as resolution N. Since we need to tune the sensors to the optimum operating point, and since we assume that we cannot reliably set the initial operating point by design, the ADC has to cover the whole range

from zero output current to maximum output current $I_{\mathrm{o,max}}$ at each output port, and, thus, $\mathrm{LSB} = I_{\mathrm{o,max}} 2^{-N}$.

The equations required to calculate the noise variances $\sigma_{\zeta_\mathrm{n}}^2$ for all noise sources ζ_n are listed in Row 2 of Table 4. The noise variance models above show that the acquisition bandwidth Δf is a major factor for the noise analysis. The measurement bandwidth is connected to the integration time T_{int} and to the minimum required sampling frequency f_s by $T_{\mathrm{int}} = 1/f_s = 1/(2\Delta f)$. Except for quantization noise, choosing an appropriate integration time is, hence, crucial for the sensor performance. The relations shown in Row 2 of Table 4 indicate that the noise variances $\sigma_{P_{\mathrm{i,n}}}^2$, $\sigma_{I_{\mathrm{s,n}}}^2$, and $\sigma_{I_{\mathrm{NEP,n}}}^2$ of the laser RIN as well as of the PD shot noise and NEP decrease for smaller acquisition bandwidths Δf or longer integration times T_{int}, i.e., longer averaging pays off and can eventually render the impact of these noise sources insignificant. In contrast to this, the stochastic processes describing temperature and laser frequency noise are not mean-free, thus leading to reconstruction variances that eventually grow with longer integration times. This can be quantified by the respective Allan variances [59], which exhibit typical bathtub-like characteristics when plotted as a function of integration time. To obtain reliable results for measurements with long observation times T_{obs}, the non-stationary portions of these noise sources have to be eliminated by suitable stabilization or referencing systems. A detailed discussion with respect to laser frequency noise can be found in Appendix F.

4.3b. Noise Propagation Factors

The noise propagation factors W_ζ for each noise source ζ_n can be obtained following the concept of the noise propagation model described in Fig. 5, where we again use linear approximations for all transmission functions in the respective operating point. The resulting noise propagation factors are specified in Table 4, Row 3.

To explain these relations, let us first consider the propagation factor W_{I_s} related to PD shot noise with variance $\sigma_{I_{\mathrm{s,n}}}^2$ (see Column 5 in Row 3 of Table 4), which translates into an equivalent reconstruction variance $\sigma_{\Delta n_{\mathrm{e,r}}, I_\mathrm{s}}^2 = W_{I_\mathrm{s}} \sigma_{I_{\mathrm{s,n}}}^2$ of the reconstructed effective RI change $\Delta n_{\mathrm{e,r}}$ (see also Fig. 5). For calculating the noise propagation factor W_{I_s}, we exploit the fact that changes of the effective-index are related to changes of the output current via the optoelectronic effective-index sensitivity $\partial I_\mathrm{o}/\partial n_\mathrm{e} = P_\mathrm{i} S_{\mathrm{e},\tau}$ (see last column of Table 3 for the corresponding expressions of the various sensor implementations). The reconstruction algorithm of a properly calibrated sensor exactly inverts this relationship such that the contribution $\sigma_{\Delta n_{\mathrm{e,r}}, I_\mathrm{s}}^2$ of the shot noise to the variance of the reconstructed effective-index change $\Delta n_{\mathrm{e,r}}$ can be expressed as $\sigma_{\Delta n_{\mathrm{e,r}}, I_\mathrm{s}}^2 = \sigma_{I_{\mathrm{s,n}}}^2 / |P_\mathrm{i} S_{\mathrm{e},\tau}|^2$. The overall noise propagation factor can, thus, be written as $W_{I_\mathrm{s}} = |P_\mathrm{i} S_{\mathrm{e},\tau}|^{-2}$. This noise propagation factor does not only apply to shot noise but can generally be used to calculate the contribution of any current noise to the uncertainty of the reconstructed effective RI $\Delta n_{\mathrm{e,r}}$, $W_{I_\mathrm{s}} = W_{I_\mathrm{q}} = W_{I_{\mathrm{NEP}}}$ (see Columns 6 and 7 in Row 3 of Table 4). In the case of laser RIN, the associated noise propagation factor $W_{\mathrm{RIN}} = |\tau|^2 W_{I_\mathrm{o}} = |\tau|^2 |P_\mathrm{i} S_{\mathrm{e},\tau}|^{-2}$ additionally contains the squared magnitude of the effective optoelectronic transmission $|\tau|^2$, which describes the translation of the input power variance $\sigma_{P_\mathrm{i}}^2$ to a contribution toward the variance $\sigma_{I_\mathrm{o}}^2$ of the sensor output current I_o (see Column 4 in Row 3 of Table 4). Hence, all four noise sources considered so far, i.e., laser intensity noise, photodiode shot noise, photodiode NEP noise, and quantization noise, have a noise propagation factor that is proportional to $|P_\mathrm{i} S_{\mathrm{e},\tau}|^{-2}$. For these noise contributions, a large sensitivity always helps to reduce the associated LoD.

The remaining noise sources are on-chip temperature fluctuations ϑ_n and laser frequency noise ω_n (see Columns 2 and 3 in Row 3 of Table 4). Both effects have direct

impact on the phases φ_{RR} and φ_{MZI} according to Eqs. (9) and (11). For these noise sources, the noise propagation factors W_ϑ and W_ω are finally independent of the sensitivity-related term $|P_\mathrm{i} S_{\mathrm{e},\tau}|^2$.

In the case of temperature fluctuations, the noise propagation factor W_ϑ can be obtained by calculating the relationship between a temperature-difference fluctuation ϑ_n and the corresponding fluctuation $\Delta n_{\mathrm{e},\vartheta} = \mathrm{TOC}\,\vartheta_n$ of the effective-index difference between the sensor and the reference waveguide. The propagation of this effective-index perturbation $\Delta n_{\mathrm{e},\vartheta}$ to the output current I_o and the subsequent propagation through the reconstruction algorithm are given by $|P_\mathrm{i} S_{\mathrm{e},\tau}|^2$ and $|P_\mathrm{i} S_{\mathrm{e},\tau}|^{-2}$, respectively, such that the net effect cancels. This leads to a noise propagation factor $W_\vartheta = \mathrm{TOC}^2\,|P_\mathrm{i} S_{\mathrm{e},\tau}|^2 |P_\mathrm{i} S_{\mathrm{e},\tau}|^{-2} = \mathrm{TOC}^2$ as indicated in Row 3, Column 2 of Table 4. In the graphical illustration of the noise propagation model in Fig. 5, this corresponds to a detour in the noise propagation path as illustrated by the purple dashed line, which directly connects the variance $\sigma^2_{\Delta n_\mathrm{e}}$ of the RI difference with the variance $\sigma^2_{I_\mathrm{q}}$ of the quantized output current. The propagation factor W_ω for laser frequency noise can be obtained in a similar way by considering the associated shift of the sensor operating point φ_{OP}. To this end, we again calculate the equivalent effective RI change $\Delta n_{\mathrm{e},\omega}$ that would lead to the same operating-point phase shift $\Delta\varphi_{\mathrm{OP}}$ as a laser frequency shift ω_n. The two quantities are related by $\Delta n_{\mathrm{e},\omega} = (\partial\varphi_{\mathrm{OP}}/\partial\Delta n_\mathrm{e})^{-1}(\partial\varphi_{\mathrm{OP}}/\partial\omega)\omega_n = (-1/k_0 L)(\partial\varphi_{\mathrm{OP}}/\partial\omega)\omega_n$. The propagation of the effective-index perturbation $\Delta n_{\mathrm{e},\omega}$ to the output current I_o and the subsequent propagation through the reconstruction algorithm does again not have any overall effect, thus leading to a noise propagation factor $W_\omega = (1/k_0 L)^2(\partial\varphi_{\mathrm{OP}}/\partial\omega)^2$ (see Column 3 in Row 3 of Table 4 as well as brown dashed signal propagation in Fig. 5). For RRs, this simplifies to $W_\omega = (n_{\mathrm{eg}}/\omega)^2$, where $n_{\mathrm{eg}} = n_\mathrm{e} + \omega(\mathrm{d}n_\mathrm{e}/\mathrm{d}\omega)$ denotes the group RI of the waveguide mode that is subject to the frequency fluctuation. In the case of MZIs, the frequency dependence $\partial\varphi_{\mathrm{OP,MZI}}/\partial\omega$ of the phase difference in the operating point can be approximated by $\partial\varphi_{\mathrm{OP,MZI}}/\partial\omega \approx (\varphi_{\mathrm{OP,MZI}}/\omega) \times (n_{\mathrm{eg}}/n_\mathrm{e})$ [see Eq. (E1) in Appendix E].

4.3c. Reconstruction Variances

With the help of the noise variances $\sigma^2_{\zeta_\mathrm{n}}$ and the noise propagation factors W_ζ explained in the previous two paragraphs, we now calculate the individual contributions $\sigma^2_{\Delta n_{\mathrm{e,r},\zeta}} = W_\zeta \sigma^2_{\zeta_\mathrm{n}}$ of each noise source ζ_n to the overall reconstruction variance $\sigma^2_{\Delta n_{\mathrm{e,r}}}$ of the reconstructed effective RI in the sensitive region. For better comparison, we split up the results into noise-type-specific base expressions, which are identical for all sensor implementations (fourth row of Table 4), as well as into sensor-implementation-dependent multiplication factors (subsequent rows of Table 4).

It is important to note that the reconstruction variances $\sigma^2_{\Delta n_{\mathrm{e,r},\zeta}}$ depend on the operating point and that the implementation-dependent factors shown in Table 4 are only valid in the optimum operating points, as defined in Eq. (18) for RRs and Eq. (19) for MZIs. In these operating points, we can use specific values for the optoelectronic transmission $\tau = \tau_{\mathrm{OP}}$ and the optoelectronic effective-index sensitivity $S_{\mathrm{e},\tau} = S_{\mathrm{e},\tau,\mathrm{peak}}$ or $S_{\mathrm{e},\tau} = S_{\mathrm{e},\tau,\mathrm{max}}$ (see Table 3). Outside the optimum operating point, the reconstruction variances $\sigma^2_{\Delta n_{\mathrm{e,r},\zeta}}$ can be obtained by calculating τ and $S_{\mathrm{e},\tau}$ from the generic transmission according to Eqs. (10) and (12) along with the relations of τ according to Column 2 of Table 2. Note that in the case of multi-output implementations such as the MZI_2, MZI_3, and $\mathrm{RR}_{\mathrm{BD}}$, the implementation-dependent factors of the reconstruction variances $\sigma^2_{\Delta n_{\mathrm{e,r},\zeta}}$ can include covariance terms that result from correlations of the noise in the different output signals. As an example, the current fluctuations

of the different output signals caused by laser RIN are correlated, while the current fluctuations originating from the NEP or the shot noise of the various PDs are not.

Regarding laser frequency noise, impairments are unavoidable for RR-based sensor implementations. In contrast to this, the impact of laser frequency noise in MZI-based schemes can be diminished by using symmetric devices with matched group delays in the two interferometer arms, leading to a zero multiplication factor as indicated by an asterisk in Table 4.

4.3d. LoD Comparison of Optimized Sensor Implementations

With a fully quantified noise analysis according to Table 4 at hand, we now compare the different sensor implementations and discuss the impact of each noise source on the associated LoD. The results of this analysis are visualized in Fig. 6. In a first step, we analyze the contributions of the different noise sources to the LoD—the results are plotted in the first row and denoted as Fig. 6(a). We then compare how the individual sensor and readout implementations are affected by each noise source—this is shown in the second row and denoted as Fig. 6(b). Finally, we quantitatively estimate typical contributions of the various noise sources to the LoD and identify dominating effects for each sensor implementation [see Fig. 6(c)].

LoD as a function of noise-source parameters. The individual contributions $\sigma^2_{\Delta n_{\mathrm{e,r}},\zeta}$ of the various noise source ζ_{n} to the overall variance $\sigma^2_{\Delta n_{\mathrm{e,r}}}$ of the reconstructed effective-index difference $\Delta n_{\mathrm{e,r}}$ can be used to calculate the associated individual LoD contributions $\mathrm{LoD}_\zeta = 3\sigma_{\Delta n_{\mathrm{e,r}},\zeta}$, each of which corresponds to the sensors' total LoD in case all other noise sources are negligible. If several noise sources are relevant, the overall LoD can be calculated as the square root of the sum of squares of the individual LoD, where we assume for simplicity that the various noise sources are statistically independent,

$$\mathrm{LoD} = \sqrt{\sum\nolimits_\zeta \mathrm{LoD}_\zeta^2}. \tag{22}$$

Each individual LoD_ζ is plotted for all noise sources in Fig. 6(a), each as a function of typical underlying noise variances and/or other key parameters of the associated noise source. According to Table 4, the LoD_ζ of all noise sources that directly affect the signal level, i.e., the laser intensity noise ($\zeta_{\mathrm{n}} = P_{\mathrm{i,n}}$), the PD shot noise ($\zeta_{\mathrm{n}} = I_{\mathrm{s,n}}$), and NEP ($\zeta_{\mathrm{n}} = I_{\mathrm{NEP,n}}$), and the quantization noise ($\zeta_{\mathrm{n}} = I_{\mathrm{q,n}}$) are all proportional to α/k_0. For the plots in Fig. 6(a), we assume a rather large $\alpha/k_0 = 5 \times 10^{-5}$, which corresponds to a silicon waveguide with 10 dB/cm at $\lambda = 1.55$ μm. As a comparison, a silicon nitride waveguide with 2.3 dB/cm at $\lambda = 0.6$ μm yields $\alpha/k_0 = 5 \times 10^{-6}$ and, thus, reduces the contributions of these four noise sources by an order of magnitude. We assume an effective group RI of $n_{\mathrm{eg}} = 4$ for the sensor waveguides, which is a typical number in silicon photonics and which is only relevant for the frequency noise-related LoD_ω (see the third column of Table 4). We further assume an acquisition bandwidth of $\Delta f = 100$ Hz, which generally impacts all but the quantization-noise-related $\mathrm{LoD}_{I_{\mathrm{q}}}$. Note that the contribution LoD_ϑ of temperature fluctuations also depends on the acquisition bandwidth, even if we do not account for a quantitative relationship in our model. Furthermore, we assume perfect photodiodes with a quantum efficiency of one, which are only affected by PD shot noise. Regarding the effective optical input power P_{i}, we do not make any assumption in the context of Fig. 5(a) but treat it as a variable parameter that can change over many orders of magnitude [see Column 4 of Fig. 5(a)]. The effective input power P_{i} is only relevant for the contributions $\mathrm{LoD}_{I_{\mathrm{s}}}$ and $\mathrm{LoD}_{I_{\mathrm{NEP}}}$ from PD shot noise and NEP noise, while the LoD contributions of all other noise sources are independent

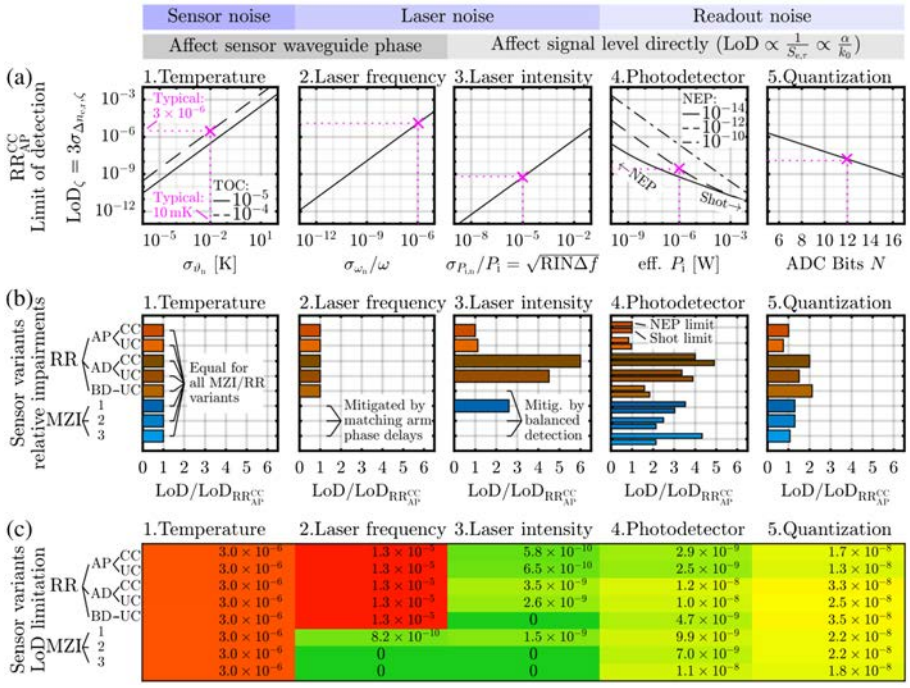

Limit of detection (LoD) for measured effective-refractive-index changes in various RR- and MZI-based sensor implementations. The individual contributions LoD_ζ of the various noise sources ζ_n are calculated using the equations in Table 4 and are plotted in Columns 1–5. Assuming for simplicity that the noise sources ζ_n are statistically independent, the overall LoD can be calculated as the square root of the sum of squares of the individual LoD_ζ, as shown in Eq. (22). The LoD_ζ, resulting from noise sources that directly affect the signal level, are proportional to α/k_0, which is set to $\alpha/k_0 = 5 \times 10^{-5}$ in this plot. For LoD_ω originating from laser frequency noise, we assume $n_\mathrm{eg} = 4$ to quantify the impact on RR-based sensor implementations. The choice for α/k_0 and n_eg reflect the situation for typical silicon photonic waveguides. For $\mathrm{LoD}_{I_\mathrm{s}}$ originating from photodetector shot noise, we assume perfect photodiodes with $\Re = q_\mathrm{e}/(\hbar\omega)$, and we assume an acquisition bandwidth of $\Delta f = 100\,\mathrm{Hz}$. (a) Individual LoD_ζ contributions of the various noise sources ζ_n plotted for the $\mathrm{RR}^{\mathrm{CC}}_{\mathrm{AP}}$ sensor implementation as a reference. Dotted magenta lines indicate typical cases found in integrated sensors. The impact of temperature fluctuations between sensor and reference structures is plotted for two different thermo-optic coefficients (TOCs), as shown in Column 1. The impacts of photodetector shot noise and noise-equivalent power are plotted as a function of the effective optical input power P_i defined in Eq. (2) for three different noise-equivalent power (NEP) levels, as shown in Column 4. Depending on P_i and NEP, the device is either shot-noise-limited or NEP-limited. (b) LoD impairments of various sensor implementations with respect to the $\mathrm{RR}^{\mathrm{CC}}_{\mathrm{AP}}$ considered as a reference case in (a). The LoD impairments of these implementations differ from that of the $\mathrm{RR}^{\mathrm{CC}}_{\mathrm{AP}}$ by constant factors, which are indicated by colored bars. A missing bar indicates that the respective sensor implementation is not prone to this specific noise source. Temperature fluctuations have the same impact on all sensor implementations. Laser frequency noise is a problem only for RR-based sensors. For the MZI, the impact on the LoD can be mitigated by matching the group delay of the sensor and reference arm, which effectively decouples the effective-index sensitivity from a sensitivity toward frequency noise. Laser intensity noise can be mitigated by sensor implementations using multiple output ports that measure power differences rather than absolute levels. For the photodetector noise sources, we consider the

two extreme cases of shot-noise limitation (lower bar) and NEP limitation (upper bar). For quantization noise, the ADC ranges are scaled to capture the full contrast of the respective current. (c) LoD bottlenecks of the various sensor implementations compared on a logarithmic color scale for the typical noise parameters marked by dashed magenta lines in (a). For these parameters, noise sources affecting the sensor waveguide phase, i.e., sensor temperature variations and, in case of RR-based implementations, laser frequency fluctuations, have the largest impact on the LoD, whereas the impact of intensity, photodetector, and quantization noise is manageable.

of P_i. For the sake of visual clarity, we restrict our analysis of the various LoD_ζ in Fig. 6(a) to only one sensor implementation, namely a CC all-pass RR ($\mathrm{RR}_\mathrm{AP}^\mathrm{CC}$), which serves as a reference for the subsequent discussion. For all other sensor implementations, the LoD_ζ are either zero or they follow the same trends and lie within the same order of magnitude, such that they can be quantified by a simple multiplier [see discussion of Fig. 6(b) below]. The five plots in Fig. 6(a) allow us to quickly estimate the LoD contributions LoD_ζ of the various noise sources and to formulate requirements for individual sensor system components if a certain target LoD has to be achieved. Dotted magenta lines and crosses indicate noise-source parameters and the corresponding LoD_ζ found in typical integrated sensors and serve as reference for a specific case study [see discussion of Fig. 6(c) below].

In Column 1 of Fig. 6(a), the LoD impact of temperature fluctuations between sensor and reference structures is plotted for two different TOCs, $\mathrm{TOC} = 10^{-4}\,\mathrm{K}^{-1}$ [60,61] and $\mathrm{TOC} = 10^{-5}\,\mathrm{K}^{-1}$, which are typical magnitudes for silicon and silicon nitride waveguides, respectively. Note that the TOC is not just the TOC of the core material but refers to the effective TOC of the overall waveguide, i.e., the ratio of an effective-index change and the associated temperature change. The corresponding LoD contribution scales as $\mathrm{LoD}_\vartheta \propto \mathrm{TOC} \times \sigma_{\vartheta_\mathrm{n}}$. Columns 2 and 3 of Fig. 6(a) show the LoD contribution of the laser frequency and intensity noise, which scale as $\mathrm{LoD}_\omega \propto \sigma_{\omega_\mathrm{n}}/\omega$ and $\mathrm{LoD}_{P_\mathrm{i}} \propto \sigma_{P_\mathrm{i,n}}/P_\mathrm{i} \approx \sqrt{\mathrm{RIN}\Delta f}$, respectively. The combined impact of PD shot noise and various levels of PD NEP are plotted in Column 4 of Fig. 6(a) as a function of the effective input power P_i. Note that the effective optical input power P_i does not directly correspond to the power of the underlying laser diode but additionally accounts for all optical excess losses that result from non-idealities of the various sensor components such as coupling losses in chip-chip interfaces or propagation losses in on-chip transport waveguides [see Subsection 3.2 and Eq. (2)]. The device is either shot-noise-limited for large P_i or small NEP with a $\mathrm{LoD}_{I_\mathrm{s}} \propto \sqrt{\Delta f / P_\mathrm{i}}$, or it is NEP-limited for small P_i or large NEP with a $\mathrm{LoD}_\mathrm{NEP} \propto \sqrt{\Delta f}/P_\mathrm{i}$. The critical input power P_i that marks the crossover between the shot-noise-limited and NEP-limited regime depends on the NEP level. In most sensor realizations, either one or the other can be neglected. Column 5 of Fig. 6(a) shows the LoD contribution of quantization noise as a function of the number of ADC bits N, which scales with $\mathrm{LoD}_{I_\mathrm{q}} \propto 2^{-N}$.

LoD comparison of the different sensor implementations. In Fig. 6(a), we have analyzed the LoD contributions for the $\mathrm{RR}_\mathrm{AP}^\mathrm{CC}$ reference sensor implementation. Figure 6(b) shows how the various other sensor types perform in relation to this reference. The relative impact of the various noise sources is described by colored bars, where a bar length of 1 corresponds to the LoD of the $\mathrm{RR}_\mathrm{AP}^\mathrm{CC}$ reference, and where a missing bar indicates that this sensor implementation is not prone to this specific noise source. As an example, the identical bar lengths in Column 1 of Fig. 6(b) indicate that the relative temperature differences between sensor and reference structures have the same impact on all sensor implementations. This is a consequence of the fact that

temperature-induced fluctuations of the effective-index difference between the sensor and reference structure cannot be separated from the sensor signal itself, irrespective of the underlying sensor implementation. Column 2 of Fig. 6(b) compares the impairments with respect to laser frequency noise. Here, we observe a distinct advantage of the MZI-based sensor implementations compared to their RR-based counterparts. In MZI, the group delay of the two arms can be matched such that the optical phase at the output of the arms is always perfectly correlated, since the corresponding signals were emitted by the same light source at the same instant of time. When bringing these signals to interference, any phase or frequency noise of the light source cancels. Note that this phenomenon is independent of the absolute group delay in each arm. It is, hence, possible to simultaneously maximize the optoelectronic effective-index sensitivity $S_{\mathrm{e},\tau}$ by selecting the optimum sensor arm length $L_{\mathrm{opt}} = 1/\alpha$, and mitigating the effects of laser frequency fluctuations by adapting the group delay of the reference arm to that of the measurement arm. For all MZI-based sensors, LoD_ω is, hence, zero [see the lower part of Column 5 of Fig. 6(b)]. This decoupling of optoelectronic effective-index sensitivity $S_{\mathrm{e},\tau}$ and sensitivity toward frequency noise is not possible in RRs, which rely on interference of portions of incoming light with portions of light of previous round trips, all of which were emitted by the light source at different instants of time and, hence, feature uncorrelated phases. Tailoring the optoelectronic effective-index sensitivity $S_{\mathrm{e},\tau}$ by appropriate choice of the round trip length, thus, unavoidably affects the impact of frequency noise. As consequence, the LoD_ω increases in proportion to the optoelectronic effective-index sensitivity $S_{\mathrm{e},\tau}$. This effect is independent of the detection scheme and the Q-factor of the coupled cavity, i.e., all RR-based sensor implementations are equally impaired by laser frequency noise [see the upper part of Column 5 of Fig. 6(b)]. Note that, while the sensitivity of a RR-based sensor implementation can always be increased by a higher Q-factor, the LoD is eventually limited by the frequency noise of the laser source. Increasing the resonator Q-factor, hence, becomes ineffective once LoD_ω dominates the overall LoD. The comparison of the sensor implementations with respect to laser RIN is shown in Column 3 of Fig. 6(b). It turns out that sensors that use multiple output ports and, thus, measure power differences rather than absolute levels can mitigate the impact of RIN if the operating point is chosen correctly. Furthermore, we find that the $\mathrm{RR}_{\mathrm{AP}}$ implementations outperform their respective $\mathrm{RR}_{\mathrm{AD}}$ counterparts, mainly due to the higher optoelectronic effective-index sensitivity. For the PD noise sources shown in Column 4 of Fig. 6(b), relative impairments for the two extreme scenarios, i.e., the shot-noise-limited regime as well the NEP-limited regime, are shown by a pair of narrower bars for each sensor type. The relative impairments attributed to these two cases of PD noise differ slightly for the sensor implementations, e.g., due to the different implementation-dependent sensitivities, the different number of PDs, and the different average power levels on each PD. Due to its superior sensitivity, the $\mathrm{RR}_{\mathrm{AP}}$ again features a comparatively low LoD contribution. The effect of quantization noise on the sensor implementations is shown in Column 5 of Fig. 6(b) and is almost identical for all sensor implementations. The slight differences here are caused again by the implementation-dependent sensitivity differences, combined with a scaled ADC range that matches the implementation-specific maximum output current $I_{\mathrm{o,max}} = P_{\mathrm{i}} \Re \hat{T}$ of each detector, where $\hat{T}$ is the optical output contrast of each individual output port, which can be calculated from Eqs. (10) and (12) (see, for example, Table 5 in Appendix B for RRs).

Identification of typical LoD limitations. In order to identify the noise source that dominates the total LoD, we indicate in Fig. 6(c) the magnitude of the individual LoD_ζ for typical noise parameters. These noise parameters and their impact on the

various LoD_ζ of the $\mathrm{RR}_{\mathrm{AP}}^{\mathrm{CC}}$ are indicated by dashed magenta lines in Fig. 6(a). The colors in Fig. 6(c) indicate the order of magnitude of the respective LoD contribution.

It can be seen in Column 1 of Fig. 6(c) that fluctuations of the temperature difference between sensor and reference structures may have substantial impact on the LoD, both for MZIs and RRs. The displayed $\mathrm{LoD}_\vartheta \approx 3 \times 10^{-6}$ is obtained for $\sigma_{\vartheta_\mathrm{n}} = 10\,\mathrm{mK}$, which assumes a typical distance between sensor and reference structures of 100 μm along with random temperature gradients with a standard deviation of the order of 1 K/cm and TOC of the order of $10^{-4}\,\mathrm{K}^{-1}$, roughly corresponding to the TOC of a silicon waveguide [60]. The detrimental effects of temperature differences between on-chip sensor and reference structures can be mitigated by different measures. First, sensor and reference structures should be positioned as close to each other as possible, for example, by designing the MZI arms as interleaved spiral waveguides [62] or by using similar techniques for nesting RRs with non-circular shapes. Second, the exposure of the sensing and reference structures to potential temperature changes should be matched. For example, a microfluidic channel that might transport a fluid with a different temperature as the PIC itself, and that is flowing over the sensitive waveguide area, should also flow over the reference waveguide area, and the reference waveguide should not be shielded from these temperature effects by isolating claddings. Third, the geometry and/or materials of the sensor and reference waveguides can be adjusted to lower the effective TOC [63,64].

The effect of laser frequency fluctuations as the second noise source that directly affects the phase shift in the sensor waveguide is shown in Column 2 of Fig. 6(c). We find that frequency fluctuations cause a large $\mathrm{LoD}_\omega \approx 10^{-5}$ in RR-based sensor implementations. For our estimation, we assume a typical value of $\sigma_{\omega_\mathrm{n}}/\omega \cong 10^{-6}$, which roughly corresponds to a laser operating at 1.55 μm with a long-term standard deviation of the emission frequency of $\sigma_{\omega_\mathrm{n}} = 2\pi \times 100\,\mathrm{MHz}$ (see Appendix F). Note that these rather large fluctuations are usually dominated by the low-frequency part of the laser's frequency noise spectrum and may, hence, be much larger than its intrinsic linewidth, which is given by the spectrally white component of the frequency noise spectrum (see Subsection 4.3a and Appendix E for details). As mentioned above, the impact of laser frequency noise on MZI-based sensor implementations can be mitigated completely by matching the group delays of the two interferometer arms, which allows us to decouple the effective-index sensitivity from the sensitivity toward frequency fluctuations. For the typical noise levels considered in our analysis, laser frequency fluctuations are the most prominent limitation for the LoD of RR-based sensor implementations, emphasizing the importance of stable laser drive currents and temperature control. It might additionally be necessary to include a frequency stabilization mechanism that can at least compensate for the slow frequency drift. However, implementing such a mechanism into a highly integrated sensor system requires additional technical effort and might represent a challenge for low-cost solutions.

Columns 4 and 5 of Fig. 6(c) indicate that the intensity noise of typical lasers and the typical PD noise levels only play a minor role for the chosen example of an integrated photonic sensor with $\alpha/k_0 = 5 \times 10^{-5}$. This is mainly due to the fact that the respective LoD scale with the square root of the acquisition bandwidth, and typical acquisition bandwidths are rather small in sensing applications as compared to those used in telecommunication applications. In our example, we use a laser with a rather large RIN of $-120\,\mathrm{dB/Hz}$ and an acquisition bandwidth of $\Delta f = 100\,\mathrm{Hz}$, which corresponds to $\sigma_{P_{\mathrm{i,n}}}/P_\mathrm{i} = \sqrt{\mathrm{RIN}\Delta f} \cong 10^{-5}$ and an associated low $\mathrm{LoD}_{P_\mathrm{i}} \approx 10^{-9}$. At the same acquisition bandwidth, a typical PD with $\mathrm{NEP} = 10^{-12}\,\mathrm{W}/\sqrt{\mathrm{Hz}}$ that receives roughly 1 μW (−30 dBm) of optical power would still allow the system to achieve

a low $\sqrt{\mathrm{LoD}_{I_{\mathrm{NEP}}}^2 + \mathrm{LoD}_{I_{\mathrm{S}}}^2} \approx 10^{-8}$. When it comes to the selection of an appropriate ADC, the required analog operating range plays a crucial role. In our calculations, we assume that the ADC has to be capable of covering the whole output contrast range of the sensor to allow for reliably tuning to the desired operating point. If the fabrication tolerances allow the setting of the operating point reliably by design and if tuning is always possible, the analog operating range of the ADC can be reduced, and the impact of quantization noise on the LoD can be reduced further. In our example shown in Column 5 of Fig. 6(c), a 12-bit ADC that covers the whole output current range leads roughly to $\mathrm{LoD}_{I_{\mathrm{q}}} \approx 3 \times 10^{-8}$.

5. EXPERIMENTAL VALIDATION OF THE IMPACT OF LASER FREQUENCY NOISE

In Section 4, we identified laser frequency noise as the dominant LoD contribution of typical RR-based sensor implementations using non-ideal light sources. This aspect and the associated quantitative model are verified experimentally in this section. To this end, we use the measurement setup depicted in Fig. 7(a). We use an external laser (LAS) at a wavelength of around 1.54 μm to drive an UC add-drop RR sensor ($\mathrm{RR_{AD}}$), realized as a silicon PIC. To investigate the influence of laser frequency noise, we first perform the experiment with a benchtop-type, highly stable TLS. We then compare the results obtained with the TLS to those obtained with a pigtailed VCSEL as an example for a particularly simple light source type that may be used in low-cost integrated sensors. In both cases, the lasers and the PIC are temperature-stabilized to remove the impact of thermal drift. Light is coupled to and from the PIC via optical fibers and an on-chip GCs. At the output of the PIC, light is send to an external PD. We use an oscilloscope (OSC) to record and digitize the resulting photocurrent and store it for offline analysis of the signal and the noise contributions. Note that an erbium-doped fiber amplifier [EDFA, not shown in Fig. 7(a)] was used after the sensor PIC to compensate for the rather high GC losses and to ensure a sufficiently high power level at the input of the high-speed photodiode (Finisar XPDV120R) that was used in this experiment. We verified that the EDFA, which was followed by a bandpass filter with a 2 nm passband to suppress amplified spontaneous emission (ASE) noise, did not have any impact on the investigation toward frequency noise sensitivity of this sensor.

In our experiments, we first capture the light at the drop port of the add-drop RR and measure the associated photocurrent for different operating point offsets $\Delta\varphi_{\mathrm{OP,RR}}$ in the vicinity of a ring resonance at $\varphi_{\mathrm{res}} = 2\pi m (m \in \mathbb{N})$ by adjusting the laser frequency. In the case of the VCSEL, the emission frequency was tuned via the injection current. In each operating point, we record the time-dependent output current and extract the mean photocurrent I_{q}, shown as the blue crosses in Figs. 7(b) and 7(c), as well as its standard deviation $\sigma_{I_{\mathrm{q}}}$, shown as red crosses in Figs. 7(b) and 7(c). In our measurements, we use an acquisition bandwidth of $\Delta f = 500$ kHz and an observation time of $T_{\mathrm{obs}} \approx 1$ ms. We verified that, for the investigated operating points, the ASE of the EDFA did not impact the photocurrent noise to a relevant degree. We then fit a Lorentzian resonance model of an $\mathrm{RR_{AD}}$, as shown in Table 6 in Appendix C, to the measured mean photocurrents I_{q}, as shown in the solid blue line in Figs. 7(b) and 7(c). In these fits, we use the peak transmission, the Q-factor, and the resonance frequency ω_{res} as fit parameters, while the effective group RI n_{eg} is obtained from an independent transmission measurement of the resonator. Both the mean photocurrent I_{q} and its standard deviation $\sigma_{I_{\mathrm{q}}}$ are normalized to the maximum current measured in resonance, which is given by $\hat{I}_{\mathrm{q}} = P_{\mathrm{i}}\hat{\tau}$, where P_{i} denotes the effective optical input power and where $\hat{\tau}$ refers to the optoelectronic transmission on resonance.

In a next step, we analyze the operating-point-dependent current deviations, where significant differences between the VCSEL and the TLS-based measurement can be seen. The most prominent difference is that in the case of the VCSEL-based

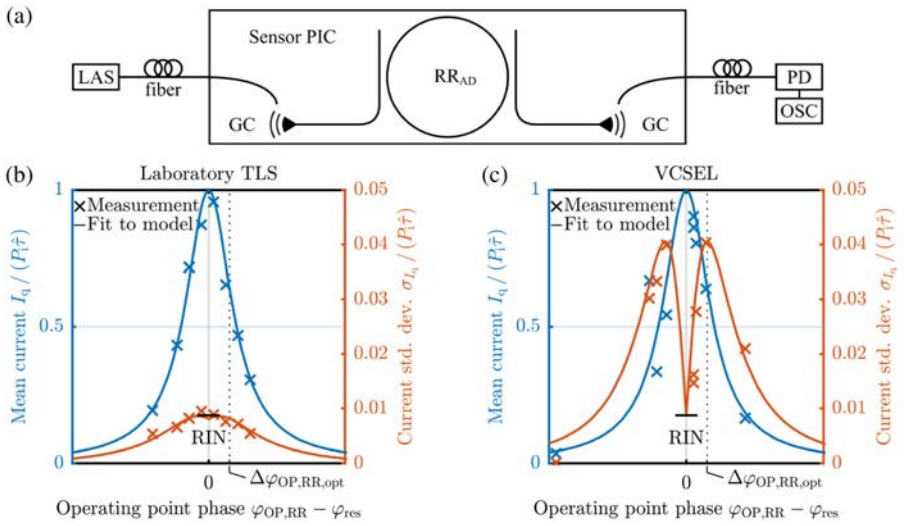

Experimental validation of the model for laser frequency noise and relative intensity noise (RIN). (a) Measurement setup consisting of a tunable laser (LAS), a sensor PIC containing an under-coupled add-drop ring resonator (RR_{AD}), an external photodetector (PD), and an oscilloscope (OSC). The optical connections from and to the silicon PIC are realized with optical fibers and grating couplers (GC) designed for 1550 nm. The overall insertion loss of the PIC amounts to 15.5 dB, including fiber-chip coupling losses of 6 dB per GC. An erbium-doped fiber amplifier (EDFA, not shown) is used after the sensor PIC to compensate for these losses and to ensure a sufficiently high power level at the input of the high-speed PD (Finisar XPDV120R) (b), (c) Normalized mean output current $I_q/(P_i\hat{\tau})$ (left axes, blue) and normalized output-current standard deviation $\sigma_{I_q}/(P_i\hat{\tau})$ (right axes, red) of the RR_{AD}^{UC} drop port, shown at different operating point offsets $\Delta\varphi_{OP,RR}$ in the vicinity of a resonance at $\varphi_{res} = 2\pi\ m$. The experiment is performed twice—(b) once with a TLS and (c) once with a VCSEL, which differ with respect to their frequency stability. The crosses denote measured data points, which were obtained by recording the output currents, whereas the solid blue lines are Lorentzian resonance fits and the solid red lines are fits to the transmission and noise propagation models derived in Section 4. The optimum operating point $\Delta\varphi_{OP,RR,opt}$ of highest optoelectronic effective-index sensitivity is marked with dotted lines. For operation with a TLS, the output current noise follows the optoelectronic transmission τ. In contrast to this, the output current noise of the VCSEL-operated RR_{AD}^{UC} follows the shape of the optoelectronic effective-index sensitivity $|S_{e,\tau}|$. This indicates that, in the given measurement setup, the TLS-driven sensor is mainly impaired by relative intensity noise (RIN) of the optical power coupled to the device. Note that, for our experiment, this RIN is not dominated by the laser source but by temporal fluctuations of the power coupling efficiency at the PIC input, which amounts to approximately 1% in both experiments. In contrast to this, laser frequency fluctuations are found to be the dominant noise source for the VCSEL-driven sensor. The frequency fluctuations extracted from these experiments amount to 435 MHz for the VCSEL and to 10 MHz for the TLS and are in fair agreement with independent measurements of the frequency noise characteristics (see Appendix E).

experiment, the current noise is much larger and follows the characteristic shape of the optoelectronic effective-index sensitivity $|S_{\mathrm{e},\tau}|$, which corresponds to the magnitude of the slope of the frequency-dependent optical transmission [see Fig. 3(c)]. In contrast to that, the current noise measured in the TLS-based experiment rather seems to follow the shape of the optoelectronic transmission τ [see Fig. 3(b)]. Note that in both cases, the current deviation strongly depends on the operating point, and we may, hence, assume that the PD NEP as well as quantization noise can be neglected—both effects would lead to a constant noise background, which is independent of the operating point. Moreover, we neglect shot noise, which is irrelevant at the power levels of typically $P_{\mathrm{i}} = 1\ \mu\mathrm{W}$ measured in our experiment, and we exclude sensor thermal noise due to the temperature stabilization of the sensor PIC. The only remaining noise sources are, hence, intensity noise of the optical signal coupled to the PIC and laser frequency noise. According to Fig. 5 and Table 4, in the case of an $\mathrm{RR}_{\mathrm{AD}}$, only intensity noise at the sensor input is translated to the output current via the optoelectronic transmission $\tau = \Re T$, while frequency noise is translated to the output current via $|S_{\mathrm{e},\tau}| = \Re|S_{\mathrm{e}}|$. The output current deviations can, hence, be modeled by the square root of the sum of the respective variances,

$$\sigma_{I_{\mathrm{q}}} \approx \sqrt{(\tau\sigma_{P_{\mathrm{i,n}}})^2 + \left(\frac{n_{\mathrm{eg}} P_{\mathrm{i}}}{\omega}|S_{\mathrm{e},\tau}|\sigma_{\omega_{\mathrm{n}}}\right)^2};$$

$$\frac{\sigma_{I_{\mathrm{q}}}}{P_{\mathrm{i}}\hat{\tau}} \approx \frac{1}{\hat{\tau}}\sqrt{\left(\tau\sqrt{\mathrm{RIN}\Delta f}\right)^2 + \left(\frac{n_{\mathrm{eg}}}{\omega}|S_{\mathrm{e},\tau}|\sigma_{\omega_{\mathrm{n}}}\right)^2}. \tag{23}$$

For fitting the measured operating-point-dependent current deviations $\sigma_{I_{\mathrm{q}}}$ to Eq. (23), we reuse the values of the optoelectronic transmission τ and its peak $\hat{\tau}$, the corresponding Q-factor, the optoelectronic effective-index sensitivity $S_{\mathrm{e},\tau}$, the resonance frequency ω_{res}, and the effective group RI n_{eg}, which are obtained from the fit of the measured mean photocurrents I_{q}, as well as from the independent transmission measurement, and only vary the relative-intensity-noise level RIN and the laser frequency deviations σ_ω as free parameters. For the TLS experiment [see solid red line in Fig. 7(b)], we find a rather small TLS frequency fluctuation of $\sigma_{\omega_{\mathrm{n}}} = 2\pi \times 10\ \mathrm{MHz}$, which is in fair agreement with the directly measured value of $\sigma_{\omega_{\mathrm{n}}} = 2\pi \times 23\ \mathrm{MHz}$ (see Appendix E). The output current noise is, hence, dominated by RIN. Using an acquisition bandwidth of $\Delta f = 500\ \mathrm{kHz}$, we find a RIN level of $\mathrm{RIN} = 2 \times 10^{-10}\ \mathrm{Hz}^{-1}$ $(-97\ \mathrm{dB\,Hz}^{-1})$ for the optical power coupled to the PIC, which equals $\sigma_{P_{\mathrm{i,n}}}/P_{\mathrm{i}} = \sqrt{\mathrm{RIN}\Delta f} = 1\%$. This value is clearly higher than the typical RIN levels expected from benchtop-type TLS, and we, therefore, attribute the optical power fluctuations to the measurement setup, in particular to mechanical vibrations affecting the coupling from the fibers to the PIC. This is confirmed by repeating the coupling experiments with different lasers and by observing that the RIN level of the optical signal at the PIC output does not depend on the laser source. In the VCSEL-based experiment, we fit the same noise model of Eq. (23) based on Table 4 to the measured current deviations [see the solid red line in Fig. 7(c)]. We use the same RIN level of $2 \times 10^{-10}\ \mathrm{Hz}^{-1}$ $(-97\ \mathrm{dB\,Hz}^{-1})$ as in the TLS experiment, which leaves only the laser frequency fluctuation σ_ω as a free parameter. An optimum fit is obtained for of $\sigma_{\omega_{\mathrm{n}}} = 2\pi \times 435\ \mathrm{MHz}$, which is again in fair agreement with the directly measured value of $\sigma_{\omega_{\mathrm{n}}} = 2\pi \times 175\ \mathrm{MHz}$ (see Appendix E). Note that even though the optimum operating point $\Delta\varphi_{\mathrm{OP,RR,opt}}$ exhibits the highest current noise, it does not yield the worst LoD: since both the current fluctuations caused by laser frequency noise and the sensitivity increase in proportion to $|S_{\mathrm{e},\tau}|$, the LoD is independent on the operating point as long as laser frequency noise is the dominant impairment.

6. GUIDELINES FOR SENSOR DESIGN

Based on the sensitivity and noise analysis detailed in the preceding sections, we formulate guidelines for designing integrated phase-sensitive photonic sensor systems that combine high sensitivity and low LoD with manageable technical complexity. All guidelines are summarized in a practical example of a favorable sensor design that relies on readily available optic and electronic components.

6.1. Sensitivity

The effective-index sensitivity $S_\mathrm{e} = \partial/\partial n_\mathrm{e}(T) = \partial/\partial n_\mathrm{e}(P_\mathrm{o}/P_\mathrm{i})$ of all discussed sensor implementations is proportional to k_0/α (see Table 3) and can, hence, be increased by operation at high wavenumbers $k_0 = \omega/c$ and by decreasing the modal power loss coefficient α. In contrast to this, the optoelectronic effective-index sensitivity $S_{\mathrm{e},\tau} = \Re S_\mathrm{e}$ can generally not be increased by using shorter larger wavenumbers $k_0 = \omega/c$ since, for a given quantum efficiency of the PD, the electric readout responsivity $\Re$ is inversely proportional to the photon energy and, hence, to the vacuum wavenumber (see Subsection 4.2e). Still, for sensing of analytes in aqueous solutions, short wavelengths in the visible range offer the advantage that absorption loss occurring in the evanescent portion of the guided field is less of a problem than for near-infrared (NIR) wavelengths. When it comes to blood analysis, photonic sensors largely rely on the so-called therapeutic window between 600 nm and 1100 nm, which offers a good compromise between pronounced hemoglobin absorption at shorter wavelengths and strong water absorption at longer wavelengths [65]. Once the wavelength is fixed, the appropriate implementation of the sensor concept should be chosen. Among the various sensor implementations discussed in this paper, simple all-pass RRs with a single bus waveguide in a slightly UC operation ($\mathrm{RR}_\mathrm{AP}^\mathrm{UC}$) exhibit the highest sensitivity (see Fig. 4) but may be prone to laser frequency noise (see also subsequent paragraph). In contrast to this, rather simple MZIs provide comparable sensitivity if their arm length is adapted to the modal loss, i.e., $L = 1/\alpha$ (see Fig. 4), and does not suffer from laser frequency noise. This comes at the cost of an increased footprint, which can be reduced by using interleaved spirals in the interferometer arms, thereby also minimizing temperature differences between the sensor and the reference arms. Note that, in practical implementations of sensor systems, the package size and cost are usually not dominated by the sensor waveguide structures themselves but rather by peripheral components such as electronic readout circuits and by the assembly processes. The footprint of MZI-based sensor structures should, hence, not play an important role unless massively parallel sensor arrays are required.

6.2. Limit of Detection

The LoD offered by integrated sensor systems that are built from standard components and that are subject to typical environmental conditions is dominated by the two noise sources that directly induce a phase shift in the sensor waveguide: on-chip temperature fluctuations and laser frequency noise. Stochastic on-chip temperature differences between sensor and reference waveguides lead to impairments in RRs and MZIs alike. These impairments can be reduced by proper waveguide design and routing, sensor layout, and temperature control. Laser frequency noise is mainly a problem for RRs and can be mitigated completely in MZIs by design. In fact, for RR-based sensor implementations operated by a light source with a given linewidth, there is an upper limit of the Q-factor, beyond which the LoD will not improve further with higher Q. MZIs, hence, allow us to build high-sensitivity sensors with low-cost light sources and without complex frequency stabilization schemes. Compared to on-chip temperature fluctuations and laser frequency noise, the impact of noise sources that directly affect the signal level at the sensor output is usually less problematic

[see Fig. 6(a)]. This applies, e.g., to laser RIN, to PD shot noise, and to additional PD noise quantified by the NEP, as well as to quantization noise. Note that the LoD contribution of these four noise sources is automatically reduced by the optoelectronic effective-index sensitivity (see Subsection 4.3b). The LoD contribution of the PD shot noise, the additional PD noise quantified by the NEP, and the quantization noise sources are reduced by increasing the effective input power P_i.

6.3. Readout

We find that balanced-detection schemes allow us to eliminate the impact of RIN on the LoD [see Fig. 6(b)] and to simplify the feedback control that stabilizes the operating point, both for MZI- and RR-based sensor implementations. For MZIs, balanced detection additionally allows us to exploit the full optical power that is available at the device output and, therefore, doubles the sensitivity compared to single-output implementation [see Fig. 4(d)]. In contrast to that, balanced detection in RR-based sensor implementations necessarily requires a second output port, which reduces the Q-factor of the ring. This has a detrimental effect on the sensitivity, which is only partially compensated for by the fact that the full output power is used [see Fig. 4(d)]. Regarding MZIs, using a triple-output configuration does not increase the sensitivity compared to its dual-output counterpart [Fig. 4(d)]. However, in combination with a detection scheme based on a Clarke transformation, triple-output MZIs allow us to directly extract the phase difference of the two interferometer arms independently of the operating point and, thereby, eliminate the need for operating-point stabilization, thus vastly reducing the system complexity. Regarding the LoD contribution of the PDs, the triple-output MZI provides the same performance as its double-output counterpart provided that all detectors are operated at the shot-noise limit [Fig. 6(b)]. For NEP-limited operation, the PD-related LoD contribution of the triple-output MZI is increased by a factor of $\sqrt{3}$ relative to the double-output scheme due to the noise in the additional detector. Note that using an optical hybrid with four detectors at the MZI output does not bring any additional benefit but further increases the complexity of the sensor PIC. Specifically, a quadruple-output MZI provides the same overall performance as a triple-output device in case of shot-noise limited operation and increases the PD-related LoD contribution by an additional factor of $\sqrt{4/3}$ for NEP-limited operation. We, hence, identify a triple-output MZI as an ideal trade-off between the complexity of the optical chip, the complexity of the electronic control and readout circuits, and the LoD performance.

6.4. Favorable Sensor Implementation

With these findings, we now propose a favorable sensor design that combines a triple-output MZI with readily available optical and electronic components. The system is illustrated in Fig. 8(a). We consider a laser operating in the visible regime at 600 nm (green box) and an effective input power P_i including all coupling losses of 10 μW, which can be easily achieved with low-cost VCSEL and state-of-the-art optical coupling approaches. The laser has a RIN of $-120\,\mathrm{dB/Hz}$ and a frequency noise standard deviation of $\sigma_{\omega_\mathrm{n}} = 2\pi \times 20\,\mathrm{MHz}$. The waveguides are based on silicon nitride and exhibit a low propagation loss of 3 dB/cm along with a TOC of approximately $10^{-5}\,\mathrm{K}^{-1}$. The MZI arms are length-optimized, $L = 1/\alpha \approx 15\,\mathrm{mm}$, and matched with respect to the optical group delay such that the frequency noise of the laser does not play a role. The waveguides are routed as two interleaving spirals, marked in blue/yellow in Fig. 8, which ensures small temperature differences between the arms. For a waveguide spacing of 5 μm and an on-chip temperature gradient of 1 K/cm, we estimate typical values of $\sigma_{\vartheta_\mathrm{n}} = 0.5\,\mathrm{mK}$ for the mean temperature

differences between the reference and the measurement arm. The sensor PIC footprint fits into an on-chip area of $400 \times 400\ \mu m^2$. The three PDs, illustrated as red boxes, have a responsivity of 0.4 A/W and a NEP of $10^{-10}\ W/\sqrt{Hz}$. The corresponding output currents are digitized with 10-bit ADC at an acquisition bandwidth of 100 Hz, and the phase shifts can be extracted by a Clarke transformation (see Table 2) which is performed in an ASIC shown below the PIC. With these assumptions, which are summarized on the right-hand side of Fig. 8(b), the sensor can achieve a $LoD = 10^{-6}$ for the effective-index fluctuations. This LoD is dictated by the NEP of the PDs, which leaves room for further improvement. We also provide a MATLAB application Code 1, Ref. [66] that allows us to estimate the performance for other sensor concepts and device specifications.

7. FURTHER DESIGN ASPECTS: WAVEGUIDE DESIGN, ASSEMBLY, AND ANALYTE HANDLING

Besides the system-level design aspects explained in the previous sections, successful implementation of an integrated photonic sensor device requires consideration of additional aspects. This includes, e.g., the design of the underlying waveguides for maximum sensitivity S_{env} with respect to environmental parameters, photonic system assembly concepts that allow us to efficiently complement the sensor PIC with light sources and detectors, and schemes for handling of liquid or gaseous analytes relying, e.g., based on co-integration of microfluidic systems. In the following sections, we provide a brief overview of these aspects that have been intensely discussed in the literature over the previous years.

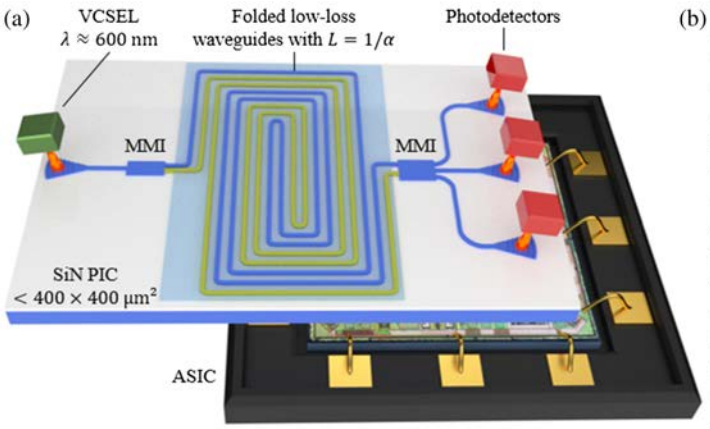

(b)

k_0	$10^7\ m^{-1}$
P_i	10^{-5} W
RIN	−120 dB/Hz
σ_{ω_n}	$2\pi \times 20$ MHz
α	3 dB/cm
L	15 mm
TOC	$10^{-5}\ K^{-1}$
σ_{ϑ_n}	0.5 mK
$\Re$	0.4 A/W
NEP	$10^{-10}\ W/\sqrt{Hz}$
N	10 bit
Δf	100 Hz
$S_{e,\tau}$	$> 3 \times 10^5$ A
LoD	$< 2 \times 10^{-7}$
Size	$< 1\ mm^2$

Analysis of a favorable implementation of a highly integrated photonic sensor, based on readily available optical and electronic components. (a) Graphical illustration of the sensor concept, relying on a SiN-based triple-output MZI (MZI3) with optimally balanced arms that are folded into each other, fed by a power-efficient low-cost VCSEL at a wavelength of 600 nm. The scheme is insensitive to laser frequency and intensity noise and minimizes the impact of temperature fluctuations, does not require any operating-point stabilization or tuning, and, thus, lends itself to highly scalable, technically robust sensor systems. (b) Specifications of the various sensor components used for the performance estimation. Other sensor concepts and device specifications can be analyzed by a MATLAB application that is based on the model described in this paper and that can be accessed in [66].

7.1. Waveguide Design and Surface Functionalization

Optimization of integrated waveguides with respect to the waveguide sensitivity S_{env} [see Eq. (3)] is an important subject in its own right. In general, the waveguide sensitivity S_{env} can be maximized by proper choice of waveguide type, material, and geometry, thereby enhancing the interaction of the guided optical mode with the medium that is subject to the change Δ_{env} of the environmental parameter of interest. In most cases, this parameter is either the RI of a homogeneous medium that surrounds the waveguide core or the thickness, possibly in combination with the RI, of a thin layer of analyte molecules that specifically bind to a functionalized surface of the waveguide core. Such surface sensing applications allow for highly multiplexed detection of analytes in massively parallel sensor arrays [26,27] but crucially rely on robust processes that permit us to selectively functionalize individual sensor elements without any degradation of or cross-reaction with differently functionalized sensor areas [67–71].

Waveguides with high sensitivity S_{env} can be realized on different material platforms such as silicon-on-insulator [11–14] or silicon nitride [15–18], where both quasi-TE or quasi-TM waveguide modes are exploited, possibly along with slot waveguide concepts [9] or sub-wavelength grating (SWG) structures [72,73] (see [1,6,37] for an overview). A particularly comprehensive overview of sensor waveguide designs covering different waveguide types, polarizations, and wavelengths can be found in the reviews [1,6]. A detailed discussion of the benefits of slot and SWG waveguides compared to strip waveguides can be found in [37]. Detailed geometrical design guidelines are provided in [36] along with a comparative study of a variety of silicon-on-insulator and silicon-nitride waveguide types that are specifically geared toward detection of target molecules bound to a functionalized waveguide surface.

7.2. Photonic System Assembly and Light-Source Integration

Photonic sensor systems crucially rely on techniques that allow us to efficiently combine sensor PIC, typically made from of indirect-bandgap silicon-on-insulator or silicon-nitride waveguides, with light sources based on direct-bandgap III–V compound semiconductors. Importantly, these techniques should offer a path toward compact and reliable assemblies that are amenable to industrial mass production. One option is to use monolithically co-integrated laser sources, realized, e.g., through heterogeneous integration of III–V epitaxial layers that are transferred to pre-structured silicon-based PIC [74–80] and that are then collectively processed on a wafer level. While this approach stands out due to good scalability, it requires highly developed front-end fabrication processes and is, thus, mainly suited for high-volume applications. Alternatively, readily processed VCSEL or DFB lasers may be transferred to passive PIC by microtransfer printing [81] or by conventional flip-chip bonding [82]. These concepts offer higher flexibility with respect to the underlying light sources and sensor PIC, but often rely on high-precision assembly techniques with limited throughput. When it comes to efficient co-integration on a package level, 3D-printed micro-lenses [83] or so-called photonic wire bonds [84,85] may open a path toward fully automated assembly of compact multi-chip systems with outstanding flexibility and performance. Similarly, options for efficiently implementing PDs on sensor PICs range from monolithic integration of germanium detectors on silicon photonic waveguides [86] to heterogeneous integration of III–V layers [80] and to transfer-printed III–V PDs [87]. The decision of the optimal light-source integration and system assembly concept heavily depends on the desired applications and in particular on the expected production volumes.

7.3. Analyte Handling and Microfluidics

Besides the optoelectronic system concept and the associated technological implementation, the delivery of the gaseous or liquid analytes to the sensing area is a key aspect in case of chemical sensors. In many cases, this calls for efficient co-integration with advanced micro-fluidic systems [88–90]. A comprehensive review of optofluidic integration can be found in [28], which discusses several microfluidic systems that are co-integrated with PIC-based sensors and that rely on the two primarily used materials, namely polydimethylsiloxane (PDMS) and on the negative-tone photoresist SU–8. In general, the PIC can be co-integrated with standalone pre-processed microfluidic chips [91], or the microfluidic structures can be processed on a wafer scale directly on the PIC [92]. In addition, digital microfluidics [93], a platform for manipulation of microdroplets based on the electrowetting effect, can be co-integrated with PICs [94–97]. Digital microfluidic systems allow for a precise spatial and temporal control over microdroplets, offering transporting, mixing, and splitting functions for lab-on-chip applications.

8. SUMMARY

We have developed a holistic model for integrated phase-sensitive photonic sensors that allows us to consistently analyze and to broadly benchmark the performance of different sensor concepts and technical implementations. Our model covers the entire signal chain from the light source through the sensor PIC and the PDs to the ADCs while accounting for the non-idealities of each component. We perform an in-depth performance analysis of different sensor systems with respect to their sensitivity and their limit of detection (LoD), considering in particular the limitations of highly integrated, mass-deployable sensor systems that rely on non-ideal components and that are operated outside a controlled laboratory environment. We examine the potential and the limitations of different sensor implementations based on RRs and MZIs, and we extract globally optimized design parameters and optimum operating points for each implementation. We find that resonator-based sensors are particularly prone to laser frequency noise and validate the underlying theoretical model by experimentally investigating impact of frequency noise on a ring-resonator-based sensor. Based on our analysis, we formulate design guidelines and estimate the achievable performance for different sensor implementations. The key insights are merged into a specific proposal for a particularly attractive sensor design that relies on a triple-output MZI in combination with readily available low-cost light sources and PDs. We further provide a MATLAB-based tool that incorporates the full model developed here that can be readily used to estimate the achievable performance of a specific sensor system based on RRs or MZIs.

APPENDIX A: WAVELENGTH-RELATED BULK SENSITIVITY OF THE RR AND MZI

For refractive-index (RI) sensors, the sensor waveguide is described by the waveguide sensitivity $S_{\mathrm{env}} = \partial n_{\mathrm{e}}/\partial n_{\mathrm{M}}$, corresponding to the ratio of the change Δn_{e} of the effective RI of the waveguide mode and the underlying change $\Delta_{\mathrm{env}} = \Delta n_{\mathrm{M}}$ of the RI of the medium that surrounds the waveguide [see Eq. (3)]. This sensitivity may alternatively be defined [1,6,28,33] via the change of a resonance wavelength λ_{res} of a ring resonator (RR) or the change of a transmission-fringe wavelength λ_{fri} of an MZI with respect to a RI change Δn_{M}. The use of wavelength-related bulk sensitivities is useful, e.g., for sensors that rely on spectral readout concepts, which can be realized

by employing tunable lasers or broadband light sources in combination with spectrometers. In such readout concepts, the wavelengths of spectral characteristics such as λ_{res} or λ_{fri} serve as the measurement quantity, estimated via signal processing from recorded spectra.

Resonances or transmission fringes occur at constant RR round trip phases φ_{RR} according to Eq. (9) or MZI phase differences φ_{MZI} according to Eq. (9), which are usually equal to integer multiples of 2π, i.e., $\varphi_{RR}(\Delta n_e, \lambda_{res}) = 2\pi\, m$ or $\varphi_{MZI}(\Delta n_e, \lambda_{fri}) = 2\pi\, m$. We can, thus, derive the wavelength sensitivities S_λ by calculating the wavelength shifts $\Delta\lambda$ that are needed to compensate a certain effective RI change $\Delta n_e = S_{env}\Delta n_M$,

$$\frac{\partial \varphi_{RR}}{\partial(\Delta n_e)}\Delta n_e + \frac{\partial \varphi_{RR}}{\partial \lambda}\Delta\lambda_{res} = 0\,,$$

$$\frac{\partial \varphi_{MZI}}{\partial(\Delta n_e)}\Delta n_e + \frac{\partial \varphi_{MZI}}{\partial \lambda}\Delta\lambda_{fri} = 0\,. \tag{A1}$$

Inserting Eqs. (9) and (11) in Eq. (A1) leads to the wavelength sensitivities S_λ for the RR and MZI,

$$S_{\lambda,RR} = \frac{\partial \lambda_{res}}{\partial n_M} = \frac{\Delta\lambda_{res}}{\Delta n_e} S_{env} = \frac{\lambda}{n_{eg}} S_{env},$$

$$S_{\lambda,MZI} = \frac{\partial \lambda_{fri}}{\partial n_M} = \frac{\Delta\lambda_{fri}}{\Delta n_e} S_{env} = \frac{\lambda}{n_{eg}} S_{env}\left(\frac{\Delta n_{eg,0}}{n_{eg}} - \frac{\Delta L}{L}\right)^{-1}. \tag{A2}$$

Note that the wavelength sensitivity $S_{\lambda,MZI}$ of MZI can be tuned deliberately by changing the optical path lengths of the interferometer arms and, hence, the group delay. Specifically, for an MZI with perfectly matched group delays in the two arms, $L\Delta n_{eg,0} - \Delta L n_{eg} = 0$, $S_{\lambda,MZI}$ approaches infinity, while the wavelength-dependent interference fringes disappear.

APPENDIX B: OPTICAL POWER TRANSMISSION OF RING RESONATORS

The optical power transmission characteristics of all-pass and add-drop ring resonator (RR) can be expressed by the round trip amplitude transmission factor $a = \exp(-\alpha L/2)$ and the amplitude transmission ρ_1 and ρ_2 of the coupling zones, as well as the round trip phase shift $\varphi_{RR} = -k_0 L \Delta n_e + \varphi_{OP,RR}$, as shown in Fig. 2(a) and Eq. (9). In these relations, α is the modal power loss coefficient, L is the round trip length, $k_0 = \omega/c$ denotes the vacuum propagation constant of light at angular frequency ω, and n_e is the modal effective refractive index of the waveguide mode in the sensitive region. The mathematical expressions for the various power transmission characteristics are shown in Column 2 of Table 5, and details on the derivation can be found in the literature, see, e.g., [33]. The label "AP" in Column 1 of Table 5 denotes the single-output port ("through port") of an all-pass RR, while "ADT" and "ADD" refer to the through port and the drop port of an add-drop RR, respectively. In addition, we specify the minimum and the maximum of the frequency-dependent optical power transfer function, T_{min} and T_{max}, as well as an approximation for the corresponding optical output contrast $\hat{T} = T_{max} - T_{min}$ and the Q-factor (see Columns 3–6 of Table 5).

APPENDIX C: DETAILS ON THE SIMPLIFIED RING RESONATOR SENSOR MODEL

The sensitivity optimization in Subsection 4.2 is performed by finding the operating point in which a change Δn_e of the effective refractive index and the associated change $\Delta\varphi_{RR}$ of the ring resonator (RR) round trip phase shift leads to a maximum change ΔT of the optical power transmission. This operating point can be found by identifying the extrema of the derivative of the relations in Column 2 of Table 5 with respect to φ_{RR}. For simplicity, we assume high-finesse RR and approximate the original transmission equations for the various output ports in Column 2 of Table 5 by Lorentzian functions T_{Lor} in the vicinity of the resonances given by $\varphi_{res} = 2\pi m (m \in \mathbb{N})$,

$$T(\varphi_{RR}) \approx \begin{cases} 1 - T_{Lor}(\Delta\varphi_{RR}) & \text{for AP} \\ T_{Lor}(\Delta\varphi_{RR}) & \text{for ADT and ADD} \end{cases}, \quad \Delta\varphi_{RR} = \varphi_{RR} - \varphi_{res} \ll 1, \tag{C1}$$

where the Lorentzian function is given by

$$T_{Lor}(\Delta\varphi_{RR}) = \hat{T}\frac{1}{1 + \left(\frac{2\Delta\varphi_{RR}}{\alpha L / c_Q}\right)^2}. \tag{C2}$$

The Lorentzian approximation is obtained by using the relation $\cos(\varphi_{RR}) \approx 1 - (\varphi_{RR} - \varphi_{res})^2/2 = 1 - \Delta\varphi_{RR}^2/2$ for $\Delta\varphi_{RR} = \varphi_{RR} - \varphi_{res} \ll 1$ in the equations given in Column 2 of Table 5. With these approximations, the resonance depth and the resonance width remain as the only two parameters, which are both easily obtained experimentally—in contrast to the coupling and loss parameters ρ_1, ρ_2, and a. Specifically, the resonance depth can be analytically described by the optical output contrast $\hat{T}$, and the full width at half-maximum (FWHM) of the resonance can be calculated from the Q-factor (see Column 6 of Table 5 and Column 3 of Table 6). Note that the Lorentzian approximation is valid only for high-finesse resonators with $\alpha L \ll 1$ and leads to errors of less than 1% for as long as $a = \exp(-\alpha L/2) > 0.65$. A worst-case attenuation of $\alpha \simeq 1000\,\mathrm{m}^{-1}$ corresponding to water absorption at $\lambda = 1550$ nm in a ring with a radius of 70 μm in a silicon photonic waveguide ($n_e \approx 3$) would still be compatible with this approximation.

The Lorentzian as a function of $\Delta\varphi_{RR} = \varphi_{RR} - \varphi_{res}$ can also be expressed as a function of a frequency offset $\Delta\omega = \omega - \omega_{res}$ or of an effective-refractive-index offset $\Delta n_e = n_e - n_{e,res}$ from the respective value at resonance, as displayed in Rows 3 and 4 of Table 6. For each of these quantities, we can specify a FWHM of the associated Lorentzian resonance (see Column 3 of Table 6). In these relations, $n_{eg} = n_e + \omega\partial n_e/\partial\omega$ is the effective group refractive index at the resonance frequency

Table 5. Generic Optical Power Transmission Characteristics of Ring Resonators[a,b]

	T	T_{min}	T_{max}	$\hat{T}$	Q
AP	$\frac{\rho_1^2 - 2\rho_1 a\cos(\varphi_{RR}) + a^2}{1 - 2\rho_1 a\cos(\varphi_{RR}) + (\rho_1 a)^2}$	$\frac{(a-\rho_1)^2}{(1-\rho_1 a)^2}$	$\frac{a^2+\rho_1{}^2}{1+(\rho_1 a)^2}$	$1 - \frac{(a-\rho_1)^2}{(1-\rho_1 a)^2}$	$\frac{n_{eg}k_0 L}{2}\frac{\sqrt{\rho_1 a}}{1-\rho_1 a}$
ADT	$\frac{\rho_2^2 a^2 - 2\rho_1\rho_2 a\cos(\varphi_{RR}) + \rho_1^2}{1 - 2\rho_1\rho_2 a\cos(\varphi_{RR}) + (\rho_1\rho_2 a)^2}$	$\frac{(\rho_2 a - \rho_1)^2}{(1-\rho_1\rho_2 a)^2}$	$\frac{\rho_2^2 a^2 + \rho_1^2}{1+(\rho_1\rho_2 a)^2}$	$1 - \frac{(\rho_2 a - \rho_1)^2}{(1-\rho_1\rho_2 a)^2}$	$\frac{n_{eg}k_0 L}{2}\frac{\sqrt{\rho_1\rho_2 a}}{1-\rho_1\rho_2 a}$
ADD	$\frac{(1-\rho_1^2)(1-\rho_2^2)a}{1 - 2\rho_1\rho_2 a\cos(\varphi_{RR}) + (\rho_1\rho_2 a)^2}$	$\frac{(1-\rho_1^2)(1-\rho_2^2)a}{1+(\rho_1\rho_2 a)^2}$	$\frac{(1-\rho_1^2)(1-\rho_2^2)a}{(1-\rho_1\rho_2 a)^2}$	$\frac{(1-\rho_1^2)(1-\rho_2^2)a}{(1-\rho_1\rho_2 a)^2}$	

[a]Note that the output contrast $\hat{T} = T_{max} - T_{min}$ in Column 5 was approximated by assuming high-finesse ring resonators, which, for off-resonance operation, leads to negligible power loss for the through ports ($T_{max} \approx 1$) and to negligible power transmission for the drop port of ADD resonators ($T_{min} \approx 0$).

[b]The relations were derived based on the assumption of lossless coupling sections $\kappa_1^2 + \rho_1^2 = \kappa_2^2 + \rho_2^2 = 1$ (see Subsection 4.1a and Fig. 2).

ω_{res} defined by $L n_{\mathrm{e}}(\omega_{\mathrm{res}})\omega_{\mathrm{res}}/c = 2\pi m$ ($m \in \mathbb{N}$). Note that, for $\alpha L \ll 1$, the loaded Q-factor Q can be expressed as the ratio of the resonance frequency and the frequency FWHM [98] and can be linked through a ratio coefficient c_Q to the intrinsic, unloaded Q-factor Q_i,

$$Q = \frac{\omega_{\mathrm{res}}}{\Delta\omega_{\mathrm{FWHM,RR}}} = c_{\mathrm{Q}} \quad Q_{\mathrm{i}} = c_{\mathrm{Q}} \frac{k_0}{\alpha} n_{\mathrm{eg}}. \tag{C3}$$

Note that the relations given in Table 6 are general and can be adapted to the various sensor implementations by using the corresponding Q-factor Q, quality ratio c_Q, and optical output contrast $\hat{T} = \hat{\tau}/\Re$ according to Eqs. (16) and (17) as well as to Table 3. Note also that for sensor implementations based on critically coupled and under-coupled RRs as defined in Table 3, the quality ratio c_Q of the all-pass resonator is twice that of an add-drop resonator and can be expressed by the respective optical output contrast $\hat{T}$,

$$c_{\mathrm{Q,RR}_{\mathrm{AP}}^{\mathrm{CC,UC}}} = 2c_{\mathrm{Q,RR}_{\mathrm{AD}}^{\mathrm{CC,UC}}} = \frac{1+\sqrt{1-\hat{T}}}{2}. \tag{C4}$$

For both critically coupled and under-coupled resonator add-drop RRs, the optical output contrast $\hat{T}$ of the through port is twice that of the drop port.

APPENDIX D: DETAILS ON THE OPTIMIZATION OF THE OPTOELECTRONIC EFFECTIVE-INDEX SENSITIVITY

D.1. Ring Coupling Optimization

An intuitive choice for the coupling strength of RR-based sensor implementations would be critical coupling that leads to a complete signal suppression in the through port at resonance, i.e., maximum output contrast $\hat{T}$. However, the performance metric that is most relevant to sensors is the output power change for a small Δn_{e}. We,

Table 6. Lorentzian Approximation of the Optical Power Transmission of a Ring Resonator Close to a Resonance[a,b,c]

	Lorentzian Approximation of Optical Power Transmission $T_{\mathrm{Lor}}(\Delta x) = \hat{T}\frac{1}{1+\left(\frac{2\Delta x}{\Delta x_{\mathrm{FWHM}}}\right)^2}$	Resonance Width (FWHM) Δx_{FWHM}	Optimum Operating Point (Detuning from a Resonance Condition) $\Delta x_{\mathrm{OP,RR,opt}}$	Slope in Optimum Operating Point $\frac{\partial T_{\mathrm{Lor}}}{\partial(\Delta x)}\vert_{\Delta x=\Delta x_{\mathrm{OP,opt}}}$
Phase	$T_{\mathrm{Lor}}(\Delta\varphi_{\mathrm{RR}}) = \hat{T}\frac{1}{1+\left(\frac{2\Delta\varphi_{\mathrm{RR}}}{\alpha L/c_Q}\right)^2}$	$\Delta\varphi_{\mathrm{FWHM,RR}} = \frac{\alpha L}{c_Q}$	$\Delta\varphi_{\mathrm{OP,RR,opt}} = \pm\frac{1}{2\sqrt{3}}\Delta\varphi_{\mathrm{FWHM,RR}}$	$\frac{3}{8}2\sqrt{3}\frac{\hat{T}}{\Delta\varphi_{\mathrm{FWHM,RR}}}$
Frequency	$T_{\mathrm{Lor}}(\Delta\omega) = \hat{T}\frac{1}{1+\left(\frac{2\Delta\omega}{\omega_{\mathrm{res}}/Q}\right)^2}$	$\Delta\omega_{\mathrm{FWHM,RR}} = \frac{\omega_{\mathrm{res}}}{Q}$	$\Delta\omega_{\mathrm{OP,RR,opt}} = \pm\frac{1}{2\sqrt{3}}\Delta\omega_{\mathrm{FWHM,RR}}$	$\frac{3}{8}2\sqrt{3}\frac{\hat{T}}{\Delta\omega_{\mathrm{FWHM,RR}}}$
Eff. index	$T_{\mathrm{Lor}}(\Delta n_{\mathrm{e}}) = \hat{T}\frac{1}{1+\left(\frac{2\Delta n_{\mathrm{e}}}{n_{\mathrm{eg}}/Q}\right)^2}$	$\Delta n_{\mathrm{e,FWHM,RR}} = \frac{n_{\mathrm{eg}}}{Q}$	$\Delta n_{\mathrm{e,OP,RR,opt}} = \pm\frac{1}{2\sqrt{3}}\Delta n_{\mathrm{e,FWHM,RR}}$	$\frac{3}{8}2\sqrt{3}\frac{\hat{T}}{\Delta n_{\mathrm{e,FWHM,RR}}}$

[a]Column 2 shows the optical power transmission T_{Lor} that allows us to approximate the true power transmission T according to Table 5, Column 2 through Eq. (C2). The variable Δx refers to a small offset of the phase, the frequency, or the effective refractive index with respect to its on-resonance value, $\Delta x \in \{\Delta\varphi_{\mathrm{RR}}, \Delta\omega, \Delta n_{\mathrm{e}}\}$. Column 3 specifies the full width at half-maximum (FWHM) with respect to the associated quantity, where the quality ratio c_Q refers to the ratio of the loaded Q-factor Q and the intrinsic, unloaded Q-factor Q_i, $c_Q = Q/Q_i < 1$ [see Eq. (17)]. Columns 4 and 5 finally give the respective optimum detuning related to the inflection point of the Lorentzian, which features the highest slope and, thus, offers the highest sensitivity with respect to changes of the phase, the frequency, or the effective refractive index.

[b]All these quantities are expressed as a function of the ring resonator round trip phase offset $\Delta\varphi_{\mathrm{RR}}$ (Row 2), the frequency offset $\Delta\omega$ (Row 3), and the offset Δn_{e} of effective refractive index (Row 4) from the respective on-resonance value.

[c]The relations are general and can be adapted to the various sensor implementations by using the corresponding Q-factor Q, quality ratio c_Q, and optical output contrast $\hat{T} = \hat{\tau}/\Re$ according to Eqs. (16) and (17) as well as to Table 3.

therefore, search for an optimum operating point that exhibits the largest slope of the optical power transmission with respect to Δn_e. Within the Lorentzian approximation, an optimum operating point is found at the inflection point, located at a distance $\pm\Delta\varphi_{FWHM}/(2\sqrt{3})$ away from the resonance (see Column 4 of Table 6). The slope in the optimum operating point is fully determined by the corresponding resonance height and width (see Column 5 of Table 6). With $\Delta n_{e,FWHM,RR} = n_{eg}/Q$ (see Table 6) and $Q = c_Q n_{eg} k_0/\alpha$, as shown in Eq. (16), we can derive Eq. (20) for the peak optoelectronic effective-index sensitivity $\hat{\tau} = \Re\hat{T}$ as used in Subsection 4.2d,

$$S_{e,\tau,peak} = \frac{3}{8}2\sqrt{3}\frac{\hat{\tau}}{\Delta n_{e,FWHM,RR}} = \frac{3}{8}2\sqrt{3}\frac{Q}{n_{eg}}\hat{\tau} = \frac{3}{8}2\sqrt{3}\frac{k_0}{\alpha}c_Q\hat{\tau}. \qquad \textbf{(D1)}$$

The effective output contrast $\hat{\tau} = \Re\hat{T}$ is given by the electric readout responsivity $\Re$ and the optical transmission contrast $\hat{T}$, which is obtained from Column 5 in Table 5. Note that $\hat{T}$ is fully defined by the amplitude transmission factors ρ_1 and ρ_2 of the RR coupling sections and the round trip amplitude transmission factor $a = \exp(-\alpha L/2)$ with modal power loss coefficient α and round trip length L. The quality ratio c_Q can be directly derived from $\hat{T}$ via Eq. (C4) and, hence, also depends on ρ_1, ρ_2, α, and L. As a consequence, for a given L and α, we can calculate the optimum coupling coefficients $\rho_{1,opt}$ and $\rho_{2,opt}$ that yield the maximum achievable optoelectronic effective-index sensitivity $S_{e,\tau,max}$ for each RR-based sensor implementation—the results are shown in the last column of Table 3 and plotted in Fig. 4. We find that a slightly under-coupled (UC) operation yields the best results, where the increased Q-factor and, thus, c_Q outweighs the decrease in output contrast $\hat{\tau}$. For an all-pass RR with optimum under-coupling (RR_{AP}^{UC}), an amplitude-transmission coefficient of $(\rho_{1,opt})_{AP}^{UC} = (\sqrt{\rho_{1,opt}})_{AP}^{CC} = \sqrt{a}$ has to be chosen, whereas the implementations based on add-drop RRs (RR_{AD}^{UC}) and optional balanced detection (RR_{BD}^{UC}) require $(\rho_{1,opt})_{AD,BD}^{UC} = (\sqrt{\rho_{1,opt}})_{AD,BD}^{CC} = a$ and $(\rho_{2,opt})_{AD,BD}^{UC} = (\rho_{2,opt})_{AD,BD}^{CC} = a$. The corresponding values for the quality ratio c_Q, the output contrast $\hat{\tau} = \Re\hat{T}$, and the effective optoelectronic transmission in the optimum operating point $\tau_{OP} = \Re T_{OP}$ for the various systems are detailed in Table 3. Here, $\tau_{OP}/\Re$ always equals $1 - {}^3/_4\hat{T}$ and ${}^3/_4\hat{T}$ for the through and drop ports, respectively, which is relevant for noise figures and feedback control.

D.2. Device-Length Optimization

For RRs, the optoelectronic effective-index sensitivity $S_{e,\tau}$, can be maximized by optimum choice of c_Q as described in the previous paragraph. In contrast to that, the round trip length L does not have relevant influence on $S_{e,\tau}$ [see Fig. 4(b)]. This is due to the fact that the sensitivity is directly linked to the loaded Q-factor $Q = Q_i/c_Q$ as long as the resonator can be described by a Lorentzian approximation [see Eq. (D1)], where the intrinsic Q-factor Q_i is independent of the ring round trip length L [see Eq. (16)]. As a consequence, changing the round trip length L while maintaining the same quality ratio c_Q does not influence the optoelectronic effective-index sensitivity as long as $\alpha L \ll 1$ [see Fig. 4(b)]. For $\alpha L \gtrsim 1$, the Lorentzian approximation and the associated relationship between optoelectronic effective-index sensitivity and Q-factor are not valid anymore, and the optoelectronic effective-index sensitivity decreases as the round trip length L is increased. In this regime, the benefits of using a resonator disappear. Note that, for typical waveguide losses of 10 dB/cm ($\alpha = 2.3\ \mathrm{cm}^{-1}$), the critical round trip length $L = 1/\alpha$ is, thus, in the millimeter range. In practical sensor designs, the length $L < 1/\alpha$ can, hence, be chosen freely over

a wide range, e.g., to achieve an advantageous FSR that is compatible with the frequency tuning rang of the light source, or to avoid excessive bend loss, which are not considered in our analysis.

For MZIs, the arm length L is a critical parameter, and the peak optoelectronic effective-index sensitivity in the optimum operating point can be expressed by Eq. (20) for any output contrast $\hat{\tau}$ as given in Table 2,

$$S_{\mathrm{e},\tau,\mathrm{peak,MZI}} = \frac{\hat{\tau}}{2} k_0 L \propto \mathrm{e}^{-\alpha L}\, L. \tag{D2}$$

Unlike RRs, the peak optoelectronic effective-index sensitivity of an MZI can be maximized by proper choice of the arm length $L_{\mathrm{opt,MZI}} = 1/\alpha$ that offers an ideal trade-off between low output power at large L and small phase shifts in case L is chosen too small. This means that a waveguide technology with lower waveguide loss allows for larger sensitivity but requires longer MZI arms to unfold its full potential.

D.3. Light-Source Linewidth

To quantify the impact of drive laser frequency noise on the optoelectronic effective-index sensitivity in Subsection 4.2d, we assume a laser diode (LD) emitting at an optical center frequency ω_0 and having a power spectral density $S_{P_\mathrm{i}}(\omega)$, which is characterized by the linewidth $\Delta\omega_{\mathrm{FWHM,LD}}$. The laser is connected to a sensor system with optical power transmission $T(\omega)$, characterized by spectral features such as a RR resonance with an FWHM $\Delta\omega_{\mathrm{FWHM,RR}}$ or a periodic MZI response with a FSR $\Delta\omega_{\mathrm{FSR,MZI}}$. If the laser linewidth is much smaller than the spectral features of the sensor transmission, the output current can be calculated by multiplying the readout responsivity $\Re$ with the total laser power $\iint S_{P_\mathrm{i}}(\omega)\,\mathrm{d}\omega$ and the sensor transmission $T(\omega_0)$ at the center frequency ω_0 of the laser. However, if the laser linewidth is comparable to the width of the spectral features of the sensor transmission characteristics, the power spectrum of the laser and the sensor transmission spectrum have to be multiplied before integrating the resulting power spectral density over the relevant frequency range,

$$I_\mathrm{o}(\omega_0) = \begin{cases} \Re\; T(\omega_0) \int S_{P_\mathrm{i}}(\omega)\mathrm{d}\omega, & \text{for } \Delta\omega_{\mathrm{FWHM,LD}} \ll (\Delta\omega_{\mathrm{FWHM,RR}} \text{ or } \Delta\omega_{\mathrm{FSR,MZI}}), \\ \Re \int S_{P_\mathrm{i}}(\omega)\, T(\omega)\mathrm{d}\omega, & \text{else.} \end{cases} \tag{D3}$$

The associated optoelectronic effective-index sensitivity $S_{\mathrm{e},\tau}(\omega_0)$ is then obtained by taking the derivative with respect to n_e and by normalizing the result by the total laser power. Using $\tau(\omega) = \Re\, T(\omega)$ for the single-output sensor implementations, this leads to

$$S_{\mathrm{e},\tau}(\omega_0) = \begin{cases} \frac{\partial \tau(\omega_0)}{\partial n_\mathrm{e}} & \text{for } \Delta\omega_{\mathrm{FWHM,LD}} \ll (\Delta\omega_{\mathrm{FWHM,RR}} \text{ or } \Delta\omega_{\mathrm{FSR,MZI}}), \\ \frac{\int S_{P_\mathrm{i}}(\omega)(\partial\tau(\omega)/\partial n_\mathrm{e})\mathrm{d}\omega}{\int S_{P_\mathrm{i}}(\omega)\mathrm{d}\omega} & \text{else.} \end{cases} \tag{D4}$$

The larger the width of the laser spectrum is compared to that of the spectral features of the sensor, the more the optoelectronic effective-index sensitivity is "blurred", leading to a decreased sensitivity with respect to the value obtained for a sharp laser line in the optimum operating point [see Fig. 4(c)]. For the plot in Fig. 4(c), we calculate $S_{e,\tau}$ for pure Lorentzian- and Gaussian-shaped power spectral densities $S_{P_\mathrm{i}}(\omega)$, both characterized by the same linewidth $\Delta\omega_{\mathrm{FWHM,LD}}$. As detailed in [54,99], these Lorentzian and Gaussian line shapes can represent corner cases for the line shape of typical lasers. Depending on the specific laser and operation conditions, the laser line shape will typically be a mixture of these two profiles—such a convolution is known as a Voigt profile.

As a numerical example, a low-cost laser diode emitting at a center wavelength of $\lambda_0 = 1.55\,\mu\text{m}$ with a typical linewidth of $\Delta\omega_{\text{FWHM,LD}} = 2\pi \times 10\,\text{MHz}$ will set an upper limit for the Q-factor of 200,000 before sensitivity degradation is to be expected. In contrast to this, MZI-based sensors are generally not subject to such limitations: the devices can always be designed with balanced arms of approximately identical group delays, leading to large FSR $\Delta\omega_{\text{FSR,MZI}} \gg \Delta\omega_{\text{FWHM,LD}}$.

APPENDIX E: FREQUENCY DEPENDENCY OF THE MZI PHASE IN THE OPERATING POINT

The MZI phase difference in an operating point (OP) at a wavenumber $k_0 = \omega_0/c$ with common base arm length L and common base effective refractive index n_e as well as an geometrical arm length difference ΔL and initial effective-refractive-index difference $\Delta n_{\text{e},0}$ can be written according to Eq. (11) as $\varphi_{\text{OP,MZI}} = k_0 = (\Delta L n_\text{e} - L\Delta n_{\text{e},0})$. The frequency dependence of this phase difference can be expressed by taking the derivative with respect to ω. The result can be simplified by using an effective group refractive index n_eg, which is common to both arms, as well as an initial difference $\Delta n_{\text{eg},0}$ of the effective group refractive index between the two arms. If we assume that the waveguides in the two arms have similar cross sections and that the corresponding refractive indices and dispersion relations are, hence, similar as well, we can assume that $\Delta n_{\text{eg},0}/\Delta n_{\text{e},0} \approx n_\text{eg}/n_\text{e}$. This leads to

$$\frac{\partial\varphi_{\text{OP,MZI}}}{\partial\omega} = \frac{1}{c}(\Delta L n_\text{eg} - L\Delta n_{\text{eg},0}) = \frac{n_\text{eg}}{n_\text{e}}\frac{1}{c}(\Delta L n_\text{e} - L\Delta n_{\text{e},0}) \approx \frac{n_\text{eg}}{n_\text{e}}\frac{\varphi_{\text{OP,MZI}}}{\omega}. \quad \textbf{(E1)}$$

APPENDIX F: EXPERIMENTAL EXTRACTION OF THE LASER FREQUENCY STABILITY

In Sections 4 and 5, we discuss laser frequency noise as one of the most important impairments for RR-based sensor implementations. The frequency noise characteristics of a laser can be obtained with the help of a heterodyne detection scheme, which transfers the relevant frequency noise characteristics from the optical domain into the electrical domain. In principle, this is achieved by first tuning the optical frequency f_LO of a highly stable reference local oscillator (LO) laser close to the optical frequency f_DUT of the laser device under test (DUT), then superimposing the two optical signals and subsequently recording the combined optical signal with a photodetector. The photocurrent is proportional to the square of the sum of the electrical fields and, hence, contains a term at the beat frequency $f_\text{beat} = f_\text{DUT} - f_\text{LO}$, which carries the phase and frequency noise properties of the laser DUT. The beat frequency f_beat has to be chosen such that the beat signal including potential frequency drift of the DUT and the LO laser is within the electronic acquisition bandwidth of the acquisition system. The beat signal can be recorded with a single photodiode, with balanced detection on two photodiodes, or via an in-phase quadrature (IQ) demodulation scheme consisting of two pairs of balanced photodiodes [100]. In the case of the IQ demodulation scheme, as sketched in Fig. 9(a), we construct a complex signal S_IQ with magnitude $\hat{I}_\text{IQ}$ from the two photocurrents that represent the in-phase (I) and the quadrature-phase (Q) components of the complex signal,

$$S_\text{IQ}(t) = I_\text{I} + \text{j}\, I_\text{Q} = \hat{I}_\text{IQ}\exp(\text{j}\,\Phi(t)). \quad \textbf{(F1)}$$

Due to the frequency offset between the LO and DUT, the total phase $\Phi(t)$ of S_IQ increases or decreases monotonously with time and can be obtained by taking the

argument of S_{IQ} and by the associated time-series of phases. Neglecting the phase noise of the LO, the phase noise of the DUT can be directly reconstructed from the phase noise Φ_n of the beat signal, which is obtained by subtracting a linear phase fit with a mean beat frequency $\overline{f_{\mathrm{beat}}}$ from the unwrapped phase $\Phi(t)$,

$$\Phi_{\mathrm{n}}(t) = \Phi(t) - 2\pi\,\overline{f_{\mathrm{beat}}}\,t. \tag{F2}$$

The noise of the instantaneous frequency, f_{n}, is then calculated via the time-derivative of the phase noise Φ_{n}. Practically, this is achieved by calculating the discrete derivative from a set of discrete measurement points spaced by the same time interval τ as

$$f_{\mathrm{n}}(t) = \frac{1}{2\pi}\frac{\partial\Phi_{\mathrm{n}}}{\partial t} = \frac{\Phi_{\mathrm{n}}(t) - \Phi_{\mathrm{n}}(t-\tau)}{2\pi\tau}. \tag{F3}$$

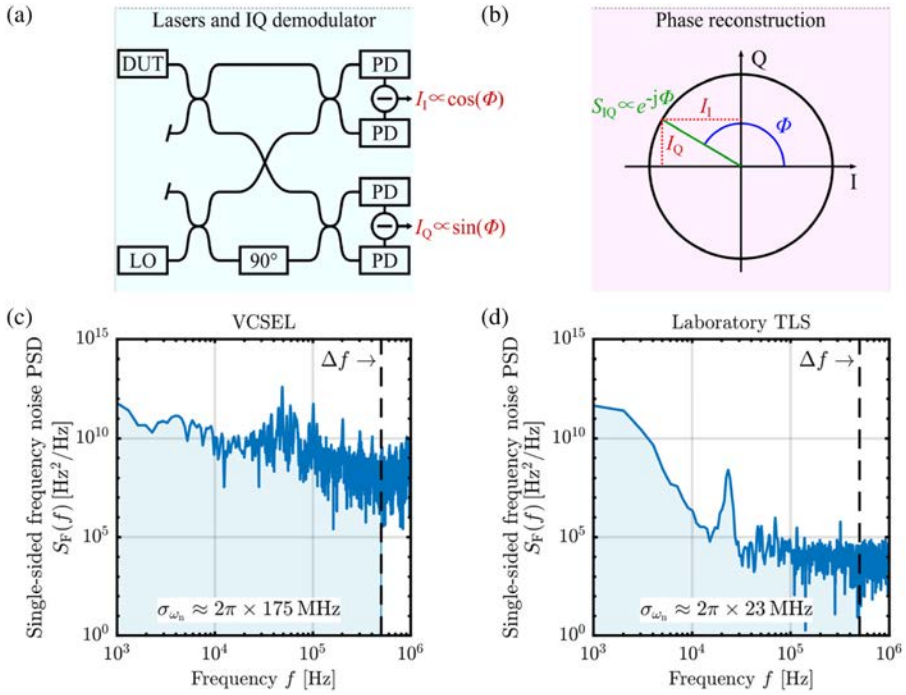

Details on the frequency noise characterization of lasers in our experiments. (a) Measurement setup for recording the beat frequency between the laser device under test (DUT: VCSEL or TLS) and a reference local-oscillator (LO) laser using an IQ demodulation detection scheme with two pairs of balanced output photodiodes (PD). The graphic was adapted from the application note of the Keysight N4391A Optical Modulation Analyzer that was used in this experiment. (b) The differential currents I_I and I_Q from the two balanced photodiode pairs generate the in-phase (I) and quadrature-phase components (Q) of the complex signal S_{IQ}. Assuming a highly stable LO laser, the phase and frequency noise characteristics of S_{IQ} can be attributed to the respective noise characteristics of the laser DUT. (c), (d) One-sided frequency noise power spectral densities of a typical VCSEL and TLS calculated from the extracted phase $\Phi(t)$ of the beat signal according to Eqs. (F3) and (F4). We extract exemplary angular frequency variances $\sigma^2_{\omega_{\mathrm{n}}}$ for each laser by integrating $S_{\mathrm{F}}(f)$ from low frequencies of $1/T_{\mathrm{obs}} = 1$ kHz up to the measurement acquisition bandwidth $\Delta f = 500$ kHz. In this case, the standard deviation $\sigma_{\omega_{\mathrm{n}}}$ of the VCSEL and the TLS emission frequency differ by nearly 1 order of magnitude.

Generally, laser phase noise corresponds to a random walk, i.e., a non-stationary stochastic process with diverging variance. For a laser controlled by some frequency stabilization process, however, we may assume that the frequency variations are mean-free and that they can be described by an ergodic stationary stochastic process. According to the Wiener–Khinchin theorem, the one-sided power spectral density $S_{\mathrm{F}}(f)$ of the frequency noise $f_{\mathrm{n}}(t)$ can then be calculated as the Fourier-transform of its autocorrelation function ρ_{ff},

$$S_{\mathrm{F}}(f) = 2\int_{-\infty}^{\infty} \rho_{\mathrm{ff}}(\tau)\exp(-\mathrm{j}\,2\pi f\tau)\mathrm{d}\tau;$$

$$\rho_{\mathrm{ff}}(\tau) = \overline{f_{\mathrm{n}}(t)\,f_{\mathrm{n}}(t+\tau)} = \lim_{T\to\infty}\frac{1}{2T}\int_{-T}^{T} f_{\mathrm{n}}(t)\,f_{\mathrm{n}}(t+\tau)\mathrm{d}t. \qquad \textbf{(F4)}$$

For a given optoelectronic acquisition bandwidth Δf of our sensor system, the variance $\sigma^2_{\omega_{\mathrm{n}}}$ of the angular laser frequency noise can theoretically be obtained by calculating the noise up to this frequency,

$$\sigma^2_{\omega_n} = (2\pi)^2\int_{1/T_{\mathrm{obs}}}^{\Delta f} S_{\mathrm{F}}(f)\mathrm{d}f, \qquad \textbf{(F5)}$$

where T_{obs} denotes the overall observation time during a complete set of measurements and where the optoelectronic acquisition bandwidth Δf is related to the ADC sampling frequency f_{s} by the sampling theorem, $f_{\mathrm{s}} \geq 2\Delta f$. Note that for long observation times $T_{\mathrm{obs}} \to \infty$, the integral in Eq. (39) can only be evaluated if $S_{\mathrm{F}}(f)$ does not diverge for $f \to 0$, i.e., $S_{\mathrm{F}}(f)$ must have an upper bound of the form $1/f^{\gamma}$ for $f \to 0$, where $\gamma < 1$—otherwise the frequency variance $\sigma^2_{\omega_{\mathrm{n}}}$ diverges with T_{obs}. For laser sources that do not fulfill this condition intrinsically, e.g., due to frequency drift, it might be necessary to use a frequency stabilization mechanism to ensure mean-free frequency variance that does not diverge with long observation times $T_{\mathrm{obs}} \to \infty$. For laser sources with feedback compensation of frequency drifts, we may approximate the one-sided power spectral density by a constant $S_{\mathrm{F}}(f) = S_{\mathrm{F0}}$ that leads to the same spectral power as the truly measured frequency noise spectrum within the frequency interval $[1/T_{\mathrm{obs}}, \Delta f]$. Exploiting the fact that the observation time is usually much larger than the sampling time and, hence, $1/T_{\mathrm{obs}} \ll \Delta f$, the laser frequency variance can be approximated by

$$\sigma^2_{\omega} = 4\pi^2 S_{\mathrm{F0}}\Delta f. \qquad \textbf{(F6)}$$

In Figs. 9(c) and 9(d), we show the one-sided power spectral density $S_{\mathrm{F}}(f)$ of the frequency noise of a typical VCSEL and benchtop-type tunable light source (ANDO AQ4321A) within a frequency interval between $1/T_{\mathrm{obs}} = 1$ kHz and $\Delta f = 500$ kHz. The standard deviation $\sigma^2_{\omega_{\mathrm{n}}}$ of the angular laser frequency noise is calculated according to Eq. (39) by integrating the frequency noise spectrum over this frequency range, which leads to $\sigma^2_{\omega_{\mathrm{n}}} = 2\pi \times 175$ MHz for the VCSEL and $\sigma^2_{\omega_{\mathrm{n}}} = 2\pi \times 23$ MHz for the TLS. These values are in fair quantitative agreement with the frequency variations of $\sigma^2_{\omega_{\mathrm{n}}} = 2\pi \times 435$ MHz and $\sigma^2_{\omega_{\mathrm{n}}} = 2\pi \times 10$ MHz that were independently estimated from the ring resonator measurement (see Section 5).

In Subsection 4.3a, we assume a typical frequency noise variance $\sigma^2_{\omega_{\mathrm{n}}} = 2\pi \times 100$ MHz at a rather low acquisition bandwidth of $\Delta f = 100$ Hz, which is estimated from the VCSEL measurement data in Fig. 9(c). Note that the equipment used in the experiment did not allow us to record sufficiently long beat signals to directly derive the frequency noise spectrum below 1 kHz. We, therefore, estimate the low-frequency part by extrapolating the measured frequency noise spectrum within the

interval $f \in [1\,\mathrm{kHz}, 10\,\mathrm{kHz}]$ toward lower frequencies $f < 1\,\mathrm{kHz}$. We use a fit based on a model function of the form $S_\mathrm{F}(f) \approx S_\mathrm{F1} \times 1/f^\gamma$, which leads to parameters $S_\mathrm{F1} = 4.6 \cdot 10^{15}\,\mathrm{Hz}^2/\mathrm{Hz}$ and $\gamma = 1.4$. As $\gamma > 1$, the frequency variance $\sigma^2_{\omega_\mathrm{n}}$ diverges for long observation times T_obs [see Eq. (39)]. The finite value $\sigma^2_{\omega_\mathrm{n}} = 2\pi \times 100\,\mathrm{MHz}$ is obtained by limiting the observation time to $T_\mathrm{obs} = 1\,\mathrm{s}$ and, hence, integrating the extrapolated data according to Eq. (39) only within the frequency interval between $1/T_\mathrm{obs} = 1\,\mathrm{Hz}$ and $\Delta f = 100\,\mathrm{Hz}$.

In practical sensor systems that rely on low-cost lasers with diverging frequency spectra of the form $S_\mathrm{F}(f) \propto 1/f^\gamma$ with $\gamma > 1$, continuous operation with infinitely long observation times requires some sort of frequency stabilization, which effectively reduces the strong frequency noise contribution at low Fourier frequencies and, thus, results in a finite frequency variance $\sigma^2_{\omega_\mathrm{n}}$ for $T_\mathrm{obs} \to \infty$. Clearly, the implementation of such a frequency stabilization mechanism increases the complexity of the overall sensor system. For a quantitatively reliable estimation of the frequency variance $\sigma^2_{\omega_\mathrm{n}}$ and the associated LoD contribution, it is essential to characterize the laser source under the operation and data acquisition conditions that are relevant for the respective use case.

FUNDING

Alfried Krupp von Bohlen und Halbach-Stiftung; Robert Bosch GmbH; Karlsruhe School of Optics and Photonics.

ACKNOWLEDGMENT

We acknowledge Dr. Stefan Wolf for supporting the experimental evaluation.

DISCLOSURES

The author declares no conflicts of interest.

REFERENCES

1. S. Schmidt, J. Flueckiger, W. Wu, S. M. Grist, S. T. Fard, V. Donzella, P. Khumwan, E. R. Thompson, Q. Wang, P. Kulik, J. Kirk, K. C. Cheung, L. Chrostowski, and D. Ratner, "Improving the performance of silicon photonic rings, disks, and Bragg gratings for use in label-free biosensing," Proc. SPIE **9166**, 91660M (2014).
2. V. M. N. Passaro, B. Troia, M. La Notte, and F. De Leonardis, "Chemical sensors based on photonic structures," in *Advances Chemical Sensors*, W. Wang, ed. (InTech, 2012).
3. S. Janz, A. Densmore, D.-X. Xu, P. Waldron, J. Lapointe, J. H. Schmid, T. Mischki, G. Lopinski, A. Delâge, R. McKinnon, P. Cheben, and B. Lamontagne, "Silicon photonic wire waveguide sensors," in *Advanced Photonic Structures for Biological and Chemical Detection*, X. Fan, ed. (Springer, 2009), pp. 229–264.
4. P. Kozma, F. Kehl, E. Ehrentreich-Förster, C. Stamm, and F. F. Bier, "Integrated planar optical waveguide interferometer biosensors: a comparative review," Biosens. Bioelectron. **58**, 287–307 (2014).
5. A. Densmore, D.-X. Xu, S. Janz, P. Waldron, J. Lapointe, T. Mischki, G. Lopinski, A. Delâge, J. Schmid, and P. Cheben, "Sensitive label-free biomolecular detection using thin silicon waveguides," Adv. Opt. Technol. **2008**, 725967 (2008).

6. L. Chrostowski, S. Grist, J. Flueckiger, W. Shi, X. Wang, E. Ouellet, H. Yun, M. Webb, B. Nie, Z. Liang, K. Cheung, S. Schmidt, D. Ratner, and N. Jaeger, "Silicon photonic resonator sensors and devices," Proc. SPIE **8236**, 823620 (2012).
7. X. Fang, I. M. White, S. I. Shopova, H. Zhu, J. D. Suter, and Y. Sun, "Sensitive optical biosensors for unlabeled targets: a review," Anal. Chim. Acta. **620**, 8–26 (2008).
8. A. Densmore, M. Vachon, D.-X. Xu, S. Janz, R. Ma, Y.-H. Li, G. Lopinski, A. Delâge, J. Lapointe, C. C. Luebbert, Q. Y. Liu, P. Cheben, and J. H. Schmid, "Silicon photonic wire biosensor array for multiplexed real-time and label-free molecular detection," Opt. Lett. **34**, 3598–3600 (2009).
9. C. Barrios, M. Bañuls, V. González-Pedro, K. Gylfason, B. Sánchez, A. Griol, A. Maquieira, H. Sohlström, M. Holgado, and R. Casquel, "Label-free optical biosensing with slot-waveguides," Opt. Lett. **33**, 708–710 (2008).
10. K. De Vos, I. Bartolozzi, E. Schacht, P. Bienstman, and R. Baets, "Silicon-on-insulator microring resonator for sensitive and label-free biosensing," Opt. Express **15**, 7610–7615 (2007).
11. B. Jalali and S. Fathpour, "Silicon photonics," J. Lightwave Technol. **24**, 4600–4615 (2006).
12. R. Soref, "The past, present, and future of silicon photonics," IEEE J. Sel. Top. Quantum Electron. **12**, 1678–1687 (2006).
13. M. Hochberg and T. Baehr-Jones, "Towards fabless silicon photonics," Nat. Photonics **4**, 492–494 (2010).
14. D. Thomson, A. Zilkie, J. E. Bowers, T. Komljenovic, G. T. Reed, L. Vivien, D. Marris-Morini, E. Cassan, L. Virot, J.-M. Fédéli, J.-M. Hartmann, J. H. Schmid, D.-X. Xu, F. Boeuf, P. O'Brien, G. Z. Mashanovich, and M. Nedeljkovic, "Roadmap on silicon photonics," J. Opt. **18**, 073003 (2016).
15. P. Muñoz, G. Micó, L. A. Bru, D. Pastor, D. Pérez, J. D. Doménech, J. Fernández, R. Baños, B. Gargallo, R. Alemany, A. M. Sánchez, J. M. Cirera, R. Mas, and C. Domínguez, "Silicon nitride photonic integration platforms for visible, near-infrared and mid-infrared applications," Sensors **17**, 2088 (2017).
16. D. J. Blumenthal, R. Heideman, D. Geuzebroek, A. Leinse, and C. Roeloffzen, "Silicon nitride in silicon photonics," Proc. IEEE **106**, 2209–2231 (2018).
17. T. A. Huffman, G. M. Brodnik, C. Pinho, S. Gundavarapu, D. Baney, and D. J. Blumenthal, "Integrated resonators in an ultralow loss Si_3N_4/SiO_2 platform for multifunction applications," IEEE J. Sel. Top. Quantum Electron. **24**, 5900209 (2018).
18. W. D. Sacher, J. C. Mikkelsen, Y. Huang, J. C. C. Mak, Z. Yong, X. Luo, Y. Li, P. Dumais, J. Jiang, D. Goodwill, E. Bernier, P. G.-Q. Lo, and J. K. S. Poon, "Monolithically integrated multilayer silicon nitride-on-silicon waveguide platforms for 3-D photonic circuits and devices," Proc. IEEE **106**, 2232–2245 (2018).
19. A. L. Washburn, L. C. Gunn, and R. C. Bailey, "Label-free quantitation of a cancer biomarker in complex media using silicon photonic microring resonators," Anal. Chem. **81**, 9499–9506 (2009).
20. W.-C. Lai, S. Chakravarty, X. Wang, C. Lin, and R. T. Chen, "On-chip methane sensing by near-IR absorption signatures in a photonic crystal slot waveguide," Opt. Lett. **36**, 984–986 (2011).
21. Y. Zou, K. Vijayraghavan, P. Wray, S. Chakravarty, M. A. Belkin, and R. T. Chen, "Monolithically integrated quantum cascade lasers, detectors and dielectric waveguides at 9.5 μm for far-infrared lab-on-chip chemical sensing," in *CLEO*, San Jose, California, USA (Optical Society of America, 2015), paper STu4I.2.

22. S. Chakravarty, X. Chen, N. Tang, W.-C. Lai, Y. Zou, H. Yan, and R. T. Chen, "Review of design principles of 2D photonic crystal microcavity biosensors in silicon and their applications," Front. Optoelectron. **9**, 206–224 (2016).
23. H. Yan, N. Tang, S. Chakravarty, and R. T. Chen, "High-sensitivity high-throughput chip based biosensor array for multiplexed detection of heavy metals," in *BiOS (Photonics West)*, San Francisco, California, USA (2016).
24. W. Lai, S. Chakravarty, Y. Zou, and R. T. Chen, "Silicon nano-membrane based photonic crystal microcavities for high sensitivity bio-sensing," Opt. Lett. **37**, 1208–1210 (2012).
25. W. Lai, S. Chakravarty, Y. Zou, Y. Guo, and R. T. Chen, "Slow light enhanced sensitivity of resonance modes in photonic crystal biosensors," Appl. Phys. Lett. **102**, 041111 (2013).
26. A. L. Washburn, M. S. Luchansky, A. L. Bowman, and R. C. Bailey, "Quantitative, label-free detection of five protein biomarkers using multiplexed arrays of silicon photonic microring resonators," Anal. Chem. **82**, 69–72 (2010).
27. M. Iqbal, M. A. Gleeson, B. Spaugh, F. Tybor, W. G. Gunn, M. Hochberg, T. Baehr-Jones, R. C. Bailey, and L. C. Gunn, "Label-free biosensor arrays based on silicon ring resonators and high-speed optical scanning instrumentation," IEEE J. Sel. Top. Quantum Electron. **16**, 654–661 (2010).
28. E. Luan, H. Shoman, D. M. Ratner, K. C. Cheung, and L. Chrostowski, "Silicon photonic biosensors using label-free detection," Sensors **18**, 3519 (2018).
29. Y. Zou, S. Chakravarty, C. Chung, X. Xu, and R. T. Chen, "Mid-infrared silicon photonic waveguides and devices," Photon. Res. **6**, 254–276 (2018).
30. E. Makarona, P. Petrou, S. Kakabakos, K. Misiakos, and I. Raptis, "Point-of-need bioanalytics based on planar optical interferometry," Biotechnol. Adv. **34**, 209–233 (2016).
31. A. F. Gavela, D. G. García, J. C. Ramirez, and L. M. Lechuga, "Last advances in silicon-based optical biosensors," Sensors **16**, 285 (2016).
32. I. M. White and X. Fan, "On the performance quantification of resonant refractive index sensors," Opt. Express **16**, 1020–1028 (2008).
33. W. Bogaerts, P. De Heyn, T. Van Vaerenbergh, K. De Vos, S. K. Selvaraja, T. Claes, P. Dumon, P. Bienstman, D. Van Thourhout, and R. Baets, "Silicon microring resonators," Laser Photon. Rev. **6**, 47–73 (2012).
34. X. Wang, J. Flueckiger, S. Schmidt, S. Grist, S. T. Fard, J. Kirk, M. Doerfler, K. C. Cheung, D. M. Ratner, and L. Chrostowski, "A silicon photonic biosensor using phase-shifted Bragg gratings in slot waveguide," J. Biophoton. **6**, 821–828 (2013).
35. F. Koyama, "Advances and new functions of VCSEL photonics," Opt. Rev. **21**, 893–904 (2014).
36. J. Milvich, D. Kohler, W. Freude, and C. Koos, "Surface sensing with integrated optical waveguides: a design guideline," Opt. Express **26**, 19885–19906 (2018).
37. D. Kita, J. Michon, S. Johnson, and J. Hu, "Are slot and sub-wavelength grating waveguides better than strip waveguides for sensing?" Optica **5**, 1046–1054 (2018).
38. S. Dante, D. Duval, B. Sepúlveda, A. B. González-Guerrero, J. R. Sendra, and L. M. Lechuga, "All-optical phase modulation for integrated interferometric biosensors," Opt. Express **20**, 7195–7205 (2012).
39. R. Halir, L. Vivien, X. Le Roux, D. X. Xu, and P. Cheben, "Direct and sensitive phase readout for integrated waveguide sensors," IEEE Photon. J. **5**, 6800906 (2013).
40. E. Clarke, *Circuit Analysis of AC Power Systems* (Wiley, 1943), Vol. **1**.

41. J. Milvich, D. Kohler, W. Freude, and C. Koos, "Mach-Zehnder interferometer readout for instantaneous sensor calibration and extraction of endlessly unwrapped phase," in *IEEE Photonics Conference (IPC)* (2017), pp. 567–568.
42. Í. Molina-Fernández, J. Leuermann, A. Ortega-Moñux, J. G. Wangüemert-Pérez, and R. Halir, "Fundamental limit of detection of photonic biosensors with coherent phase read-out," Opt. Express **27**, 12616–12629 (2019).
43. M. Bachmann, P. A. Besse, and H. Melchior, "General self-imaging properties in $N \times N$ multimode interference couplers including phase relations," Appl. Opt. **33**, 3905–3911 (1994).
44. K. Giewont, K. Nummy, F. A. Anderson, J. Ayala, T. Barwicz, Y. Bian, K. K. Dezfulian, D. M. Gill, T. Houghton, S. Hu, B. Peng, M. Rakowski, S. Rauch, J. C. Rosenberg, A. Sahin, I. Stobert, and A. Stricker, "300-mm monolithic silicon photonics foundry technology," IEEE J. Sel. Top. Quantum Electron. **25**, 8200611 (2019).
45. A. Rahim, T. Spuesens, R. Baets, and W. Bogaerts, "Open-access silicon photonics: current status and emerging initiatives," Proc. IEEE **106**, 2313–2330 (2018).
46. T. W. Weng, Z. Zhang, Z. Su, Y. Marzouk, A. Melloni, and L. Daniel, "Uncertainty quantification of silicon photonic devices with correlated and non-Gaussian random parameters," Opt. Express **23**, 4242–4254 (2015).
47. S. Dwivedi, H. D'heer, and W. Bogaerts, "Maximizing fabrication and thermal tolerances of all-silicon FIR wavelength filters," IEEE Photon. Technol. Lett. **27**, 871–874 (2015).
48. X. Zhou, L. Zhang, A. M. Armani, J. Liu, X. Duan, D. Zhang, H. Zhang, and W. Pang, "An integrated photonic gas sensor enhanced by optimized Fano effects in coupled microring resonators with an athermal waveguide," J. Lightwave Technol. **33**, 4521–4530 (2015).
49. K. B. Gylfason, C. F. Carlborg, A. Kaźmierczak, F. Dortu, H. Sohlström, L. Vivien, C. A. Barrios, W. van der Wijngaart, and G. Stemme, "On-chip temperature compensation in an integrated slot-waveguide ring resonator refractive index sensor array," Opt. Express **18**, 3226–3237 (2010).
50. B. Guha, B. B. Kyotoku, and M. Lipson, "CMOS-compatible athermal silicon microring resonators," Opt. Express **18**, 3487–3493 (2010).
51. D. Xu, M. Vachon, A. Densmore, R. Ma, S. Janz, A. Delâge, J. Lapointe, P. Cheben, J. Schmid, E. Post, S. Messaoudène, and J. Fédéli, "Real-time cancellation of temperature induced resonance shifts in SOI wire waveguide ring resonator label-free biosensor arrays," Opt. Express **18**, 22867–22879 (2010).
52. E. Kleijn, E. Van Vliet, D. Pustakhod, M. Smit, and X. Leijtens, "Amplitude and phase error correction algorithm for 3×3 MMI based Mach–Zehnder interferometers," J. Lightwave Technol. **33**, 2233–2239 (2015).
53. W. Bogaerts and L. Chrostowski, "Silicon photonics circuit design: methods, tools and challenges," Laser Photon. Rev. **12**, 1700237 (2018).
54. G. Di Domenico, S. Schilt, and P. Thomann, "Simple approach to the relation between laser frequency noise and laser line shape," Appl. Opt. **49**, 4801–4807 (2010).
55. D. M. Kuchta, J. Gamelin, J. D. Walker, J. Lin, K. Y. Lau, J. S. Smith, M. Hong, and J. P. Mannaerts, "Relative intensity noise of vertical cavity surface emitting lasers," Appl. Phys. Lett. **62**, 1194–1196 (1993).
56. W. Schottky, "Über spontane Stromschwankungen in verschiedenen Elektrizitätsleitern," Ann. Phys. **362**, 541–567 (1918).
57. V. Mackowiak, J. Peupelmann, Y. Ma, and A. Gorges, and Thorlabs, Inc., "NEP-Noise equivalent power," 2015, https://www.thorlabs.com/images/TabImages/Noise_Equivalent_Power_White_Paper.pdf.

58. A. Sripad and D. Snyder, "A necessary and sufficient condition for quantization errors to be uniform and white," IEEE Trans. Acoust. **25**, 442–448 (1977).
59. N. El-Sheimy, H. Hou, and X. Niu, "Analysis and modeling of inertial sensors using Allan variance," IEEE Trans. Instrum. Meas. **57**, 140–149 (2007).
60. J. Komma, C. Schwarz, G. Hofmann, D. Heinert, and R. Nawrodt, "Thermo-optic coefficient of silicon at 1550 nm and cryogenic temperatures," Appl. Phys. Lett. **101**, 041905 (2012).
61. A. Arbabi and L. L. Goddard, "Measurements of the refractive indices and thermo-optic coefficients of Si_3N_4 and SiO_x using microring resonances," Opt. Lett. **38**, 3878–3881 (2013).
62. A. Densmore, D. X. Xu, S. Janz, P. Waldron, T. Mischki, G. Lopinski, A. Delâge, J. Lapointe, P. Cheben, B. Lamontagne, and J. H. Schmid, "Spiral-path high-sensitivity silicon photonic wire molecular sensor with temperature-independent response," Opt. Lett. **33**, 596–598 (2008).
63. J. Teng, P. Dumon, W. Bogaerts, H. Zhang, X. Jian, X. Han, M. Zhao, G. Morthier, and R. Baets, "Athermal silicon-on-insulator ring resonators by overlaying a polymer cladding on narrowed waveguides," Opt. Express **17**, 14627–14633 (2009).
64. X. Tu, J. Song, T. Liow, M. Park, J. Yiying, J. Kee, M. Yu, and G. Lo, "Thermal independent silicon-nitride slot waveguide biosensor with high sensitivity," Opt. Express **20**, 2640–2648 (2012).
65. H. W. Lim and N. A. Soter, *Clinical Photomedicine* (Dekker, 1993).
66. J. Milvich, "Design of waveguide-based photonic sensor systems | MATLAB," figshare (2020), https://doi.org/10.6084/m9.figshare.13138457.
67. J. T. Kirk, G. E. Fridley, J. W. Chamberlain, E. D. Christensen, M. Hochberg, and D. M. Ratner, "Multiplexed inkjet functionalization of silicon photonic biosensors," Lab Chip **11**, 1372–1377 (2011).
68. J. T. Kirk, N. D. Brault, T. Baehr-Jones, M. Hochberg, S. Jiang, and D. M. Ratner, "Zwitterionic polymer-modified silicon microring resonators for label-free biosensing in undiluted humanplasma," Biosens. Bioelectron. **42**, 100–105 (2013).
69. J. Shang, F. Cheng, M. Dubey, J. M. Kaplan, M. Rawal, X. Jiang, D. S. Newburg, P. A. Sullivan, R. B. Andrade, and D. M. Ratner, "An organophosphonate strategy for functionalizing silicon photonic biosensors," Langmuir **28**, 3338–3344 (2012).
70. N. B. Arnfinnsdottir, C. A. Chapman, R. C. Bailey, A. Aksnes, and B. T. Stokke, "Impact of silanization parameters and antibody immobilization strategy on binding capacity of photonic ring resonators," Sensors **20**, 3163 (2020).
71. R. D. Rohde, H. D. Agnew, W. S. Yeo, R. C. Bailey, and J. R. Heath, "A non-oxidative approach toward chemically and electrochemically functionalizing Si(111)," J. Am. Chem. Soc. **128**, 9518–9525 (2006).
72. P. Cheben, R. Halir, J. H. Schmid, H. A. Atwater, and D. R. Smith, "Subwavelength integrated photonics," Nature **560**, 565–572 (2018).
73. R. Halir, P. J. Bock, P. Cheben, A. Ortega-Moñux, C. Alonso-Ramos, J. H. Schmid, J. Lapointe, D.-X. Xu, J. G. Wangüemert-Pérez, Í. Molina-Fernández, and S. Janz, "Waveguide sub-wavelength structures: a review of principles and applications," Laser Photon. Rev. **9**, 25–49 (2015).
74. T. Komljenovic, D. Huang, P. Pintus, M. A. Tran, M. L. Davenport, and J. E. Bowers, "Photonic integrated circuits using heterogeneous integration on silicon," Proc. IEEE **106**, 2246–2257 (2018).
75. O. Marshall, M. Hsu, Z. Wang, B. Kunert, C. Koos, and D. Van Thourhout, "Heterogeneous integration on silicon photonics," Proc. IEEE **106**, 2258–2269 (2018).

76. S. Tanaka, S. H. Jeong, S. Sekiguchi, T. Kurahashi, Y. Tanaka, and K. Morito, "High-output-power, single-wavelength silicon hybrid laser using precise flip-chip bonding technology," Opt. Express **20**, 28057–28069 (2012).
77. M. J. Heck, J. F. Bauters, M. L. Davenport, J. K. Doylend, S. Jain, G. Kurczveil, S. Srinivasan, Y. Tang, and J. E. Bowers, "Hybrid silicon photonic integrated circuit technology," IEEE J. Sel. Top. Quantum Electron. **19**, 6100117 (2012).
78. C. Xiang, W. Jin, J. Guo, J. D. Peters, M. J. Kennedy, J. Selvidge, P. A. Mortion, and J. E. Bowers, "Narrow-linewidth III-V/Si/Si_3N_4 laser using multilayer heterogeneous integration," Optica **7**, 20–21 (2020).
79. D. Liang and J. E. Bowers, "Recent progress in lasers on silicon," Nat. Photonics **4**, 511–517 (2010).
80. G. Roelkens, L. Liu, D. Liang, R. Jones, A. Fang, B. Koch, and J. E. Bowers, "III-V/silicon photonics for on-chip and intra-chip optical interconnects," Laser Photon. Rev. **4**, 751–779 (2010).
81. C. O. de Beeck, B. Haq, L. Elsinger, A. Gocalinska, E. Pelucchi, B. Corbett, G. Roelkens, and B. Kuyken, "Heterogeneous III–V on silicon nitride amplifiers and lasers via microtransfer printing," Optica **7**, 386–393 (2020).
82. H. Lu, J. S. Lee, Y. Zhao, C. Scarcella, P. Cardile, A. Daly, M. Ortsiefer, L. Carroll, and P. O'Brien, "Flip-chip integration of tilted VCSELs onto a silicon photonic integrated circuit," Opt. Express **24**, 16258–16266 (2016).
83. P. I. Dietrich, M. Blaicher, I. Reuter, M. Billah, T. Hoose, A. Hofmann, C. Caer, R. Dangel, B. Offrein, U. Troppenz, M. Moehrle, W. Freude, and C. Koos, "In situ 3D nanoprinting of free-form coupling elements for hybrid photonic integration," Nat. Photonics **12**, 241–247 (2018).
84. M. R. Billah, M. Blaicher, T. Hoose, P.-I. Dietrich, P. Marin-Palomo, N. Lindenmann, A. Nesic, A. Hofmann, U. Troppenz, M. Moehrle, S. Randel, W. Freude, and C. Koos, "Hybrid integration of silicon photonics circuits and InP lasers by photonic wire bonding," Optica **5**, 876–883 (2018).
85. M. Blaicher, M. Billah, J. N. Kemal, T. Hoose, P. Marin-Palomo, A. Hofmann, Y. Kutuvantavida, C. Kieninger, P.-I. Dietrich, M. Lauermann, S. Wolf, U. Troppenz, M. Moehrle, F. Merget, S. Skacel, J. Witzens, S. Randel, W. Freude, and C. Koos, "Hybrid multi-chip assembly of optical communication engines by in situ 3D nano-lithography," Light Sci. Appl. **9**, 71 (2020).
86. L. Vivien, A. Polzer, D. Marris-Morini, J. Osmond, J. M. Hartmann, P. Crozat, E. Cassan, C. Kopp, H. Zimmermann, and J. M. Fédéli, "Zero-bias 40 Gbit/s germanium waveguide photodetector on silicon," Opt. Express **20**, 1096–1101 (2012).
87. J. Goyvaerts, S. Kumari, S. Uvin, J. Zhang, R. Baets, A. Gocalinska, E. Pelucchi, B. Corbett, and G. Roelkens, "Transfer-print integration of GaAs p-i-n photodiodes onto silicon nitride waveguides for near-infrared applications," Opt. Express **28**, 21275–21285 (2020).
88. K. K. Liu, R. G. Wu, Y. J. Chuang, H. S. Khoo, S. H. Huang, and F. G. Tseng, "Microfluidic systems for biosensing," Sensors **10**, 6623–6661 (2010).
89. Z. Wang, H. Yan, S. Chakravarty, H. Subbaraman, X. Xu, D. Fan, A. X. Wang, and R. T. Chen, "Microfluidic channels with ultralow-loss waveguide crossings for various chip-integrated photonic sensors," Opt. Lett. **40**, 1563–1566 (2015).
90. X. Fan and I. M. White, "Optofluidic microsystems for chemical and biological analysis," Nat. Photonics **5**, 591–597 (2011).
91. C. Adamopoulos, A. Gharia, A. Niknejad, V. Stojanović, and M. Anwar, "Microfluidic packaging integration with electronic-photonic biosensors using 3D printed transfer molding," Biosensors **10**, 177 (2020).
92. L. Laplatine, E. Luan, K. Cheung, D. M. Ratner, Y. Dattner, and L. Chrostowski, "System-level integration of active silicon photonic biosensors using fan-out

wafer-level-packaging for low cost and multiplexed point-of-care diagnostic testing," Sens. Actuators B **273**, 1610–1617 (2018).
93. A. R. Wheeler, "Putting electrowetting to work," Science **322**, 539–540 (2008).
94. S. F. Wondimu, S. von der Ecken, R. Ahrens, W. Freude, A. E. Guber, and C. Koos, "Integration of digital microfluidics with whispering-gallery mode sensors for label-free detection of biomolecules," Lab Chip **17**, 1740–1748 (2017).
95. M. W. Royal, N. M. Jokerst, and R. B. Fair, "Droplet-based sensing: optical microresonator sensors embedded in digital electrowetting microfluidics systems," IEEE Sens. J. **13**, 4733–4742 (2013).
96. C. L. Arce, D. Witters, R. Puers, J. Lammertyn, and P. Bienstman, "Silicon photonic sensors incorporated in a digital microfluidic system," Anal. Bioanal. Chem. **404**, 2887–2894 (2012).
97. L. Luan, M. W. Royal, R. Evans, R. B. Fair, and N. M. Jokerst, "Chip scale optical microresonator sensors integrated with embedded thin film photodetectors on electrowetting digital microfluidics platforms," IEEE Sens. J. **12**, 1794–1800 (2011).
98. J. Heebner, R. Grover, T. Ibrahim, and T. A. Ibrahim, *Optical Microresonators: Theory, Fabrication, and Applications* (Springer, 2008), Vol. **138**.
99. D. S. Elliott, R. Roy, and S. J. Smith, "Extracavity laser band-shape and bandwidth modification," Phys. Rev. A **26**, 12–18 (1982).
100. Keysight application note, "Everything you need to know about complex optical modulation," 2019, http://literature.cdn.keysight.com/litweb/pdf/5992-2888EN.pdf.

Johannes Milvich received his B.Sc. and M.Sc. degrees in Electrical Engineering in 2011 and 2014 from University of Stuttgart. Between 2014 and 2017 he pursued his Ph.D. in Electrical Engineering in a collaboration between the Corporate Research department of Robert Bosch GmbH and the Institute of Photonics and Quantum Electronics (IPQ) at Karlsruhe Institute of Technology (KIT). Since 2017, he has been with the Automotive Electronics division of Robert Bosch GmbH. His research interests include integrated photonics and semiconductor image sensors.

Daria Kohler received her Dipl.-Phys. (M.Sc.) degree in physics from the Karlsruhe Institute of Technology (KIT), Germany, in 2013. Between 2014 and 2020, she worked as a Ph.D. candidate at the Institute of Photonics and Quantum Electronics (IPQ). Since 2020, she has been employed as a research associate and technical project manager at Carl Zeiss Semiconductor Manufacturing Technology (SMT) GmbH, Germany. Her research interests are integrated photonics and biosensors as well as extreme-ultraviolet optics and lithography.

Wolfgang Freude received his Dipl. Ing. (M.S.E.E.) and the Dr. Ing. (Ph.D.E.E.) degrees in Electrical Engineering in 1969 and 1975 from the University of Karlsruhe. He is Professor at the Institute of Photonics and Quantum Electronics and a Distinguished Senior Fellow, both at Karlsruhe Institute of Technology (KIT). His research activities are in the area of optical and wireless high-data rate transmission, and in the field of high-density integrated-optics with a focus on silicon photonics. He has authored and co-authored more than 320 publications as well as a book and seven book chapters. Wolfgang Freude is an Honorary Doctor of the Kharkov National University of Radioelectronics, Ukraine. He serves as a program chair for the OSA Advanced Photonics Congress committee "Photonic Networks and Devices" and as an editorial board member for the Springer Nature journal *Light: Science & Applications*.

Christian Koos has been a full professor at Karlsruhe Institute of Technology (KIT), Institute of Photonics and Quantum Electronics (IPQ) since 2010. He received his Dipl.-Ing. (M.Sc.) and Dr.-Ing. (Ph.D.) degrees in electrical engineering from the University of Karlsruhe in 2002 and 2007, respectively. From 2007 to 2008, he worked as a postdoctoral researcher at the Institute of Photonics and Quantum Electronics (IPQ). From 2008 to 2010, he was with the Corporate Research and Technology Department, Carl Zeiss AG, Germany, where he led the technology forecast in the area of nanotechnology and optical metrology. His research activities comprise photonic integration, nonlinear optics, optical communications, and signal processing, as well as optical metrology and sensing.